

**CORROSION PROCESS MONITORING OF REINFORCED
CONCRETE STRUCTURE USING FIBER BRAGG
GRATING (FBG) STRAIN SENSOR**

OMAR ALMUBAIED

**FACULTY OF ENGINEERING
UNIVERSITY OF MALAYA
KUALA LUMPUR**

2017

**CORROSION PROCESS MONITORING OF
REINFORCED CONCRETE STRUCTURE USING
FIBER BRAGG GRATING (FBG) STRAIN SENSOR**

OMAR ALMUBAIED

**DISSERTATION SUBMITTED IN FULFILMENT
OF THE REQUIREMENTS FOR THE DEGREE OF
MASTER OF ENGINEERING SCIENCE**

**FACULTY OF ENGINEERING
UNIVERSITY OF MALAYA
KUALA LUMPUR**

2017

UNIVERSITY OF MALAYA
ORIGINAL LITERARY WORK DECLARATION

Name of Candidate: OMAR ALMUBAIED

Registration/Matric No: KGA150042

Name of Degree: Master of Engineering Science

Title of Project Paper/Research Report/Dissertation/Thesis (“this Work”): Corrosion Process Monitoring of Reinforced Concrete Structure using strain Fiber Bragg Grating (FBG) Sensor.

Field of Study: STRUCTURAL ENGINEERING AND MATERIALS

I do solemnly and sincerely declare that:

- (1) I am the sole author/writer of this Work;
- (2) This Work is original;
- (3) Any use of any work in which copyright exists was done by way of fair dealing and for permitted purposes and any excerpt or extract from, or reference to or reproduction of any copyright work has been disclosed expressly and sufficiently and the title of the Work and its authorship have been acknowledged in this Work;
- (4) I do not have any actual knowledge nor do I ought reasonably to know that the making of this work constitutes an infringement of any copyright work;
- (5) I hereby assign all and every rights in the copyright to this Work to the University of Malaya (“UM”), who henceforth shall be owner of the copyright in this Work and that any reproduction or use in any form or by any means whatsoever is prohibited without the written consent of UM having been first had and obtained;
- (6) I am fully aware that if in the course of making this Work I have infringed any copyright whether intentionally or otherwise, I may be subject to legal action or any other action as may be determined by UM.

Candidate’s Signature

Date:

Subscribed and solemnly declared before,

Witness’s Signature

Date:

Name:

Designation:

CORROSION PROCESS MONITORING OF REINFORCED CONCRETE STRUCTURE USING STRAIN FIBER BRAGG GRATING (FBG) SENSOR

ABSTRACT

Corrosion of steel reinforcement can occur without visible indication unless it creates cracks on concrete surface. In the context of structure safety, detecting cracks in a structure can be considered a late indication of the structural strength status. Additionally, steel reinforcement corrosion affects the behaviour of the structural member against load, where the vertical displacement of structural members such as beams can be changed. Therefore, measuring the deflection can improve the assessment of the structural health, which will increase the safety of the structure and reduce the repair cost if needed. In this study, an instrumentation for Fiber Bragg Grating (FBG) strain sensor was developed to monitor corrosion process and measure vertical displacement. Laboratory investigations were conducted to evaluate the proposed FBG mounting method that protects FBG during concrete casting and hardening to later facilitate effective detection of steel reinforcement corrosion as well as measurement of vertical displacements of reinforced concrete beams under loading. The mounting method was proposed based on the bend sensitivity of the FBG strain sensor, which enables the sensor to evaluate corrosion and vertical displacement without the need to compare with reference point. The laboratory investigations were divided into two phases. Phase 1 examined the capability of the FBG sensor to monitor steel corrosion process in concrete cylindrical specimens, while Phase 2 examined the capability of the FBG sensor to measure vertical displacement of reinforced concrete beam specimens under loading in addition to corrosion process monitoring. The impressed current technique was adopted to accelerate steel corrosion process during testing. In general, the measurement data provides a good correlation between the corrosion level and FBG wavelength shifts. On the other hand, in the measurement of vertical displacement in Phase 2, the mounting method was slightly

modified to serve the purpose. The modified mounting method has demonstrated to be effective in allowing the FBG strain sensor to measure vertical displacement, from which a coefficient can be obtained from the correlation between the vertical displacement and FBG wavelength shifts. Finally, a statistical procedure for FBG sensing was introduced for assessing FBG measurements accuracy and interpretation.

University of Malaya

ABSTRAK

Penghakisan tetulang keluli boleh berlaku tanpa indikasi sehingga ianya menghasilkan retakan pada permukaan konkrit. Dalam konteks keselamatan struktur, pengesanan retakan-retakan di dalam struktur boleh dianggap sebagai petunjuk yang lewat kepada status kekuatan struktur. Penghakisan tetulang mempengaruhi sifat-sifat struktur sokongan terhadap beban, dimana sesaran menegak struktur sokongan seperti rasuk boleh diubah. Oleh itu, pengukuran pesongan boleh meningkatkan penilaian kesihatan struktur, dimana ianya akan meningkatkan keselamatan struktur dan mengurangkan kos membaik pulih, jika diperlukan. Dalam kajian ini, peralatan untuk Sensor Gentian Belauan Bragg (FBG) telah dibangunkan dan dikaji untuk memantau proses penghakisan dan pengukuran sesaran menegak. Kajian makmal telah dijalankan untuk menilai teknik penyelarasan FBG yang telah dicadangkan, dimana teknik FBG ini dapat mengesan proses penghakisan didalam tetulang dan sesaran menegak sementara dilindungi daripada bancuhan dan pengerasan konkrit. Teknik penyelarasan dicadangkan berdasarkan sensitiviti bengkokan pada sensor terikan FBG, dimana ianya membolehkan pengesanan hakisan dan sesaran menegak tanpa titik rujukan. Kajian makmal telah dibahagikan kepada dua seksyen. Seksyen 1 menyiasat kebolehan sensor untuk memantau proses hakisan. Manakala, seksyen 2 untuk memeriksa kebolehan sensor untuk memantau proses hakisan dan mengukur sesaran menegak pada konkrit bertetulang. Teknik arus penerakan telah digunakan untuk memecutkan proses hakisan. Secara am, keputusan data menunjukkan korelasi yang baik diantara tahap hakisan dan anjakan panjang gelombang sensor terikan FBG. Berkaitan dengan sesaran menegak, teknik pemasangan telah diubah suai di Seksyen 2 supaya membolehkan sensor FBG mengukur sesaran menegak konkrit bertetulang. Teknik pemasangan telah menunjukkan kebolehannya untuk mengukur sesaran menegak dan pekali penghubung diantara sesaran dan anjakan panjang

gelombang tekanan sensor FBG telah dihitung. Akhirnya, satu prosedur statistik telah diperkenalkan untuk penilaian ketepatan dan intepretasi pengukuran FBG.

University of Malaya

ACKNOWLEDGEMENTS

I would like to express my deepest gratitude to my supervisors, Dr. Chai Hwa Kian and Dr. Tan Chee Ghuan for their invaluable kindness, patience, advice, and support. They showed themselves to me as a model scientists and teachers that I eagerly wish to follow. This work would never have been completed without their support and assistance. A special thanks and appreciation go to all the academic staff and the lab assistants at Civil Engineering Department, University of Malaya. Also, I would like to acknowledge the grant High Impact Research (HIR) and University Malaya Research Grant (UMRG) provided from UM to financially support the research work.

Finally, I would like to express my deep gratitude and appreciation to my parents, brothers, sister, and all family members for their consistent love, encouragement, support, and sacrifice. Special thanks should go to my brother Anas Almubaied for being supportive while conducting my study Master of Engineering Science (M. Eng. Sc.).

TABLE OF CONTENTS

Abstract	iii
ABSTRAK	v
Acknowledgements	vii
Table of Contents	viii
List of Figures	xi
List of Tables	xv
List of Symbols and Abbreviations.....	xvi
CHAPTER 1: INTRODUCTION	1
1.1. Research Background	1
1.2. Problem Statement	5
1.3. Significance of the Study	6
1.4. Objectives	7
1.5. Scope of Work	7
CHAPTER 2: LITERATURE REVIEW	8
2.1. Introduction.....	8
2.2. Structural Health Monitoring (SHM).....	8
2.3. Corrosion of Steel Reinforcement.....	11
2.4. Accelerated Corrosion.....	13
2.5. Bond Between Steel Reinforcement and Concrete	15
2.6. FBG Sensing	18

2.6.1.	FBG Sensing for Corrosion	20
2.6.2.	FBG Sensing for Displacement Measurement.....	23
2.6.2.1.	Direct Strain Measurement	23
2.6.2.2.	Vertical Displacement Measurement by Curvature Measurement	27
2.6.2.3.	Vertical Displacement Measurement by Inclination Measurement.....	28
2.6.3.	FBG Parameters	30
2.7.	Statistical Analysis Controlling	35
2.7.1.	Control Charts.....	37
CHAPTER 3: MATERIALS AND METHODS		43
3.1.	Introduction.....	43
3.2.	Materials and Specimens	45
3.2.1.	Concrete	45
3.2.2.	Corrosion Acceleration of Steel Reinforcement	48
3.3.	FBG Sensor Mounting Methods	49
3.3.1.	Phase 1 Experiment.....	50
3.3.2.	Phase 2 Experiment.....	53
3.4.	Corrosion and Displacement Experiments Setup.....	59
3.4.1.	Phase 1 Experiment.....	59
3.4.2.	Phase 2 Experiment.....	61
3.5.	FBG Data Collection.....	64
CHAPTER 4: RESULTS AND DISCUSSIONS		66
4.1.	Accelerated Corrosion Test.....	66

4.1.1.	Phase 1 Experiment.....	66
4.1.2.	Phase 2 Experiment.....	72
4.2.	Concrete Mechanical Properties	82
4.3.	Problems Faced in FBG Data Collection.....	83
4.4.	Phase 2 Flexure Test	91
4.5.	Identification of FBG Parameters (Reflected Spectrum Shape).....	95
4.6.	Shewhart Control Chart for Statistical Analysis Controlling Model	97
CHAPTER 5: CONCLUSIONS AND RECOMMENDATIONS.....		104
REFERENCES		107
SUPPLEMENTARY		115
Paper Presented.....		115

LIST OF FIGURES

Figure 2.1: Corrosion process on steel surface.	12
Figure 2.2: Bond force transfer mechanisms (ACI-408R-03, 2003).	15
Figure 2.3: Formation of Splitting cracks (ACI-408R-03, 2003).	16
Figure 2.4: Formation of hoop stresses and resulting splitting cracks (ACI-408R-03, 2003).	16
Figure 2.5: Pull-out failure (ACI-408R-03, 2003).	17
Figure 2.6: Cross and longitudinal sections of FBG (Majumder et al., 2008).	18
Figure 2.7: Working principle of FBG (Majumder et al., 2008).	19
Figure 2.8: Working principle of TFBG (Gouveia et al., 2013).	21
Figure 2.9: The schematic diagram of the cantilever-based FBG sensor: (A) aluminium baseplate, (B) polymer beam (Dong et al., 2001).	24
Figure 2.10: Experiment setup for implementation of polymer FBG-based bend test (Chen et al., 2010).	25
Figure 2.11: Schematic diagram of the eccentric FBG bend at 0° orientation (Chen et al., 2010).	25
Figure 2.12: Bragg peak shift for increasing curvature: (a) at the 0° orientation; (b) at the 180° orientation (Chen et al., 2010).	26
Figure 2.13: Description of FBG locations in RC beam (Yau et al., 2011).	27
Figure 2.14: The relationships between vertical displacement, slope and curvature (Yau et al., 2011).	28
Figure 2.15: FBG tilt sensor (Yau et al., 2013).	29
Figure 2.16: Spectra changes from embedded FBGs in (a) L1 and (b) L4 with various fatigue cycles under a 140 cm drop height and impact at position B (Shin et al., 2014).	32

Figure 2.17: (a), (b), (c) and (d) Evolution of reflected FBG spectrum shape under tensile loading (Trilaksono et al., 2013).	33
Figure 2.18: Spectrum of the FBG character (Trilaksono et al., 2014).	34
Figure 2.19: Spectrum evolution on profiling tensile test (Trilaksono et al., 2014).	35
Figure 2.20: Construction control chart scheme.	41
Figure 2.21: Typical normal and abnormal patterns (El-Midany et al., 2010).	42
Figure 3.1: Flow chart for the Methodology.	44
Figure 3.2: Details of concrete cylinder specimens for Phase 1 experiment.	46
Figure 3.3: Details of concrete beam specimens for Phase 2 experiments.	47
Figure 3.4: Layout of polystyrene foam cover for FBG strain sensor.	51
Figure 3.5: Procedure used for mounting FBG strain sensor on steel reinforcement bar for Phase1. (a) Fiber sensors were placed on the grinded surface of steel reinforcement. (b) The two ends of FBG strain sensor to steel reinforcement were bonded with epoxy resin. (c) Polystyrene foam was placed to cover FBG strain sensor. (d) Epoxy resin was applied to the perimeter of polystyrene foam to seal gap with steel reinforcement.	52
Figure 3.6: Photo of FBG strain sensor mounted on steel bar with polystyrene foam cover.	53
Figure 3.7: Foam cover dimension.	54
Figure 3.8: Procedure used for mounting FBG strain sensor on steel reinforcement bar for Phase 2. Fiber sensors were placed and fixed on the grinded surface of steel reinforcement.	56
Figure 3.9: Procedure used for mounting FBG strain sensor on steel reinforcement bar for Phase 2. Polystyrene foam was placed to cover FBG strain sensor.	56

Figure 3.10: Procedure used for mounting FBG strain sensor on steel reinforcement bar for Phase 2. Epoxy resin was applied to perimeter of polystyrene foam to seal gap with steel reinforcement.	57
Figure 3.11: Procedure used for mounting FBG strain sensor on steel reinforcement bar for Phase 2. Steel reinforcement cage before concrete pouring.	57
Figure 3.12: Photos of the sensors that were mounted over the steel bar (a) before placing the polystyrene foam (b) after sealing the perimeter of polystyrene foam with steel reinforcement.	58
Figure 3.13: Phase 1 experiment: accelerated corrosion setup (a) photo (b) schematic set up.	60
Figure 3.14: Steel container used for accelerated corrosion of beam specimens.	61
Figure 3.15: Phase 2 experiment: accelerated corrosion setup (a) photo (b) schematic set up.	62
Figure 3.16: Phase 2 experiment: flexure test performed in three-point bending for beam specimens.....	64
Figure 3.17: NI-OSI explorer main menu.....	65
Figure 3.18: LabVIEW front panel.....	65
Figure 4.1: Wavelength shift of cylindrical specimens 1 (a) and 2 (b) versus time and percentage of corrosion.....	68
Figure 4.2 : Condition of specimen 1 and 2 reinforcements and their FBG strain sensors after corrosion experiment. (a) Specimen 1 (b) Specimen 2.	71
Figure 4.3: Specimen 2 shows the crack after the corrosion process.	72
Figure 4.4: Beam cross section of corrosion experiment of Phase 2.	74
Figure 4.5: FBG vs corrosion time for BM2 wavelength shifts of FBG sensors (a) actual in total time of corrosion (b) linear regression.	77

Figure 4.6: FBG vs corrosion time for BM3 wavelength shifts of FBG sensors (a) actual in total time of corrosion (b) linear regression.	78
Figure 4.7: FBG vs corrosion time for BM4 wavelength shifts of FBG sensors (a) actual in total time of corrosion (b) linear regression.	79
Figure 4.8: FBG vs corrosion time for BM5 wavelength shifts of FBG sensors (a) actual in total time of corrosion (b) linear regression.	80
Figure 4.9: Theoretical wavelength shift based on the regression equations.....	81
Figure 4.10: Chloride-induced reinforcement corrosion and cracking patterns (Chen & Mahadevan, 2008).	82
Figure 4.11: NI-OSI Explorer spectral graph view of the multiplex cases (a) missing data (b) detection of unwanted peaks.	84
Figure 4.12: Wavelength shift peaks obtained from (a) real- time monitoring display and (b) time history plot.	85
Figure 4.13: Reflected spectrums before and after corrosion experiment obtained from BM5-1 and BM5-2.	86
Figure 4.14: Reflected spectrums before and after corrosion experiment obtained from BM4-1 and BM4-2.	87
Figure 4.15: Reflected spectrums before and after corrosion experiment obtained from BM3-1 and BM3-2.	88
Figure 4.16: Reflected spectrums before and after corrosion experiment obtained from BM2-1 and BM2-2.	89
Figure 4.17: Reflected spectrums before and after corrosion experiment obtained from BM1-1 and BM1-2.	90
Figure 4.18: Load vs Wavelength shift vs LVDT measurements of all beams (a) BM1, (b) BM2, (c) BM3, (e) BM4, and (e) BM 5.....	94
Figure 4.19: Wavelength shift vs time flexure test for BM3-1.....	94

Figure 4.20: Original reflected peak wavelength shift of undamaged case (a)
Wavelength shift due to vertical displacement or corrosion case (b) wavelength
shift of unwanted peaks case example 1 (b) and example 2 (c). 101

Figure 4.21: X-bar control charts of undamaged case (a) Wavelength shift due to
vertical displacement or corrosion case (b) wavelength shift of unwanted peaks
case example 1 (b) and example 2 (c). 103

LIST OF TABLES

Table 3.1: RC beam specimens.....47

Table 4.1: Current values for each specimen..... 66

Table 4.2: FBG wavelength shift data for specimen 2 from 91 to 107 hours of corrosion
time. 69

Table 4.3: Comparison between theoretical and measured corrosion level for beams’
specimens by weight..... 73

Table 4.4: Regression equations for wavelength shift of corrosion level measurements.
..... 81

Table 4.5: Power reflection values before and after corrosion and of all beams..... 96

LIST OF SYMBOLS AND ABBREVIATIONS

FBG	Fiber Bragg Grating
TFBG	Tilted Fiber Bragg Grating
RC	Reinforced Concrete
SHM	Structure Health Monitoring
SHS	Structure Health State
BS EN	British Standards European Norm
ASTM	American Society for Testing and Materials
SPR	Statistical Pattern Recognition
DSF	Damage Sensitive Feature
NI	National Instruments
RSS	Reflected Spectrum Shape
ICCP	Current Cathodic Protection
AR	Auto-Regressive model
AR(ρ)	Auto-Regressive model with ρ autoregressive terms
λ_B	Bragg wavelength
n_{eff}	Effective refractive index
Λ	Grating period
κ_i	Curvature
ε_i	Longitudinal strain
Y	Distance from neutral axis of cross section
ε^b	Bottom strain
ε^t	Top strain
h	Distance between the sensors
M_s	Mass of steel loss consumed
t	Time in second

I_{corr}	Amount of current flowing through the electrochemical corrosion cell
$M\%$	Steel corrosion by percentage of mass loss
M_0	Original weight

University of Malaya

CHAPTER 1: INTRODUCTION

1.1. Research Background

Steel reinforced concrete (RC) is considered as one of the most popular composite methods embraced by modern construction all over the world, owing largely to a number of reasons such as vast availability of raw materials, flexibility in construction and excellent cost-performance. While embedded steel reinforcements help to improve tensile resistance of structural members, concrete provides cover to protect the steel reinforcements from corrosion. Nevertheless, corrosion of steel reinforcements can usually be found in RC members that have been put under service for a long-time, especially in chloride-borne environments (Khatri & Sirivivatnanon, 2004). In addition, corrosion problem can be profound for RC members which have cracked to an extent that moisture and other corrosion-initiating chemicals can easily penetrate into. This initiates durability issues, which if not attended properly could pose serious threats to the integrity of a whole structure.

The effect of steel reinforcement corrosion on a structure is twofold: firstly, it lowers stiffness and result in loss of structural integrity because of the reduced useful steel cross section area; secondly, the formation of expansive corrosion products introduces undesirable stresses that initiate concrete cracking, resulting in further loss of structural stiffness. A corrosion level of 9 % by weight loss of steel reinforcement can lead to a reduction of the steel-concrete bond strength by two-third of the un-corroded bond (Fang et al., 2004), in other words 9 % corroded bar had one third bond strength of non-corroded bar. However, the bond strength could possibly be slightly enhanced at low corrosion level due to the expansive pressure and the increment of frictional strength between the steel reinforcement and surrounding concrete (Fang et al., 2004). The expansive pressure is generated from the excessive increment in the volume of corrosion

products, which is four to six times bigger than the steel volume (Mao et al., 2015). When the mechanical pressure induced by the corrosion of steel reinforcement exceeds the tensile strength of concrete (which is a tenth of its compression strength), cracks will be formed and the durability will be reduced dramatically. In this regard, the durability of an RC structure is governed by the severity of steel reinforcement corrosion (Mao et al., 2015).

Corrosion can occur without visible indication until it creates cracks on concrete surface. In the context of structure safety, formation of significant cracks from surface of concrete in a structure can be considered a late indication of loss of the structural stiffness. Also, repair cost of a concrete structure due to corrosion cracks can be extremely high, with an estimated cost for maintenance and repair of concrete infrastructure due to corrosion around 100 billion US dollars all around the world (Li & Melchers, 2005), while in 2017 the repair cost estimated 1.8 trillion US dollars (Siad et al., 2017). Therefore, it is important to employ a monitoring system for the detection of corrosion. This can improve the safety, reduce the cost of repair and lengthen the structural service life. It is to be mentioned that corrosion to steel reinforcement affects the behaviour of the structural member due to load, where the vertical displacement can be changed. Therefore, measuring the deflection can improve the assessment of the structural health which will increase the safety of the structure and reduce the repair cost if needed.

Some non-destructive tests (NDT) have been developed for in-situ detection of steel reinforcement corrosion in concrete. Methods such as surface potential measurement, linear polarization measurement, electrochemical impedance spectroscopy can detect steel reinforcement corrosion satisfactory in a qualitative manner (Song & Saraswathy, 2007). Nevertheless, majority of these methods provide predictive

indications for corrosion, such as the rate or potential of corrosion and not the current state of corrosion. Therefore, it is advisable that those methods should not use individually, in other words, at least two methods need to be applied to get reliable measurements. In addition, current NDT examination techniques are only sensitive to some of these failure mechanisms and are responsive only when the defects reach a certain size (Shin et al., 2014). It is necessary to have a method that enables continuous monitoring of steel reinforcement corrosion so that warning of structure deterioration can be provided as early as possible to realize strategic maintenance.

Due to the unique features of Fiber Bragg Grating (FBG) sensing technique, it was adopted in this study as a monitoring tool for assessing corrosion of steel reinforcement in concrete. FBG sensors possess numerous advantages for practical applications, such as their immunity to electromagnetic interference and power fluctuation along the optical path, small size and lightweight, corrosion resistance and high durability. Furthermore, the sensors can be multiplexed and instrumented to receive signals from sources located up to a few kilometers away with high precision. Besides strain and temperature, the FBG sensing technique allows measurement of some other key engineering properties including pressure, and force (Lim et al., 2002; Bock et al., 2007; Ma et al., 2012). Therefore, the FBG sensing technique has attracted much attention from the civil engineering community over the past decade for structural health, vibration and seismic response monitoring (Majumder et al., 2008).

Furthermore, FBG strain sensor has the bend sensitivity (Chen et al., 2010) which makes the FBG strain sensor capable of detecting displacement without the need of a reference point. Also, it can be used for real time monitoring by collecting FBG

measurements of the structure before any damage or load occurs and during the service life of the structure.

As mentioned earlier corrosion detection and monitoring are critical exercises that provide evaluation on the health status of structures, for instance bridges. Thus, the main aim of this study is to develop an FBG sensing methodology that provides reliable measurements for the detecting and monitoring steel reinforcement corrosion in concrete members. Besides that, the sensing methodology will also enable vertical displacement measurement of the RC member in the event of loading, so that the effect of steel reinforcement corrosion and other damages on structural behaviour can be assessed (Moses et al., 1994; Saraf & Nowak, 1998). The methodology shall be used to establish a useful alarm system for structural integrity, which evaluates measurement data to indicate steel reinforcement corrosion progress and the associated damage, such as excessive displacement. The system should provide the structure's health status to facilitate appropriate remedial that achieves cost-effectiveness.

1.2. Problem Statement

RC structures start to deteriorate once they are built and used, however, their deterioration differs based on many factors such as environmental exposure conditions as well as load and servicing state. Therefore, maintaining safe and reliable RC structures for daily use is important to the wellbeing of all of us. Knowing the integrity of the RC structure is important and necessary to ensure safety and prevent a catastrophic event from occurring.

Monitoring techniques of corrosion have been considered costly due to the complexity of corrosion process detection and non-uniformity of corrosion process. Therefore, other structural parameters can be used such as vertical displacement to give a better estimation of the Structure Health State (SHS). However, using multiple techniques to get the SHS of structure can increase the cost of Structure Health Monitoring (SHM). Thus, engineers need a method that can monitor the corrosion condition especially and evaluate displacement additionally of a structural member to reduce the total cost of SHM. FBG sensors' applications for SHM to detect corrosion of RC structures have shown its advantages over other methods. Generally, based on the literature, the FBG sensors for corrosion detection can be divided into two main types, detects corrosion of steel reinforcement in wet condition, while the second type is based on detecting the physical changes of the material surrounding the FBG strain Fiber. However, the first type is fragile, costly to manufacture and it needs to be in direct contact with corroded environment. On the other hand, the second type focuses on the strain generated on the concrete due to the cracks, which considered a late indication. In other words, there is still room for improvement in corrosion measurement using FBGs in terms of FBG installation and measurement accuracy. Therefore, this study is aimed at developing and signal processing methodology for FBG sensing method to be utilized for detecting corrosion and measure vertical displacement of RC structures such as bridges.

Furthermore, the method is aimed to be cost effective by using bare FBG strain sensors without applying any encapsulation on the FBG strain fiber, which may alter and possibly reduce the sensitivity of the FBG strain sensor and increase its cost. The method is used at the construction or reconstruction (repair) stage to ensure the earliest detection of corrosion.

1.3. Significance of the Study

Corrosion of steel reinforcement in concrete and its assessment techniques are topics widely studied over the last two to three decades. Besides, evaluating other structural parameters, such as vertical displacement of a corroded concrete member can provide more information on the SHS. Therefore, many SHM techniques have been studied and implemented as attempts to enhance assessment for SHS. This leads to the increment of SHM process cost. It is desired that a relatively cost-effective method be developed to realise corrosion monitoring and deflection evaluation concurrently in a real-time manner.

Although the Fiber Bragg Grating (FBG) sensing has exhibited its efficiency to monitor vertical displacement of structural members, there are limited studies on adopting the technique for detecting and monitoring corrosion steel reinforcement in concrete. Therefore, this study is purposed at developing a methodology of instrumentation, signal processing and interpretation for FBG sensing to detect, monitor and evaluate steel reinforcement corrosion in concrete members as well as provide displacement data in real time for assessing the effect of corrosion on structural behaviour. Also, a statistical analysis controlling model is proposed to improve FBG measurements accuracy and interpretation.

1.4. Objectives

The objectives of the study are as follows:

- To propose and study a new instrumentation method for FBG sensing for monitoring steel reinforcement corrosion in concrete structure without damaging the FBG sensors used.
- To investigate the relationships between FBG sensing data with corrosion level of steel reinforcement in concrete and vertical displacement of RC beams.
- To establish a statistical monitoring scheme for assessing FBG measurements accuracy and interpretation.

1.5. Scope of Work

The study investigates the capability of the proposed instrumentation for FBG sensing to protect the FBG sensor itself, detect corrosion level and monitor vertical displacement. Two main experiments, accelerated corrosion and flexure, were conducted to investigate the sensing method capabilities. The corrosion experiments included cylindrical and beam specimens, where the corrosion levels varied from 0% to 10%. On the other hand, the flexure experiments included RC beams only. Finally, a statistical analysis was performed on FBG measured data to establish an alarm system that can recognize any unnatural patterns of FBG measured data.

CHAPTER 2: LITERATURE REVIEW

2.1. Introduction

The literature review presents an introduction to Structural Health Monitoring (SHM) of structures, corrosion and its effects of steel reinforcements and summarizes the techniques used in corrosion measurement and vertical displacement of structures by using FBG sensors. Section 2.2 reviews the SHM, damage and its importance. Section 2.3 reviews corrosion of steel reinforcement principle. Section 2.4 illustrates the acceleration corrosion technique. Section 2.5 reviews the steel reinforcements bond and the effects of corrosion process. Section 2.6 reviews the technique used to evaluate corrosion and vertical displacement by using FBG sensors. Finally, Section 2.7 reviews the statistical analysis techniques used for FBG's measurements analysis.

2.2. Structural Health Monitoring (SHM)

SHM can be defined as the process of identification of damage, where in the most general terms, damage can be defined as changes introduced into a system that adversely affect its current or future performance. Implicit in this definition is the concept that damage is not meaningful without a comparison between two different states of the system, one of which is assumed to represent the initial state (undamaged state), and damaged state. This theme issue is focused on the study of damage identification in structural and mechanical systems. Therefore, the definition of damage will be limited to changes to the material and/or geometric properties of these systems, including changes to the boundary conditions and system connectivity, which adversely affect the current or future performance of these systems (Farrar & Worden, 2007).

In terms of length-scales, all damages begin at the material level. Although not necessarily a universally accepted terminology, such damage is referred to as a defect or flaw and is present to some degree in all materials. Under appropriate loading scenarios, the defects or flaws grow and coalesce at various rates to cause component and then system-level damage. The term damage does not necessarily imply a total loss of system functionality, but rather that the system is no longer operating in its optimal manner. As the damage grows, it will reach a point where it affects the system operation to a point that is no longer acceptable to the user. This point is referred to as a failure. In terms of time-scales, damage can accumulate incrementally over long periods of time such as that associated with fatigue or corrosion damage accumulation. On relatively shorter time-scales, damage can also result from scheduled discrete events such as aircraft landings and from unscheduled discrete events such as natural phenomena hazards such as earthquakes (Farrar & Worden, 2007).

The damage state of a system can be described as a five-step process along the lines of the process discussed by Rytter (1993) to answer the following questions.

- (i) Existence. Is there damage in the system?
- (ii) Location. Where is the damage in the system?
- (iii) Type. What kind of damage is present?
- (iv) Extent. How severe is the damage?
- (v) Prognosis. How much useful life remains?

The meaning of damage and its effects on the structure are twofold, therefore, SHM is critical to insure safety and reduce repair cost. SHM in more specific meaning is the process of implementing a damage identification strategy for aerospace, civil and mechanical engineering infrastructure (Farrar & Worden, 2007). A wide variety of highly

effective local non-destructive evaluation tools are available for such monitoring. However, the majority of SHM research conducted over the last 30 years has attempted to identify damage in structures on a more global basis. The past 10 years have seen a rapid increase in the amount of research related to SHM as quantified by the significant escalation in papers published on this subject. The increased interest in SHM and its associated potential for significant life-safety and economic benefits has motivated the need for this theme issue (Farrar & Worden, 2007).

The process of implementing a damage identification strategy involves the observation of a structure or mechanical system over time using periodically spaced measurements, the extraction of damage-sensitive features from these measurements and the statistical analysis of these features to determine the current state of system health. For long-term SHM, the output of this process is periodically updated information regarding the ability of the structure to continue to perform its intended function in light of the inevitable aging and damage accumulation resulting from the operational environments. Under an extreme event, such as an earthquake or unanticipated blast loading, SHM is used for rapid condition screening. This screening is intended to provide, in near real-time, reliable information about system performance during such extreme events and the subsequent integrity of the system.

Damage identification is carried out in conjunction with five closely related disciplines that include SHM, Condition Monitoring (CM), Non-Destructive Evaluation (NDE), Statistical Process Control (SPC) and Damage Prognosis (DP). Typically, SHM is associated with online–global damage identification in structural systems such as buildings. CM is similar to SHM, but addresses damage identification in rotating and reciprocating machinery, such as those used in manufacturing and power generation.

NDE is usually carried out off-line in a local manner after the damage has been located. There are exceptions to this rule, as NDE is also used as a monitoring tool for in situ structures such as pressure vessels and rails. NDE is therefore primarily used for damage characterization and as a severity check when there is a prior knowledge of the damage location. SPC is process-based rather than structure-based and uses a variety of sensors to monitor changes in a process, one cause of which can result from structural damage. Once damage has been detected, DP is used to predict the remaining useful life of a system. This study, however, will focus on SHM.

Almost all private and government industries want to detect damage in their infrastructure at the earliest possible time. Such detection requires these industries to perform some form of SHM and is motivated by the potential life-safety and economic impact of this technology. Such downtime can cost these companies on the order of millions of dollars per hour. Clearly, such damage identification has significant life-safety implications.

2.3. Corrosion of Steel Reinforcement

Corrosion of steel in any environment is a process that involves progressive removal of atoms of iron (Fe) from the steel being corroded. The iron is removed by an electrochemical reaction and is dissolved in the surrounding water solution, appearing as ferrous (Fe^{2+}) ions. On steel embedded in concrete, the dissolution takes place in the limited volume of water solution present in the pores of the concrete surrounding the steel. As a result of this dissolution process, the steel loses mass, i.e. its cross-section becomes smaller.

The corrosion of steel in concrete is an electrochemical process in which both chemical reactions and flow of electrical current are involved. The chemical and electrical processes are coupled. In order to evaluate conditions that might lead to steel corrosion in concrete, one needs to be familiar with at least the basic concepts of both the chemical reactions and the electrical processes involved.

The basic concept of the corrosion processes is not overly complex. The processes shall be described in simple terms, emphasizing only those aspects that are important in understanding steel corrosion in concrete (Bentur et al., 1997). The corrosion process actually involved two separate, but coupled, chemical reactions that take place simultaneously at two different sites on the steel surface. As indicated in Figure 2.1, an electric current must flow in a closed loop between the two sites for the reactions to proceed. The overall process is quite similar to what takes place in an ordinary dry cell battery means of which electricity is generated. Such batteries are technically described as ‘galvanic corrosion’ (Bentur et al., 1997).

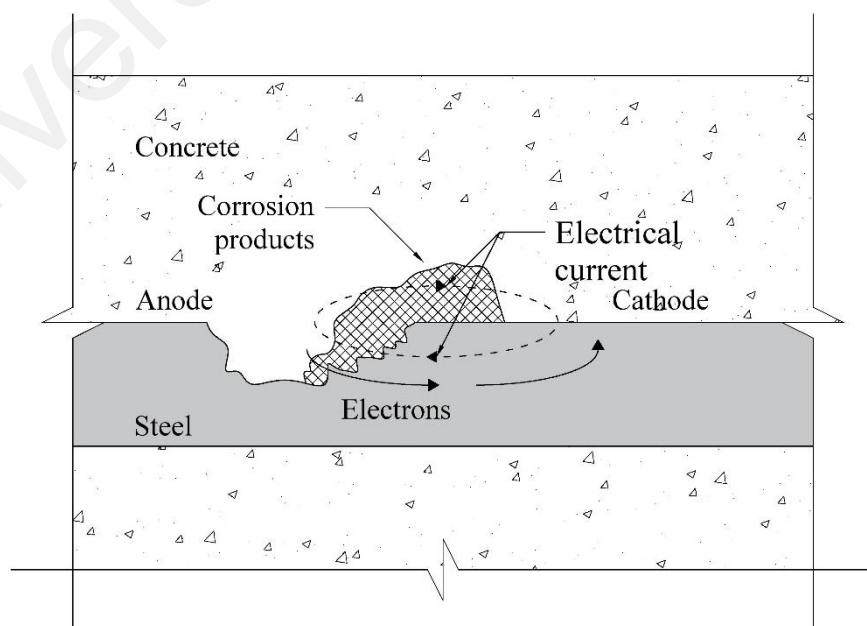


Figure 2.1: Corrosion process on steel surface.

In corrosion, the two electrochemical reactions are known as ‘anodic’ and ‘cathodic’ reactions, respectively, and the areas on which they occur in the steel are called ‘anodic’ and ‘cathodic’ areas or simply anodes and cathodes, as indicated in Figure 2.1.

The two reactions are as follow (Bentur et al., 1997):

Corrosion reactions:

Anodic reaction



metallic atoms at
the steel surface

ions dissolved in solution



dissolved oxygen
molecules

ions dissolved in solution

The flow of electrons from the anodic areas where they are produced by the anodic reaction (2.1) to the cathodic areas where they are used in the cathodic reaction (2.2), and its counter-current ionic flow in the external concrete pore solution constitute the corrosion current. Such flow is extremely important, since its interruption will the corrosion process to come to a halt.

2.4. Accelerated Corrosion

Accelerated corrosion by means of the impressed current technique is widely used in concrete durability tests (Boerstler & Frankel, 2017; Qiao et al., 2017). Utilizing impressed current to better control and accelerate the charge passed from anode to counter-electrode compared to simple exposure, which eventually allow better control of corrosion process and shorten the testing period. The magnitude of reinforcement corrosion has a significant effect on flexural strength, deformational behaviour, ductility, bond strength, and mode of failure of the reinforced-concrete structures (El Maaddawy

& Soudki, 2003). As a result, the degree of corrosion is considered as one of the main parameters to predict the useful service life of corroding reinforced-concrete structures. It is possible, with varying degrees of accuracy, to measure the amount of steel dissolving and forming oxides (rust). This is done directly as a measurement of the electric current generated by the anodic reaction (see equation 2.1) and consumed by the cathodic reaction (see equation 2.2). Then converting the current flow by Faraday's law to metal loss (Chen & Mahadevan, 2008). The impressed current technique in accelerated corrosion studies is used so that tests can be conducted faster than the natural corrosion process.

Corrosion is induced by applying an electrochemical potential between the reinforcing steel (anode) and a cathode. With some modification, the same technique can be used to protect the embedded steel reinforcement from corrosion (cathodic protection). Impressed Current Cathodic Protection (ICCP) of atmospherically exposed steel reinforced concrete structures has been used since the 1970s and it is a proven technique which is able to arrest ongoing corrosion and induce and sustain steel passivity (Koleva et al., 2009). The main principle of cathodic protection is applying an impressed current such as to induce negative steel polarisation British Standards European Norm (BS EN, 2000), in other words to drive the steel potentials more cathodically than -850 mV (SCE: saturated calomel electrode), where corrosion process is thermodynamically impossible to occur (Christodoulou et al., 2010). Under these conditions the steel will be immune to corrosion.

2.5. Bond Between Steel Reinforcement and Concrete

In reinforced concrete, the transfer of forces between deformed steel bars and the adjacent concrete occurs by three primary modes: 1) chemical adhesion between the bar and concrete (Du Béton, 2000), 2) friction forces, transverse forces, and relative slip, and 3) bearing of the ribs or deformations against the surrounding concrete. For deformed bars, adhesion is lost after the initial slip. This slip initiates bearing of the ribs against the surrounding concrete. Frictional forces along the surface of the bar remain small compared to these bearing forces, and bearing plays the biggest role in bond behaviour. To balance the forces on the surface of the deformed bar, which are shown in Figure 2.2, compressive and shear stresses develop in the contacting concrete surfaces. These stresses develop into tensile stresses which in turn can lead to cracking of the concrete (American Concrete Institute (ACI 408R-03, 2003)). The types of crack found in reinforced concrete structures are discussed in this section.

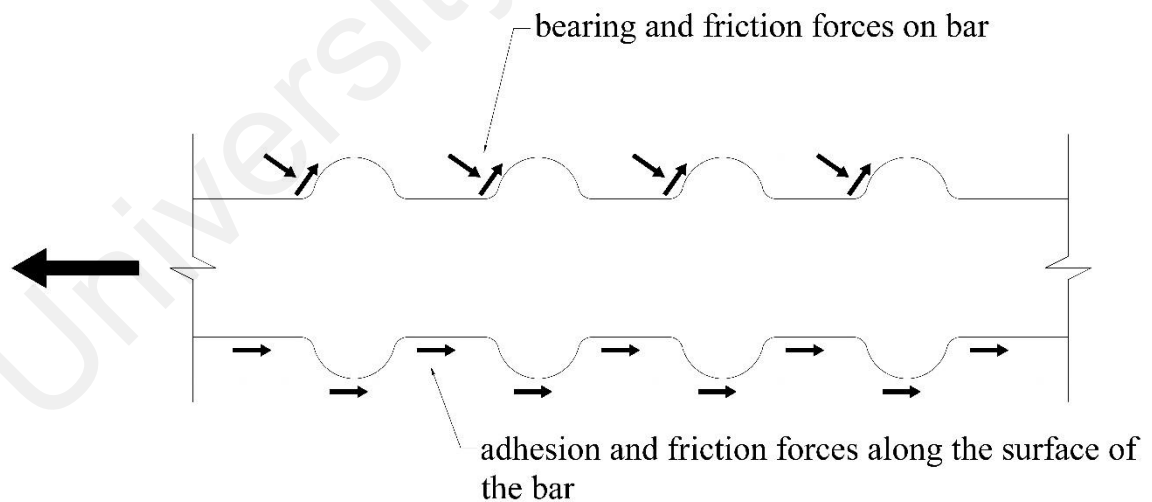


Figure 2.2: Bond force transfer mechanisms (ACI 408R-03, 2003).

Splitting cracks can form as a result of the tension stresses induced by the compression forces at the bearing contact surfaces extending from the ribs. The formation of these cracks is shown in Figure 2.3. These cracks can result in a conical failure surface

for bars in tension that extend outside of the concrete. However, Splitting cracks do not play a significant role in bond anchorage or steel reinforcement development (ACI 408R-03, 2003).

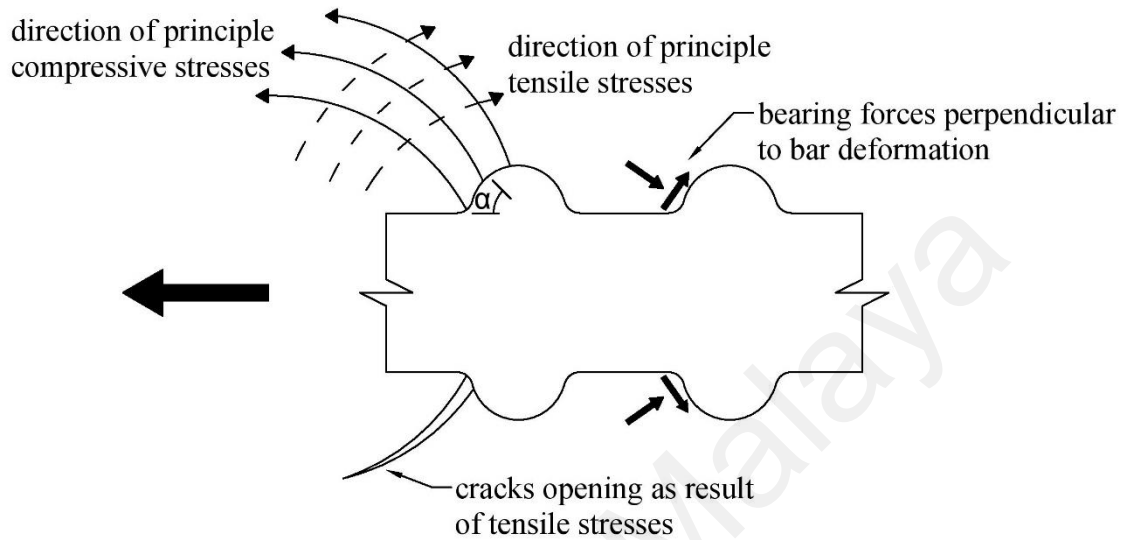


Figure 2.3: Formation of Splitting cracks (ACI 408R-03, 2003).

Transverse cracks, formed when the minimum concrete cover or bar spacing is small. The transverse cracks form as a result of hoop tensile stresses in the surrounding concrete induced by the bearing action of the ribs. With small cover, these cracks can reach the outside surface of the concrete and form splitting cracks as shown in Figure 2.4.

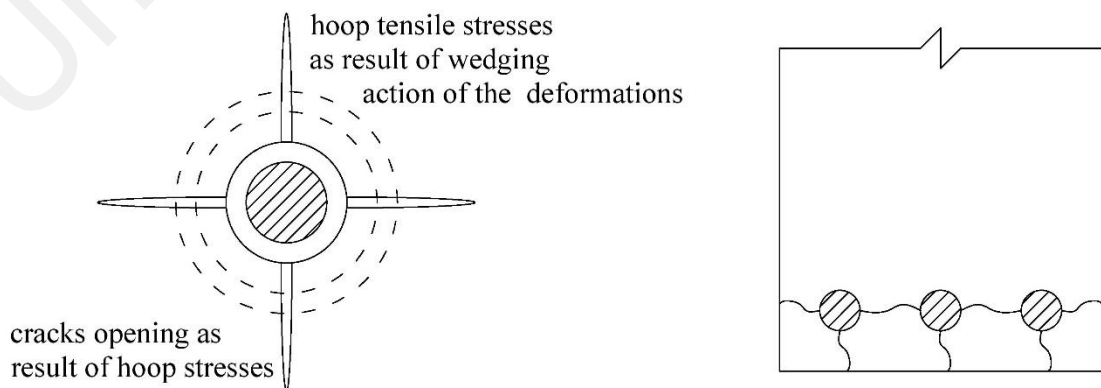


Figure 2.4: Formation of hoop stresses and resulting splitting cracks (ACI 408R-03, 2003).

When concrete cover and the bar spacing is sufficiently large or enough transverse steel reinforcement is provided to prevent splitting failure, the bond failure may be a pull-out type. This failure results in the shearing along the top surfaces of the reinforcing bar's ribs as shown in Figure 2.5. Most bond failures result as a combination of both concrete splitting and pull out type failure modes (ACI 408R-03, 2003). It is also possible that if anchorage of the bar into the concrete is adequate and sufficient confinement is provided to delay crack propagation, the steel bar may yield or strain harden prior to bond failure. Thus, bond failure only occurs when stresses in the steel do not exceed its tensile strength.

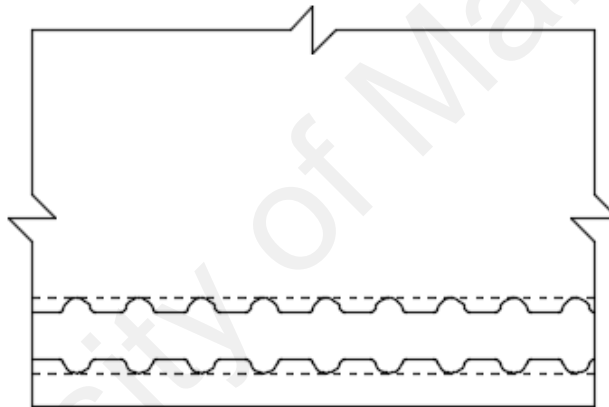


Figure 2.5: Pull-out failure (ACI 408R-03, 2003).

Based on the above discussion, it is obvious that bond behaviour is largely controlled by the following factors: mechanical properties of the surrounding concrete, concrete cover and bar spacing, presence or absence of confinement, surface condition of the bar, and the geometry of the bar (namely deformation shape, rib height, and bar diameter). Corrosion of steel reinforcements can lead to change of surrounding concrete, surface condition of the bars, the diameter of the bars and creates transverse cracks due to the stress generated from the excessive volume corrosion products. All those changes reduce dramatically the friction and bearing resistance of steel reinforcements.

2.6. FBG Sensing

In the last two decades, a considerable number of investigations have been conducted in reviewing the progress of research and development of the optical fiber sensing technology as well as the applications of optical fiber sensors in the monitoring of various kinds of engineering structures (Ye et al., 2014). FBG sensing in particular has shown its efficiency in many areas such as large composite and concrete structures, the electrical power industry, medicine, and chemical sensing (Rao, 1999). Up to now, the FBG sensor has been widely used in monitoring of civil engineering structures (Tan et al., 2016; Choi et al., 2016; Hong et al., 2016; Kouroussis et al., 2016), where Majumder et al. (2008) reviewed various studies and developments in structural monitoring using FBG sensors.

The FBG strain sensor is a type of optical fiber sensor that is prepared by exposing the core of a glass fiber to UV laser using a phase mask technique (Zhou et al., 2003). This exposure creates a fixed index modulation by an increment of refractive index of the core of glass fiber. Figure 2.6 shows the core and the cladding cross section of a glass fiber along with a segment of optical fiber with a periodic variation of refractive index in the core. This periodic modulated fiber segment is called fiber Bragg grating that reflects specific wavelengths of light and allows the others to transmit.

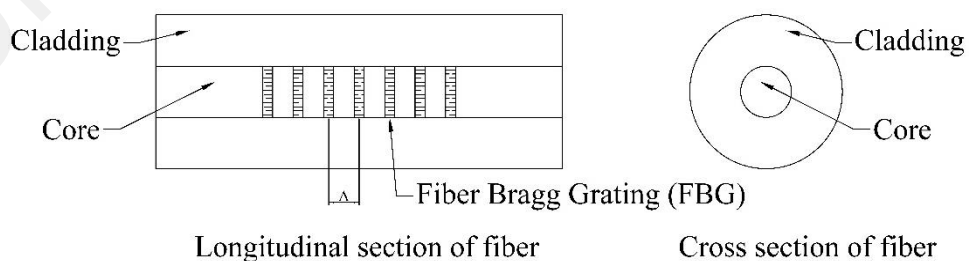


Figure 2.6: Cross and longitudinal sections of FBG (Majumder et al., 2008).

A small quantity of light is reflected from FBG at each variation of periodic refraction. These reflected light signals merge to a single giant reflection at a distinct wavelength as illustrate in Figure 2.7. This situation is called Bragg condition, and Bragg wavelength is the wavelength where Bragg condition takes place. This Bragg wavelength (λ_B) can be changed by changing either effective refractive index (n_{eff}) or grating period (Λ) or both, this change can be expressed as:

$$\lambda_B = 2 n_{\text{eff}} \Lambda \quad (2.3)$$

The parametric variations in the grating region due to strain or temperature will lead to a shift in the Bragg wavelength. This wavelength shift can be used to measure strain ($\Delta\lambda = 1.2 \text{ pm}/\mu\epsilon$) and/or temperature (Pereira et al., 2016). Λ will be changed if the FBG is subjected to a deformation. Such deformation may be caused by mechanical strains from axial stress bending stress or thermal strains from change of the ambient temperature of the fiber (Shin et al., 2014).

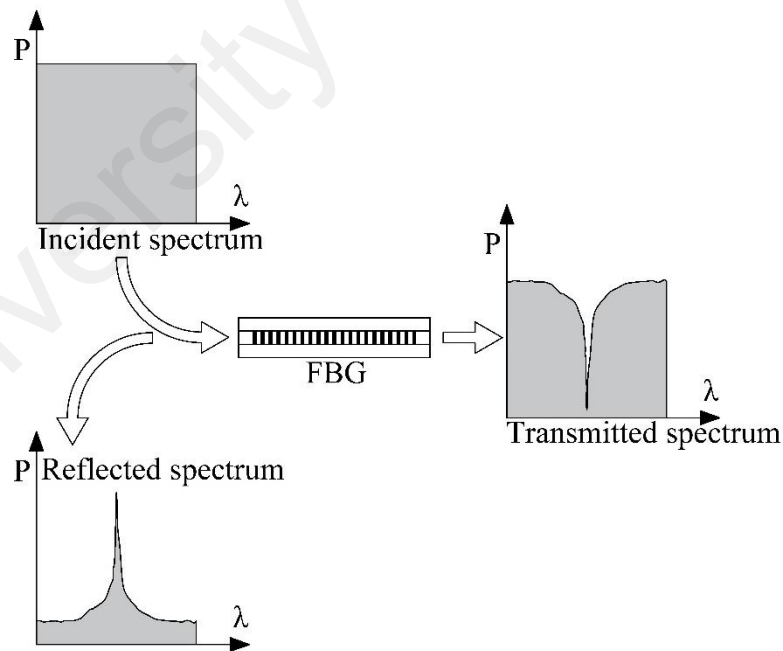


Figure 2.7: Working principle of FBG (Majumder et al., 2008).

2.6.1. FBG Sensing for Corrosion

This sub-section reviews the type and techniques used to monitor corrosion by using FBG sensors. Tilted FBG (TFBG) or laser ablated clad grating fiber sensors can be used for the monitoring of corrosion of steel reinforcement in wet condition based on the surrounding Refractive Index (SRI) variation of the chemical or electrochemical transformation that take place in corrosion process (Hassan et al., 2012; Islam et al., 2015; Islam et al., 2016) (see Figure 2.8). The TFBGs have attracted extensive attention to numerous industrial sensing applications, such as temperature-independent vibration measurement (Guo et al., 2008), strain measurement (Chen et al., 2007), concentration sensor (Melo et al., 2014), magnetic field sensing (Yang et al., 2014), and twist/torsion measurement (Shen et al., 2014). The tilted periodic modulation in the fiber core triggers the couplings between core and cladding modes (Erdogan & Sipe, 1996). The couplings contribute to a generation of multiple dips in the transmission spectrum, which can be easily achieved by tilting the grating plane or phase mask during the grating inscription process. The excited cladding modes have stronger interaction with the ambient medium of the fiber and cladding removal is not required to achieve that. This makes it an attractive sensor for refractive index. The measured transmission spectrum of the TFBG with the coverage of cladding modes and fundamental mode can be recorded. However, TFBGS need to have to record the retreated wave and the transmission spectrum, which the TFBG needs to be connected on both ends. On the other hand, the FBG strain sensors need only to be connected to an interrogator from one end.

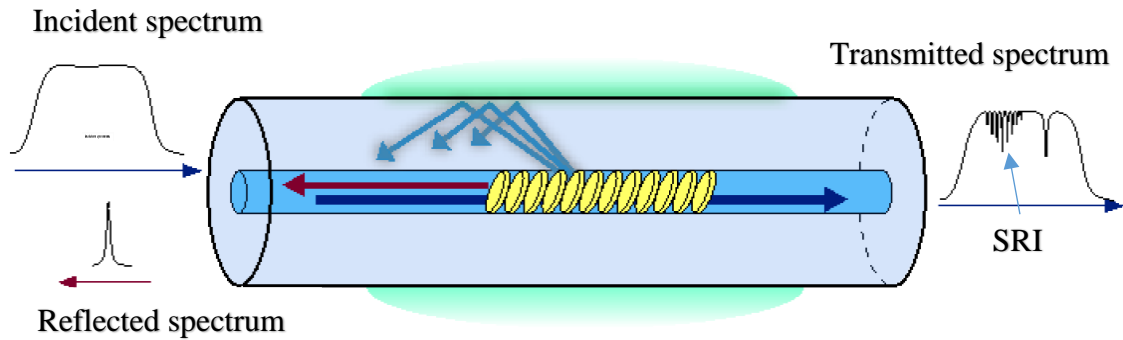


Figure 2.8: Working principle of TFBG (Gouveia et al., 2013).

FBG strain sensors can also be used to monitor corrosion. Mao et al. (2015) had used tight- buffered FBG and covered with epoxy resin to protect the fiber and to reduce the effect of the fiber on the concrete specimen integrity. Also, Mao used bare FBG sensor's properties which has the flexibility and precision to detect corrosion-induced crack where the fiber was placed as a hoop around impeded steel reinforcement. Chen and Dong (2012) have used the FBG strain sensor to detect the concrete changes around the steel reinforcement, his technique is similar to Mao et al. (2015) where a loop was created around the steel reinforcement with an offset to detect the concrete's changes. His study found a relationship between the axial strain due to the rebar corrosion and the wavelength shift of FBG sensor. However, Hu et al. (2011) had stripped at the grading part of the fiber with two layers, the first layer was Silver film followed by Fe-C sensing film as the second layer. The purpose of choosing Fe-C sensing film is its ability to change longitudinally due to rusting reaction. The film changes can cause strain on FBG, which will lead to wavelength shift. The Fe-C film's composition and parameters are $\text{FeSO}_4 \cdot 7\text{H}_2\text{O}$ (40 g/L), Citric acid (1.2 g/L), L-ascorbic acid (3.0 g/L), pH (2.5) and I (30 mA/cm²). Gao et al. (2011) on the other hand, used a different approach for mounting and sensing technique to sense corrosion level. A standard FBG strain fiber fixed between twin steel rebars perpendicularly to rebars axis. The principle is to use the expansion of the twin rebars' diameters due to the corrosion product formation and that will cause the

twin bars to push each other. The FBG was fixed at each rebar therefore it can detect the longitudinal strain caused by the movement of rebars' centres from each other.

The FBG sensors for corrosion detection can be divided into two main types. The first type detects corrosion of steel reinforcement in wet condition based on the surrounding refractive index (SRI), while the second type is based on detecting the physical changes of the material surrounding the FBG strain Fiber. Those changes are generated from the stresses imposed from the expansion of the corrosion products. Based on literature, the first type is applied in protected environments due to its fragility and this type needs to be in direct contact with corroded environment due to its sensitivity refractive index. To increase the refractive sensitivity, studies have etched the cladding of FBG, which increases its fragility, or change the Bragg Grating formation (TFBG) (Hassan et al., 2012). However, the second type mainly focuses on monitoring the effect of the corrosion on concrete or other materials and detecting the structural changes on the concrete. Previous studies focused on the strain generated on the concrete due to the cracks, where the common application of the fiber is being a hoop around the steel reinforcement in the concrete material. It is to be noted, the formation of cracks as observed from the surface of concrete is considered as a late indication of SHS. Nevertheless, others have used a coating material on the FBG that can react with the corrosion intensity. The coating material expands due to corrosion and causes strain on the FBG. Finally, some studies use the expanding volume of corrosion by using FBG and detect the strain created by direct tensile forces on FBG (Gao et al., 2011). However, To the authors' best knowledge, there is limited literature reports on the direct application of bare FBG sensors to steel bar and on using the bend sensitivity of FBG for corrosion monitoring. Using bare FBG strain sensors have better bend sensitivity that encapsulated

ones because applying any encapsulation on the FBG strain fiber may alter and possibly reduce the sensitivity of the FBG strain sensor (Zhou et al., 2003).

2.6.2. FBG Sensing for Displacement Measurement

This sub-section reviews the techniques and methods used to monitor displacement by using FBG strain sensors. The techniques are direct strain measurement, vertical displacement by curvature measurement and vertical displacement by inclination measurement.

2.6.2.1. Direct Strain Measurement

FBG strain sensors can be used for bending sensitivity to evaluate the vertical displacements. However, some studies used the basic bend sensitivity of the FBG strain sensor and others modify the sensors to have higher bend sensitivity. Dong et al. (2001) has used FBG strain sensor where Dong bonded the FBG crosswise on the joint section of a specially constructed cantilever. The cantilever is composed by sticking the fixed end of a polymer beam on an aluminum base plate as shown in Figure 2.9. Part of the FBG (FBG1) is attached on the surface of the polymer beam, while the other part (FBG2) is attached to the surface of the aluminum base plate. Since the base plate is fixed, vertical displacement of the polymer beam's free end changes the axial strain of the FBG1. The Bragg wavelength of FBG1 then changes according to the vertical displacement. One thus can get information of the displacement by monitoring the wavelength shift of FBG1. Furthermore, because of the different rigidities and thermal expansion coefficient for the polymer beam and the aluminum base plate, FBG1 and FBG2 respond directly to the displacement and temperature variation. As a result, the Bragg wavelength of the original FBG is split into two Bragg wavelengths, which correspond to the two parts of the

displacement and temperature measurement. By measuring the shifts of these two new Bragg wavelength, displacement and temperature can be determined simultaneously.

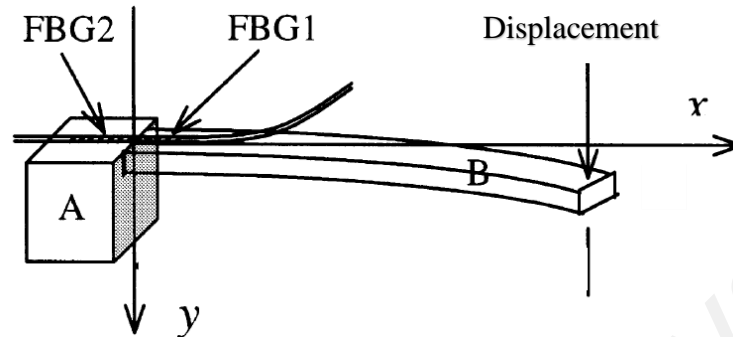


Figure 2.9: The schematic diagram of the cantilever-based FBG sensor: (A) aluminium baseplate, (B) polymer beam (Dong et al., 2001).

Several bend sensors based on FBGs have been demonstrated which employed multiple-core fiber with an asymmetric axially offset FBG (Patrick, 2000; Flockhart et al., 2003; Martinez et al., 2005; Yong et al., 2006). Those types of sensors are modified to get high bend sensitivity, but increase the system cost. In contrast, Chen et al. (2010) used a wavelength-encoded sensor based on a Bragg grating written in eccentric-cored polymer optical fiber (ecPOF) to achieve higher bend sensitivity without increasing the system cost. Its core is offset from the fiber neutral axis, inducing the required asymmetry in the device to enable vector bend sensing with high sensitivity and wide curvature range. The experimental arrangements for bend test are shown in Figure 2.10. The polymer fiber with a gauge length of 90 mm ($2L$) was hung between two translation stages with the FBG at its center. Both ends of the POF were clamped onto the stages. The bend sensing experiment was conducted by driving the right-hand stage's micrometer screw along the '-z' direction, which resulted in a bent that lay in the vertical plane. As shown in Figure 2.11, the bending curvature C is given by $C = 1/R = 2h/(h^2 + L^2)$, where h is the displacement from the straight position and $2L$ is the length of bend section. To ensure the bend was in the vertical plane, two parallel plastic plates were set up either side of the

fiber to constrain its movement. It is obvious that if the core is located above or below the neutral axis, the core will be in compression or extension during bending. The spectral response of the polymer FBG to curvature variations was monitored for different fiber orientations. As shown in Figure 2.12, at 0° orientation, the Bragg peak blue-shifted to shorter wavelengths; in contrast, the peak moved to the longer side for the 180° orientation, where the polymer FBG experienced compression and extension, respectively.

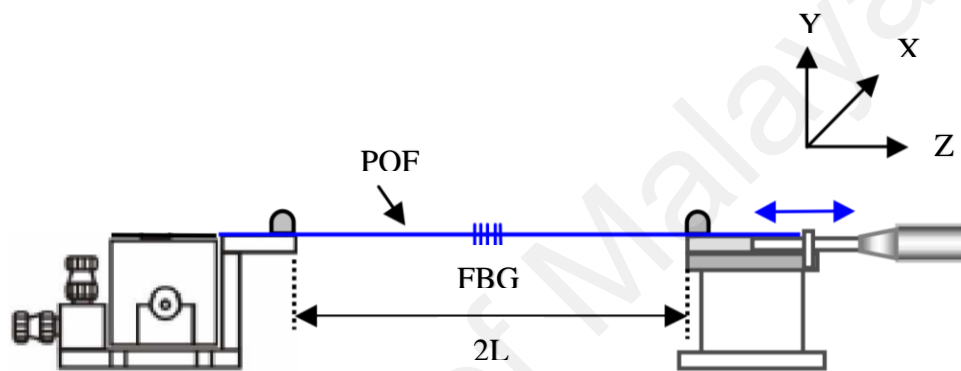


Figure 2.10: Experiment setup for implementation of polymer FBG-based bend test (Chen et al., 2010).

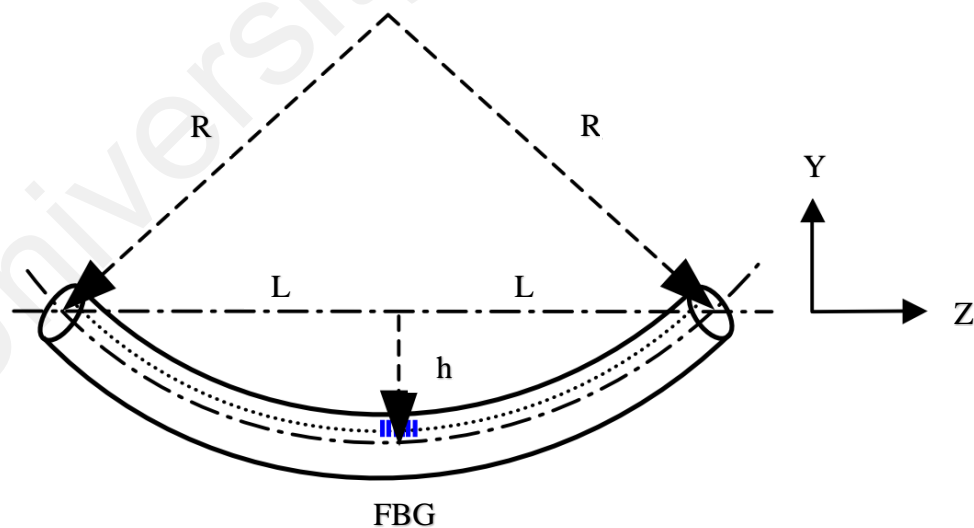
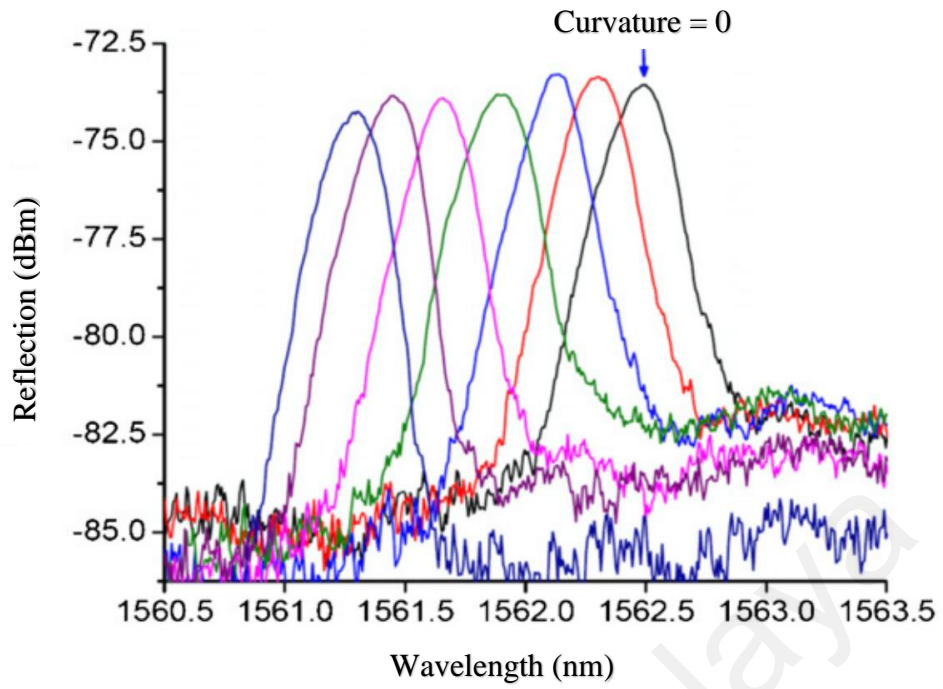
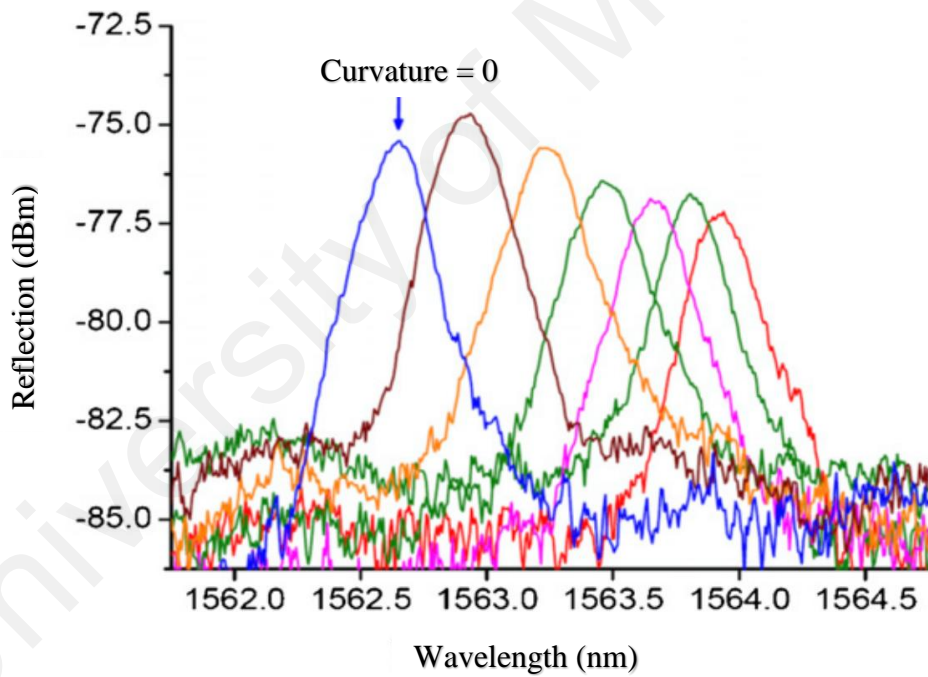


Figure 2.11: Schematic diagram of the eccentric FBG bend at 0° orientation (Chen et al., 2010).



(a)



(b)

Figure 2.12: Bragg peak shift for increasing curvature: (a) at the 0° orientation; (b) at the 180° orientation (Chen et al., 2010)

2.6.2.2. Vertical Displacement Measurement by Curvature Measurement

FBG strain sensors have a high sensitivity to axial strain changes compared to other type of sensors. Therefore, many studies have used its sensitivity to monitor strain. Yau et al. (2011) has used this sensitivity to detect the vertical displacement, where the relationship between curvature (K_i) and strain measurement of FBG strain sensor can be expressed as (Yau et al., 2011):

$$K_i = \frac{-\varepsilon_i}{y} \quad (2.4)$$

Where i is the i^{th} longitudinal location, ε is longitudinal strain and y is distance from the neutral axis of beam cross section. The curvature can be determined by longitudinal strain measurements parallel to the neutral axis. However, the neutral axis may be shifted if damage of beam occurs. Thereafter, two strain sensors placed at different distances parallel to the neutral axis can be used to eliminate the effect of the shift of the neutral axis, as illustrated in Figure 2.13. For two sensors at corresponding longitudinal locations, the curvature is expressed as:

$$K_i = \frac{\varepsilon_i^b - \varepsilon_i^t}{h} \quad (2.5)$$

Where ε^b and ε^t are the bottom and top strain and h is the distance between the sensors. By finding the curvature, the vertical displacement can be evaluated as it is shown in Figure 2.14.

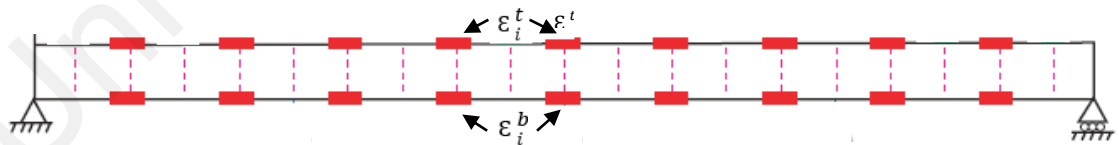


Figure 2.13: Description of FBG locations in RC beam (Yau et al., 2011).

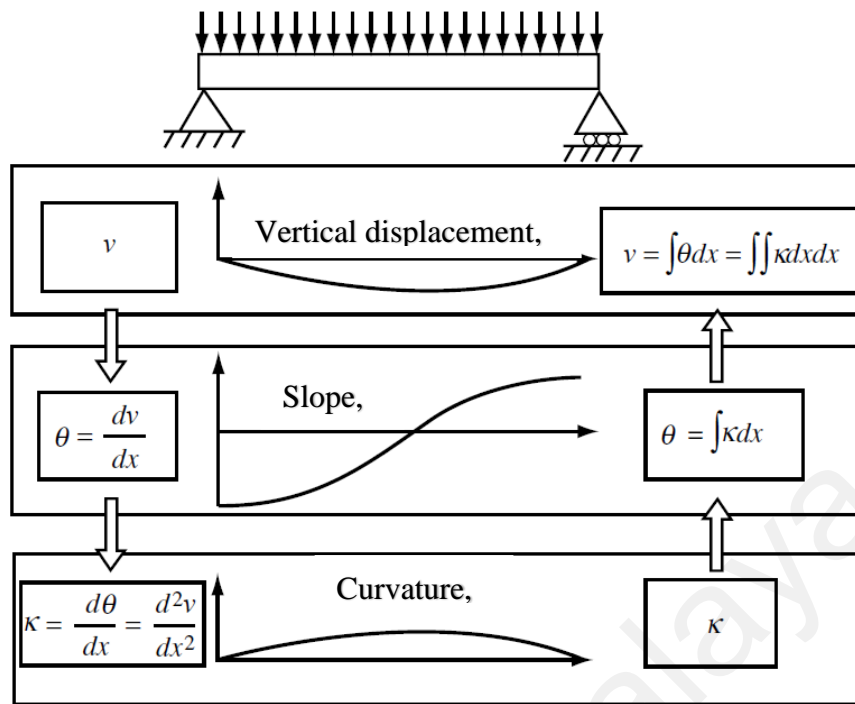


Figure 2.14: The relationships between vertical displacement, slope and curvature (Yau et al., 2011).

2.6.2.3. Vertical Displacement Measurement by Inclination Measurement

With the development of an FBG tilt sensor (Guan et al., 2004) which has all advantages attributed to FBG sensors, high accuracy inclination measurements can be implemented for bridge vertical displacement measurements. As the measurements are only relevant to the geometry of deformed shapes, they will not be affected by the changes of internal deformations. That can increase the practicability of measurements for bridges. Hence, an inclination approach of vertical displacement measurements is proposed by Yau et al. (2013), where Yau proposed an FBG tilt sensor as illustrated in Figure 2.15.

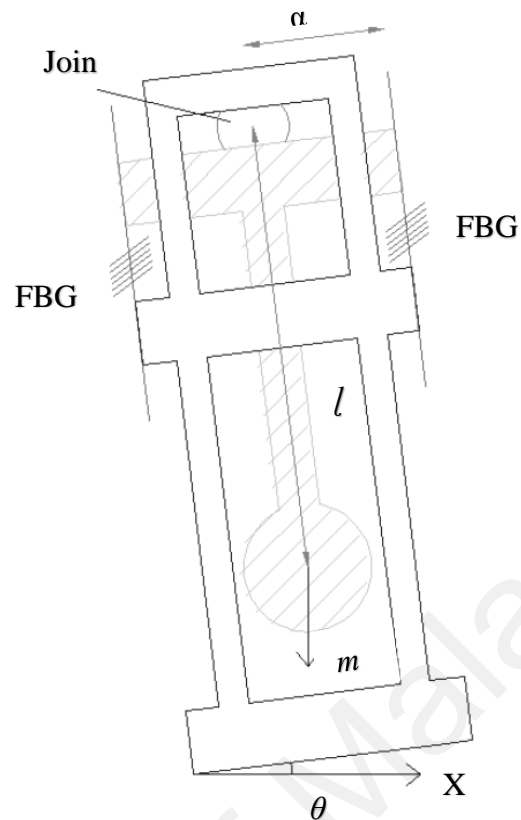


Figure 2.15: FBG tilt sensor (Yau et al., 2013).

The design of the sensor (FBG tilt sensor) is pendulum based. The joint is a key component of the sensor. Since the friction of the joint used is significant to the sensor performance, especially the accuracy, a high precision, low backlash joint is proposed. One end of the joint is embedded at the top of a steel frame. The other end is bonded into a steel rod with two arms. The other end of the rod is bonded with a vertical pendulum. Two FBGs that are pre-strained equally are glued to the two arms at the one end and the frame at the other end.

The sensor amplifies the small force induced by the inclination of the pendulum to a greater axial force into the FBGs. As applying an impact force to the sensor may break the FBGs, a movement stopper is assigned inside the steel frame to prevent the free movement of the vertical pendulum while transporting and handling the sensor. Additionally, it can control the vertical pendulum movement within the ultimate

inclination range when an over inclination is accidentally applied to the sensor. The moment the sensor is inclined about x-axis, the axial strain is induced to the FBGs to keep the vertical pendulum in equilibrium. By finding the angle the vertical displacement can be found as shown in the previous Figure 2.14.

2.6.3. FBG Parameters

In the previous sub-sections (2.6.1 and 2.6.2), wavelength shift of the reflected peak is the main parameter used in FBG sensing. The wavelength shift can be correlated to pressure (Bock et al., 2007), temperature (Lim et al., 2002), strain (Lim et al., 2002), and force (Ma et al., 2012) based on the FBG instrumentation and mounting technique used. However, other studies have used the Refractive Spectrum Shape (RSS) itself as a sensing parameter. The shape characteristics (power reflection, occurrence multiple peaks and the broader of wavelength width) of the reflected spectrum changes due to two reasons according the literature. The two causes of the spectrum change are microcracks in the FBG or stress perturbed strain field on the FBG from the damaged composite material that encapsulates the FBG. The literature in this section focuses on the studies which used the shape changing of reflective spectrum as a parameter to monitor damage in different cases.

Shin et al. (2014) has found that the FBG reflected peak in the spectrum gradually submerged into a rise of background intensity as internal damages progressed in the composite material (resin) around the FBG. Shin considered changing of reflected spectrums' characteristics as damage detection parameter as shown in Figure 2.16. Shin concluded that the change in the FBG spectrum is not a result of deterioration/damage to the sensor. The change in the spectrum is caused solely by the damages initiated in the composite material by the impact and aggravated by fatigue loading. Also, Shin

concluded that the FBG spectra had a single sharp peak, which will be detected to monitor any mechanical or thermal stress. If the FBG spectrum has not changed while the wavelength is shifting that suggest the strains induced to the FBG did not cause significant damage in the composite material. Therefore, the status of the FBGs in the specimen was not under stress perturbed the strain field and caused steep strain gradient in the vicinity of the FBGs or the FBG has microcracks (Shin et al., 2014). On the other hand, if the FBG RSS changed that means there is a microcracks in the FBG or there is stress perturbed strain field on the FBG from the damaged composite material that encapsulates the FBG. It is to be noted, even though the FBG spectrum gradually submerged into a rise of background intensity the peak can still be recognized during the extent of the test. The microcracks in the FBG can cause stress concentration which alters the localized refractive index through the photoelastic effect (Lin et al., 2001) and perturbs the periodicity of the grating. However, his study concluded that the cause of the change of RSS is the stress perturbed strain field on the FBG from the damaged encapsulation composite material, where the FBG did not show any visibility of any microcracks.

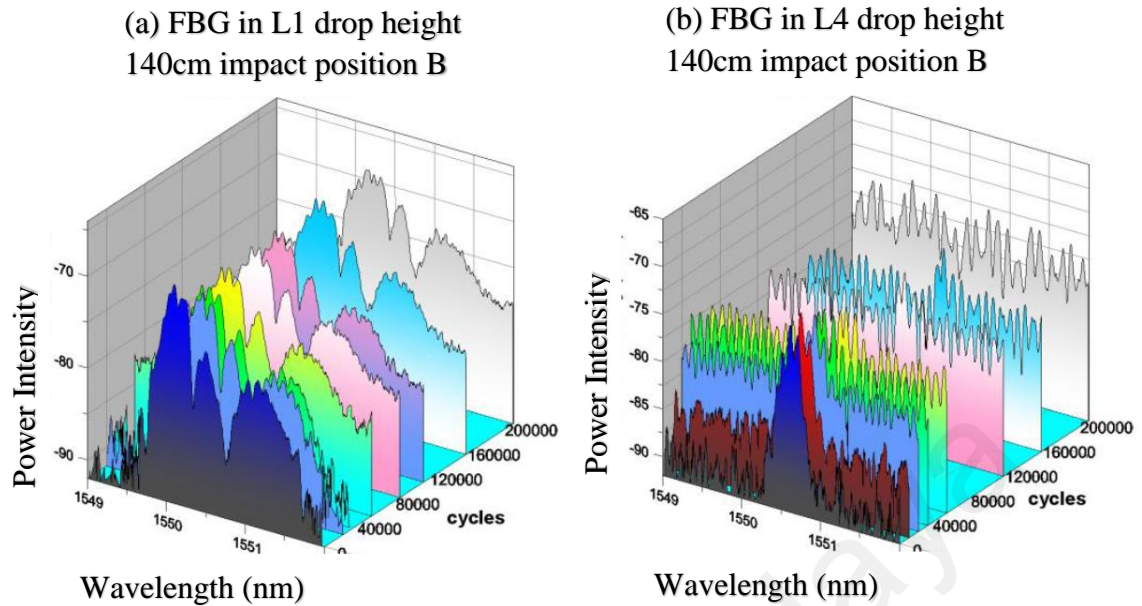


Figure 2.16: Spectra changes from embedded FBGs in (a) L1 and (b) L4 with various fatigue cycles under a 140 cm drop height and impact at position B (Shin et al., 2014).

Trilaksono et al. (2013) has performed two loading cases using ideal loads to create a secondary bending moment and bearing loads in the stiffness-mismatched structure to determine the distribution of load in a combined joint. The bending test's results showed that the normalized power reflection could not be used as an indicator of delamination growth because of the normalized intensity value, which remained nearly the same during a loading run, and the line's slope was small. However, the normalized wavelength over the loading run could more clearly be used as a damage growth indicator. After damage occurred, the normalized wavelength curve increased significantly as the load increased. As a result, the normalized wavelength can be used to quantitatively measure damage in a uniform strain failure. In contrast, the tension loading tests' results showed different indication. The results indicate that the normalized power reflection and wavelength can be used as a tracking parameter for delamination growth because the occurrence of multiple peaks with broader wavelengths can be clearly seen when the damage occurred. From his study the occurrence of multiple peaks and the broader wavelength can be used as a tracking parameter for delamination growth (see Figure

2.17), however, for the bending test the wavelength shift can be considered the only damage indicator.

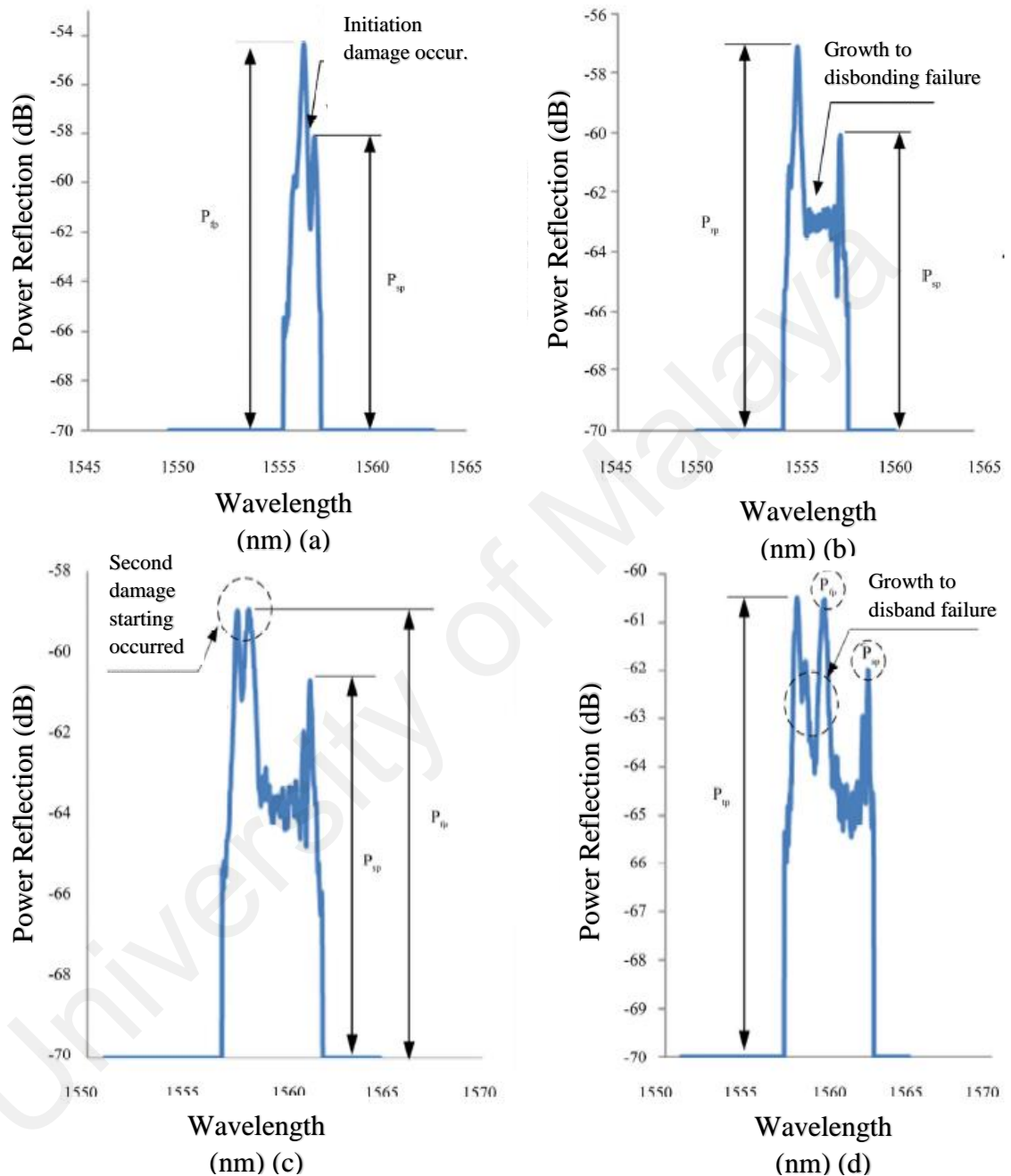


Figure 2.17: (a), (b), (c) and (d) Evolution of reflected FBG spectrum shape under tensile loading (Trilaksono et al., 2013).

Trilaksono et al. (2014) has used FBG strain sensor to quantitatively predict the damage growth. His approach also used the change in the FBG spectrum reflection shape to monitor the damage. Trilaksono used a spectrum analyzer (MS9710C, Anritsu Co.) to

measure the changes of the reflected spectrum shape (spectrum reflection). A direct tensile test was performed on a stitch laminate specimen which contained an FBG strain sensor for monitoring. The spectrum of the FBG character was monitored and there was more than one peak in the spectrum. Then the peak disappeared with correlation to damage until it became a normal class fiber without any Bragg grating. Figure 2.18 illustrates from left to right the original spectrum without FBG peak, spectrum with FBG peak, the evolution of the FBG spectrum when damage occurred, and finally the evolution of the spectrum when almost all the grating periods of the FBG are broken.

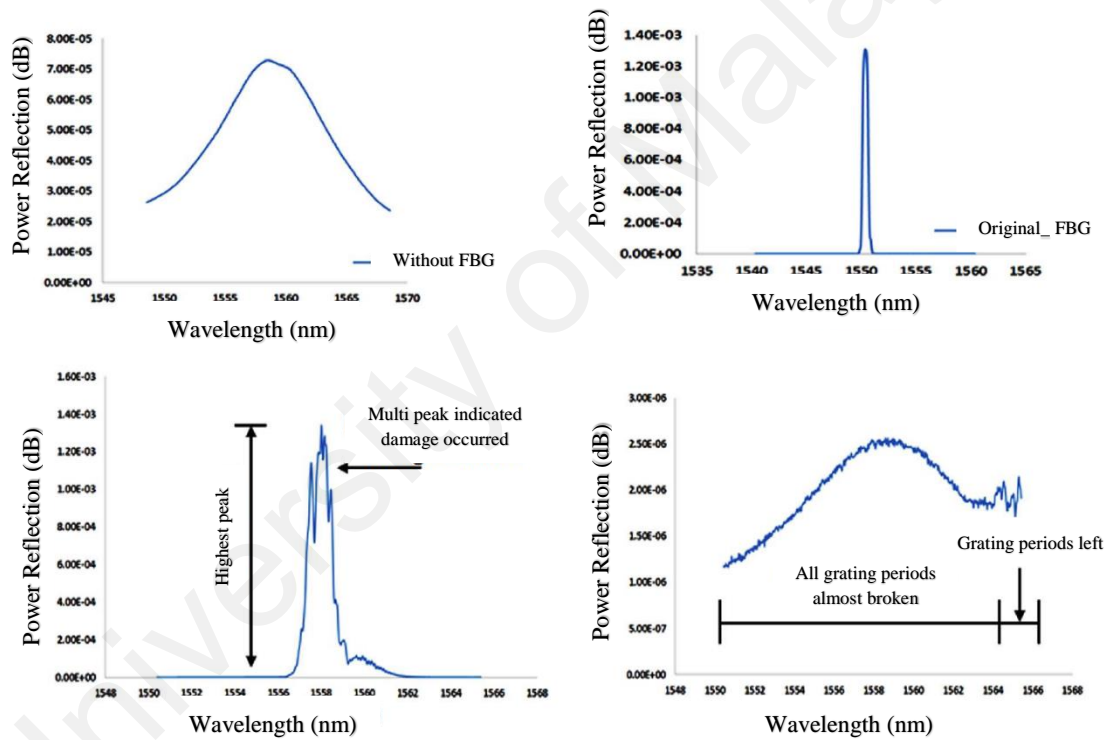


Figure 2.18: Spectrum of the FBG character (Trilaksono et al., 2014).

The multippeak is an indication of damage of the FBG strain sensor, however, this type of multi peak was happening along with a constant pattern of the height. The reflective peak value has the tendency to decrease gradually until the failure of the stitch laminate specimen. The reduction of the reflective peak height from the FBG reading during load ran in a tensile test up to the breakage of the specimen is shown in Figure

2.19. Trilaksono et al. (2014) used this reduction of the highest peak value as an indicator to determine the degradation of the strength of the material in addition to the occurrence of multi-peaks.

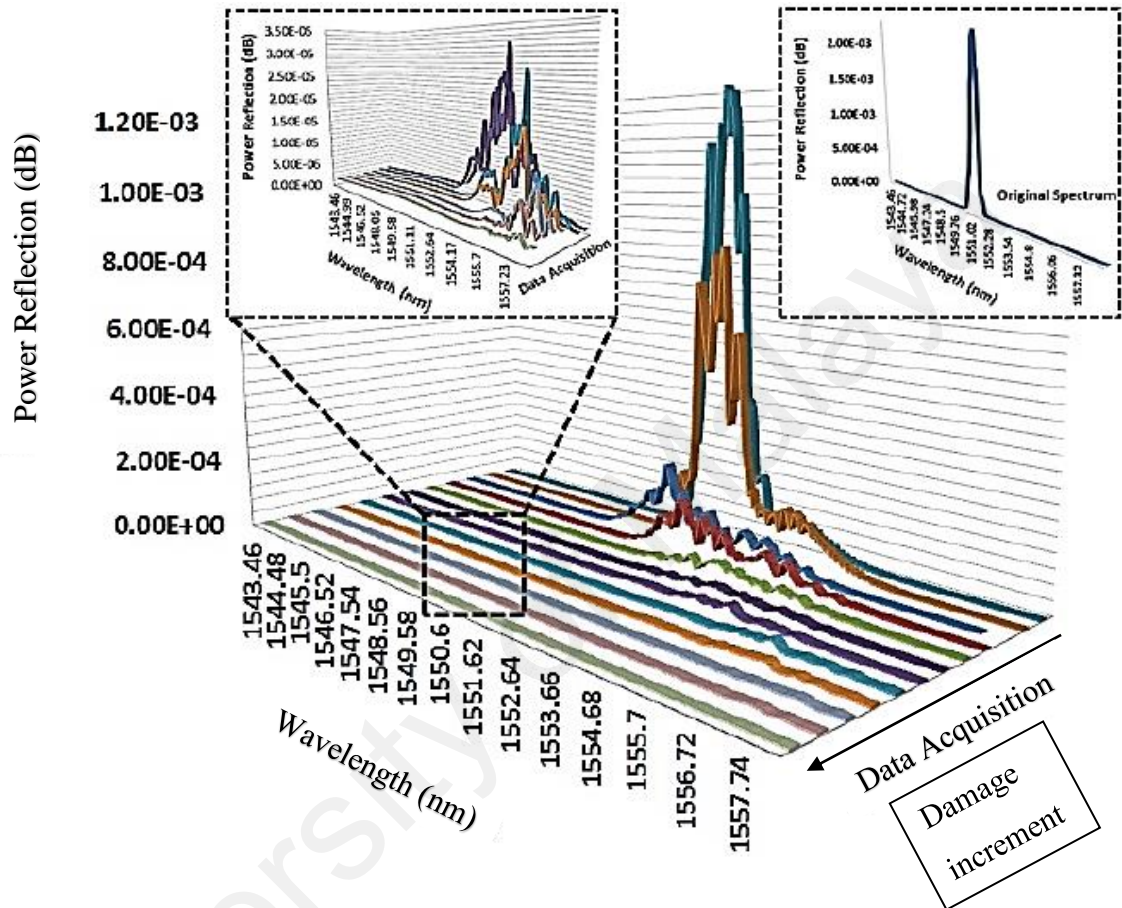


Figure 2.19: Spectrum evolution on profiling tensile test (Trilaksono et al., 2014).

2.7. Statistical Analysis Controlling

Recent research has begun to recognize that the SHM problem is fundamentally one of the Statistical Pattern Recognition (SPR) and a paradigm (Farrar & Worden, 2007). The review of the technical literature presented by Doebling et al. (1996) and Sohn et al. (2003) show an increasing number of research studies related to damage identification. These studies identify many technical challenges to the adaptation of SHM that are common to all applications of this technology. These challenges include the development of methods to optimally define the number and location of the sensors; identification of

the features sensitive to small damage levels; the ability to discriminate changes in these features caused by damage or caused by changing environmental and/or test conditions; the development of statistical methods to discriminate features from undamaged and damaged structures; and performance of comparative studies of different damage identification methods applied to common datasets. These topics are currently the focus of various research efforts by many industries including defense, civil infrastructure, automotive and semiconductor manufacturing where multi-disciplinary approaches are being used to advance the current capabilities of SHM and CM.

There are many ways by which one can organize steps to perform the SHM process. For example, Farrar and Worden (2007) defined the SHM process in terms of a four-step statistical pattern recognition paradigm. This following four-step process includes:

- (i) operational evaluation,
- (ii) data acquisition, normalization and cleansing,
- (iii) feature selection and information condensation, and
- (iv) statistical model development for feature discrimination.

All papers published in the fields of SHM and CM address some parts of this paradigm, but the number of studies that address all portions of the paradigm is much more limited (Farrar & Worden, 2007). As data can be measured under varying conditions, the ability to normalize the data becomes very important to the damage identification process. As it applies to SHM, data normalization is the process of separating changes in sensor reading caused by damage or caused by varying operational and environmental conditions. One of the most common procedures is to normalize the measured responses by the measured inputs. Thus, when environmental or operational variability is an issue, the need can arise to normalize the data in some time-related

fashion to facilitate the comparison of data measured at similar times of an environmental or operational cycle. Sources of variation in the data acquisition process and with the system being monitored need to be identified and minimized to the extent possible. In general, not all sources of variability can be eliminated. Therefore, it is necessary to make the appropriate measurements such that these sources can be statistically quantified. Variability can arise from changing environmental and test conditions, changes in the data reduction process and unit-to-unit inconsistencies (Farrar & Worden, 2007). One of the most used SPR is control charts, where they have been used firstly for monitoring product's qualities. However, due to its efficiency the control charts have been used to detect the changes of the sensors' data measured such as accelerometer (Fugate et al., 2001).

2.7.1. Control Charts

Monitoring quality processes is the procedure to insure the quality of products to following the standards. As mentioned earlier that many industries have used control charts to monitor the quality process which has shown its efficiency (Jensen et al., 2006). The application of control charts is divided in two separated phases. Phase I concerns producing control charts based on the historical data reference (control state). It is to be noted that in this phase the reference data will be assessed to ensure that it is a representative of the whole process. The end product of phase I is control limits which will be used in phase II. The monitoring process based on the control limits will be done in Phase II, when the observed chart statistics are plotted within the control limits of the reference data the process is deemed stable or in control. In other words, the observed chart statistics are following the quality of the reference data. On the other hand, when the observed chart statistics are plotted outside the control limits of the reference data are

considered out of control. Out of control process is a sign to perform a corrective action regarding the process.

Autocorrelation data cannot be used in control chart analysis without modification analysis to eliminate their autocorrelation. The data should be modelled in an appropriate time-series model such as auto-regressive. Auto-Regressive (AR) model eliminate the correlation between the data observed, which will eliminate the false alarm given by the control chart constructed from correlated data. In other words, the control charts can be more efficient to give the correct alarm (Montgomery, 2007). The end product of the AR is the residual errors that fitted an AR model. The residual errors then will be used in the control charts rather than the actual measured data to detect any changes. An AR model with ρ autoregressive terms, $AR(\rho)$, can be written as:

$$X_{(t)} = \alpha + \sum_{j=1}^{\rho} \emptyset_j X_{(t-j)} + Z_{(t)} \quad (2.6)$$

The $X_{(t)}$ are measurements observed at time t and $Z_{(t)}$ is an unobservable random error with mean 0 and constant variance. The mean of the $X_{(t)}$ is μ for all time t . The \emptyset_j and μ are unknown parameters that must be estimated. In this study, the AR coefficients are estimated by the Yule-Walker method (Brockwell & DAVIS, 1991).

The AR should fit the measured data which depend on the order of it. There are a variety of techniques for choosing the model order, such as Akaike's information criterion (AIC) and for estimating the parameters. These techniques can be found in most textbooks on time series analysis, e.g. (Brockwell & DAVIS, 1991). As mentioned earlier the AR model is to uncorrelate the measurements, where the residual errors will be used for the control charts. In other words, the residual errors of the fitted AR model will be considered as the damage sensitive feature (DSF).

The control limits that constructed from the reference measured data are considered the undamaged measurements. Therefore, when there is a new measured data the undamaged control limits will be used to check if the measured data is considered under control or out of control. The chart statistics of the new measured data residual errors will chart beyond the reference control charts if there is damage. Fugate et al. (2001) has used control charts as a statistical pattern recognition paradigm to distinguish between damaged and undamaged state of structure. Fugate used accelerometers during the vibration test and Fugate used an SPC which is a method of quality control of a process by using statistical methods. In the study, Fugate constructed control charts. Firstly, a mean and variance were found based on the undamaged structure, however, when there is any damage the mean and the variance should change which will be shown in the control charts. The control chart based on the undamaged measurements from the accelerometer measurements is made of three lines, where the center line is the mean of the DSF. The upper limit and the lower limit are the mean plus constant multiply with the variance of the DSF. The constant changes based on the type of the control chart used. It is to be noted that most of the DSFs should fall between the upper and lower limits of the control chart, the percentage of the outlier which exceeds the limits changed based on the constant chosen, which is depend on the type of control chart. Moreover, the charted data should not have an obvious pattern (El-Midany et al., 2010) such as five charted data above the mean followed by five charted data below the mean line. Plotting the individual measurements on a control chart is referred to as an X-chart or a Shewhart chart (Montgomery, 2007). It is to be noted that any distribution of the detected charted data can lead to the increment of the outliers' percentage. This distribution can be caused from many sources such as damage to the structure or operational or environmental factors. Therefore, the percentage of outlier it is not always a sign of damage, it is just a

justification of a change in the data measured. An inspection of damage is important to insure the source of the outliers' percentage.

Forming a rational subgroup of size n can allow the control charts to detect the change of DSFs mean, in this step each subgroup mean will be computed. The center line of the control chart will not change, which is the mean of the subgroup means. However, the standard deviation of the charted values will be the same divided by the square root of the subgroup size. This method of control charts is called an X-bar chart, where the control limits will become $\mu \pm k \sigma/\sqrt{n}$ (Montgomery, 2007). The rational subgroup size n should be chosen in the way that the observations within the same group are more similar than the observations between groups. In other words, if n is too large the change of the means will be undetectable. Also, by applying the subgrouping technique the distribution of the means can be considered as normal distribution.

Fugate et al. (2001) has used the AR order as 5 and the subgroup size was 4 to construct X-bar control chart. The steps to construct the control chart are shown in Figure 2.20. After the DSF has been defined which is in this case is the residual errors of fitting the fifth order of the AR (5). The residual errors should be normalized by subtracting each residual from the residuals mean and dividing it with standard deviation of the residuals computed. Then the residual errors sub grouped, each subgroup formed from 4 residual errors. The mean and the variance of each subgroup is computed where the charted values are the means of the subgroups. Due to the normalization of the residuals the center line will be 0, on the other hand the estimated population standard deviation that represent the pool of the residuals are the square root of the averaged subgroup variances. The upper and lower X-bar control charts are:

$$UCL, LCL = 0 \pm Z_{\alpha/2} \frac{S_p}{\sqrt{n}} \quad (2.7)$$

Where UCL and LCL and the upper and lower control limits respectively, and Z_α is the value of a standard normal variance which has probability α of being exceeded.

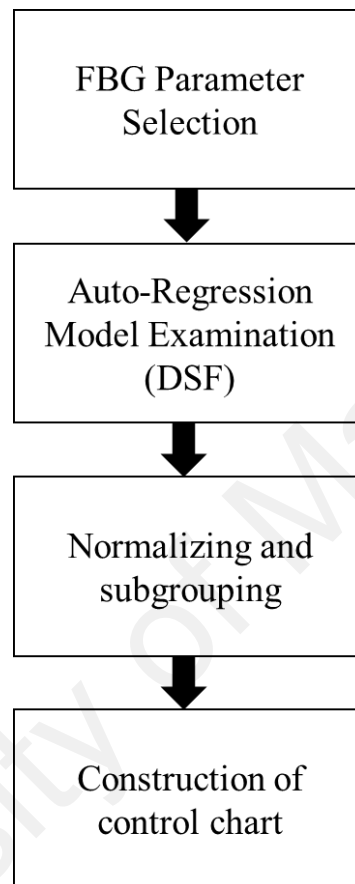


Figure 2.20: Construction control chart scheme.

As mentioned earlier control charts are useful in determining whether a process is behaving as intended or if there are some unnatural causes of variation (measurements). However, in addition to charted points fall outside the control limits (outliers) as an indicator of the quality (in control or out of control) of a process, a series of points exhibit an unnatural pattern (also known as nonrandom variation) is also an indication of a process quality. Analysis of unnatural patterns is an important aspect of SPC (Pham & Wani, 1997; Perry et al., 2001; Guh, 2002; Hao et al., 2005; El-Midany et al., 2010). These unnatural patterns provide valuable information regarding potential for process improvement. There are six main types of control chart patterns that may exist in

Shewhart X-bar control chart, namely, random, cyclic, decreasing trend, increasing trend, downward shift and upward shift (Hao et al., 2005). Except for the random pattern, the existence of other unnatural patterns indicate that the process is abnormal. Recognition of these unnatural patterns and further analysis would lead to identification and elimination of sources of disturbances. El-Midany et al. (2010) has classified the patterns in 4 types as shown in Figure 2.21. The presence of unnatural patterns indicates that a process is affected by assignable causes, and corrective actions should be taken.

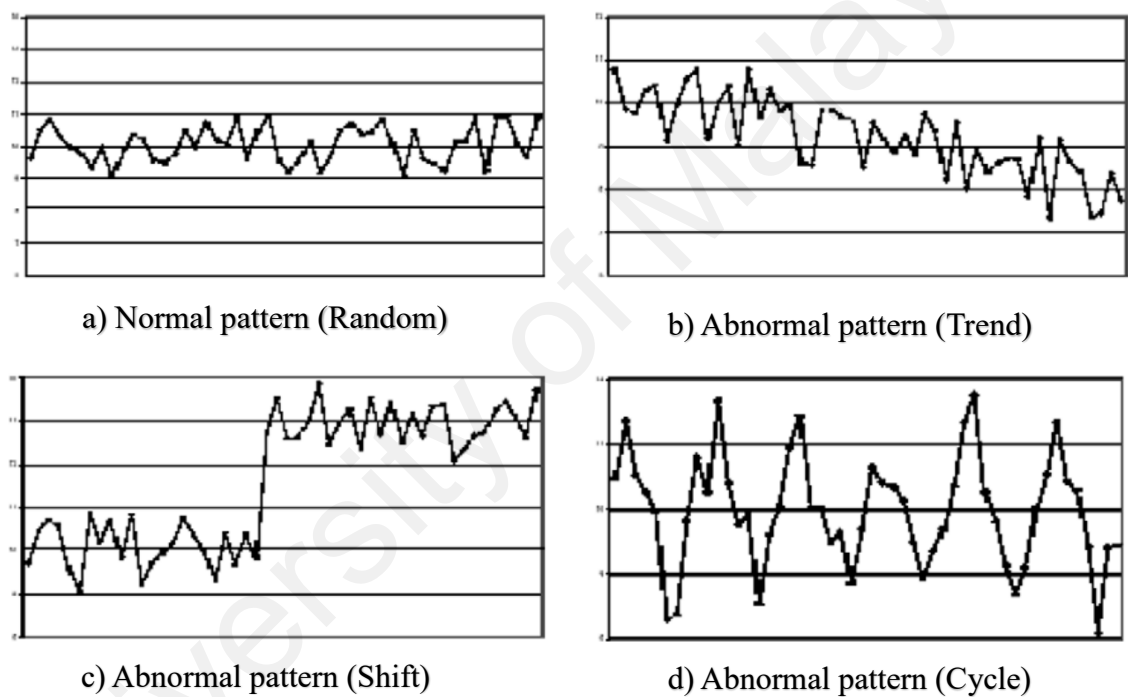


Figure 2.21: Typical normal and abnormal patterns (El-Midany et al., 2010).

CHAPTER 3: MATERIALS AND METHODS

3.1. Introduction

This chapter describes the proposed instrumentation method of Fiber Bragg Grating (FBG) strain sensing. The proposed method was investigated through two phases of experiments. Phase 1 investigated the FBG strain sensing capability to detect corrosion formation and provides protection for the FBG sensor, while Phase 2 investigated the capability of the FBG strain sensor not only to detect corrosion process but also to evaluate the vertical displacement of RC beams. Figure 3.1 shows the flow chart of this chapter, where objective 1 was investigated throughout Phase 1 experiment while objective 2 and 3 were investigated throughout Phase 2 experiment and analysis.

University of Malaya

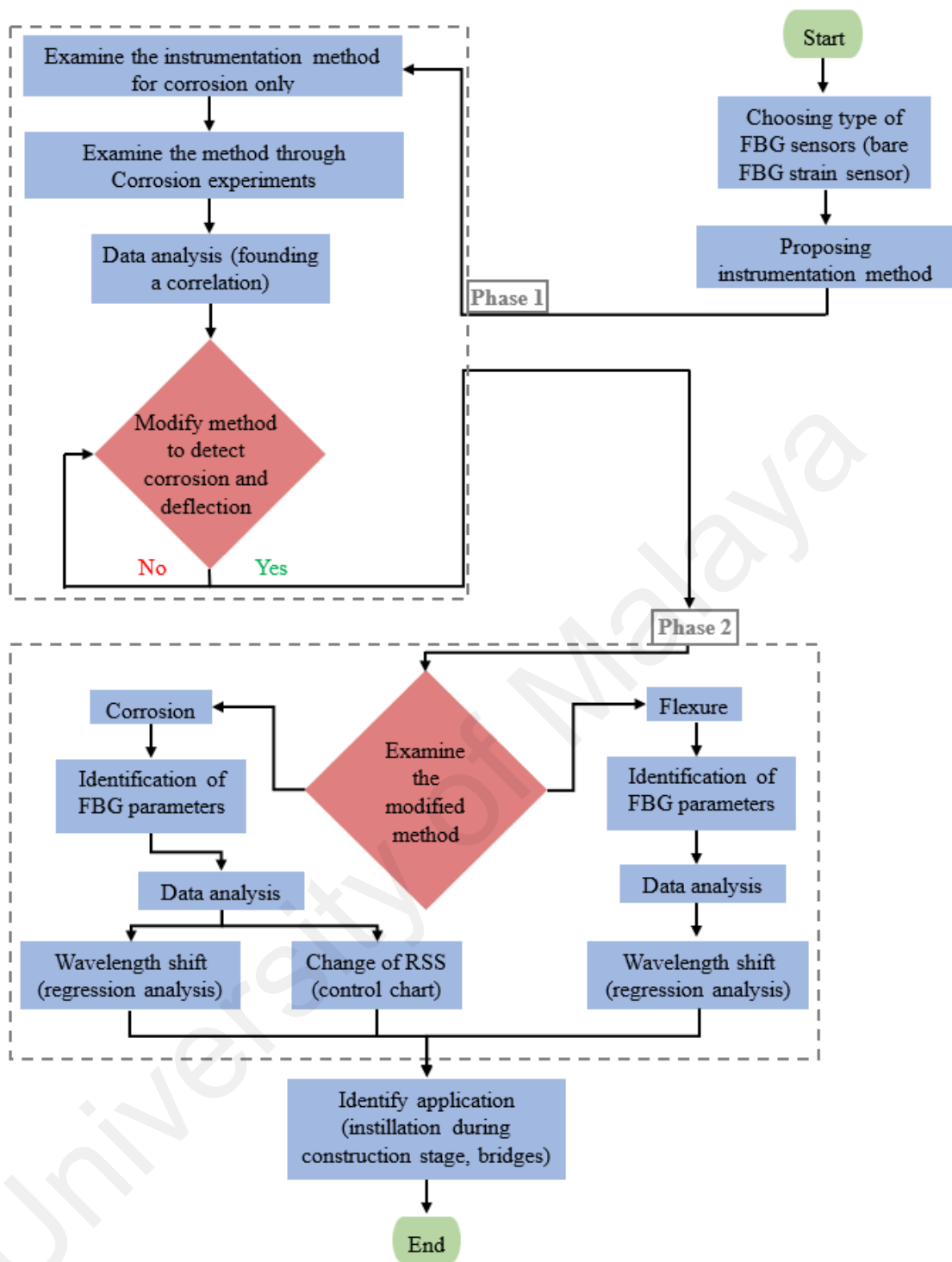


Figure 3.1: Flow chart for the Methodology.

3.2. Materials and Specimens

3.2.1. Concrete

Concrete density should be essentially high to ensure high strength and good provision of cover to steel reinforcements. However, in this study the density of the concrete was purposely minimized, with reduced concrete cover to facilitate faster corrosion process undertaken in the laboratory (Chindaprasirt et al., 2008). In other words, by making the concrete more porous, density was reduced and permeability became higher to allow for the corrosion steel reinforcement to be simulated in the laboratory using the impressed current method at a faster rate to obtain different levels of corrosion for respective specimens.

Two 200 x 100 mm cylindrical concrete specimens were prepared for Phase 1 test in the study, as shown in Figure 3.2. Ordinary Portland cement was used as the binder. The concrete mix was designed by referring to a previous work (Grattan et al., 2007) with a binder to water ratio of 0.55, design in accordance to British Standards European Norm (BS EN) and American Society for Testing and Materials (ASTM) standards. The proportional ratios for binder, fine aggregates and coarse aggregates were 1:1.65:3, respectively, with maximum coarse aggregate size of 10 mm. A structural grade deformed steel bar of 10 mm in diameter was placed at the center of the specimen. After casting, the specimens were demoulded after 24 hours and cured inside a water tank.

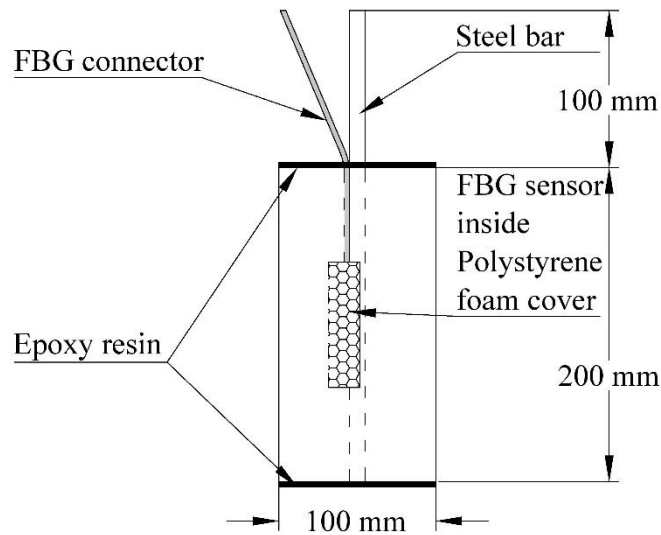


Figure 3.2: Details of concrete cylinder specimens for Phase 1 experiment.

In addition to the cylindrical specimens used for corrosion monitoring, five (control and corroded beams) RC beam specimens were prepared for Phase 2 of testing (Table 3.1). Schematic diagram of a beam specimen is given in Figure 3.3. All beams specimens were reinforced for tension and compression by 16 mm and 8 mm with high yield deformed steel bars complying with BS8110 specifications. For shear reinforcement, smooth mild steel bars of 6mm in diameter were used, with the link being spaced at 100 mm. The concrete mix that was used in this stage has cement: sand: coarse aggregate ratio of 1: 1.43: 3.48 (373 kg/m^3 , 530.7 kg/m^3 , 1299.3 kg/m^3 respectively). Crushed granite stones with a maximum size of 10 mm were used as coarse aggregate, with water-to-cement ratio of 0.55. The size of Phase 2 specimens required different mix which was designed to allow a higher rate of chloride ion penetration into concrete, by having higher porosity, for generating corrosion to steel reinforcement faster. During casting, a vibrating rod was used to compact the concrete mix poured into beam moulds. The beam specimens were demoulded three days after casting and cured twice a day through twenty-eight days from the day of casting. In addition to beam specimens, 100 mm x 100 mm cubic specimens, 100 x 200 mm cylindrical specimens and 150 mm x 300 cylindrical specimens were also prepared using the same mix for purpose of testing the

concrete mechanical properties. Concrete density was aimed to be lower than the normal concrete density (2400-2500 kg/m³), therefore, porous concrete was used. Porous concrete can be achieved by reducing fine aggregates while increasing coarse aggregate percentage in concrete mix (gap graded concrete) (De Larrard, 1999) and increasing cement/aggregate volume ratio (Chindaprasirt et al., 2008). It is to be mentioned, this type of concrete is used in thermal cycling conditions (Khudhair & Farid, 2004).

Table 3.1: RC beam specimens.

Beam No.	Beam Name	Theoretical Corrosion level (%)	Time required to corrode (hour)
1	BM1	0%	0
2	BM2	2%	48
3	BM3	4%	96
4	BM4	6%	144
5	BM5	10%	240

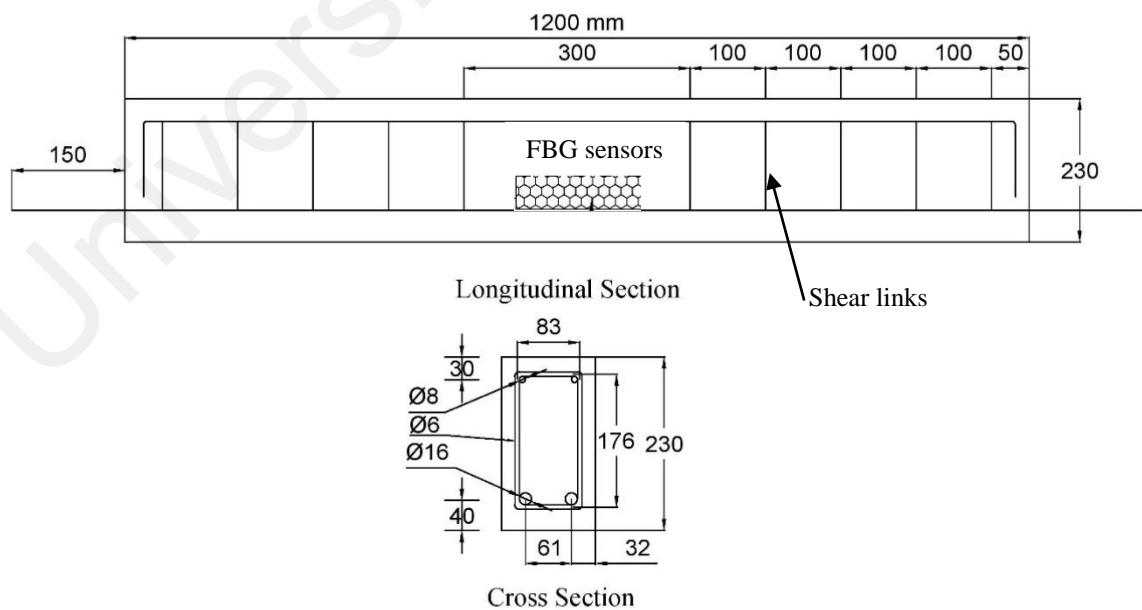


Figure 3.3: Details of concrete beam specimens for Phase 2 experiments.

3.2.2. Corrosion Acceleration of Steel Reinforcement

Both Phase 1 and 2 specimens went through accelerated corrosion experiments. To accelerate corrosion of steel reinforcement, the impressed current technique was used. To perform the technique a Direct Current (DC) power supply was needed, where the positive terminal was connected to the embedded steel bar to form the anode. Next, to form an electrical circuit, the other terminal (negative) was connected to a bare steel bar immersed in the same water tank as the specimen. The other steel bar became the counter-electrode (Caré & Raharinaivo, 2007). The solution was electrically conductive due to the 5% of sodium chloride. Therefore, the oxidation of steel bar can be increased by removing electrons from the anode bar to form Fe(OH)_2 and Fe(OH)_3 (Chen & Mahadevan, 2008). Accordingly, the embedded steel reinforcements (anode) would be corroded while the bare steel bar being protected from corrosion due to cathodic protection shield effect (Chess & Broomfield, 2003).

The Faraday's law adopted in this study to establish different corrosion levels of steel reinforcement corrosion. The law states that 96,486.7 Coulombs (equal to one Faraday) of charge transfer will oxidize or reduce one gram equivalent weight of the material involved in the electrochemical reaction (Bushman & Engineer, 2000). The law is expressed by an equation, in which the amount of corrosion is a function of voltage, amperage and time. The designed amount of corrosion in this study was calculated according to Faraday's law. The designed amount of corrosion, in terms of rate of steel mass loss due to corrosion can be estimated by the following equation (Chen & Mahadevan, 2008):

$$\frac{dM_s}{dt} = 2.315 \times 10^{-4} \times I_{corr} \left(\frac{g}{s}\right) \quad (3.1)$$

Where, M_s is mass of steel loss consumed in gram, t is time in second and I_{corr} is the amount of current flowing through the electrochemical corrosion cell in Ampere. The steel corrosion by percentage of mass loss can be computed by the following:

$$M_{\%} = \frac{M_s}{M_o} \times 100 \quad (3.2)$$

Where, $M_{\%}$ = The steel corrosion by percentage of mass loss (%), and M_o = Original weight of steel bar (g). It should be noted that the designed degrees of corrosion as well as the corresponding amounts of corrosion Eq. (3.1) were used only to roughly control the electric current and the time of corrosion in the corrosion experiments. The actual degree of corrosion, or corrosion level, was measured at the end of the experiments, where all specimens were hacked open to weight their actual steel reinforcements after corrosion. The corrosion product was removed from steel reinforcements by using corrosion-inhibited HCl solution (Torres-Acosta et al., 2007).

3.3. FBG Sensor Mounting Methods

The proposed mounting method should accommodate free formation of expansive rust on steel, without sacrificing the sensitivity of corrosion detection and evaluation. Polystyrene foam was proposed to be used as a buffer material that would provide protection and sufficient room for the FBG strain sensor to reflect any strain change in accordance to any stress that takes place as a result of corrosion activities. It is to be noted, the mounting method was slightly modified to serve the purpose of Phase 2 experiments. The FBG strain sensor used for Phase 2 was fixed with epoxy at one end and by foam strip on the other end. While, in Phase 1 the FBG strain sensor fixed with epoxy at both ends of the sensing area. The two proposed methods will be described in detail in this section.

Phase 1 and 2 experiments adopted the same principle for corrosion detection using FBG mounting method. The sufficient room made by polystyrene foam and the sensitivity of the FBG strain sensor are the two keys to effectively detect any strain that occurs. The FBG sensor was laid over the grinded area of steel reinforcement to sense any volume changes due to corrosion of steel reinforcement. The moment the grinded area under the FBG sensor gets corroded, the corrosion product will induce stresses on FBG sensor due to its higher volume compared to steel. Therefore, when the corrosion process continues the corrosion product will accumulate over each other (corrosion-induced expansion (Mao et al., 2015)) causing higher stress on the FBG sensor which will be shown by the wavelength shift of FBG sensor measurements.

3.3.1. Phase 1 Experiment

Phase 1 experiment aims to check the capability of the FBG sensor to detect corrosion formation and monitor its progression, in addition to examining the feasibility of the mounting method to protect the FBG strain sensor. With reference to the arrangement layout shown in Figure 3.4, the polystyrene foam was first cut to give a triangular shaped void, which would later be used to “cover” the steel reinforcement part pre-mounted with FBG strain sensor. Epoxy resin (Araldite Super Strong Steel bonding adhesive) was used to bond the polystyrene foam to steel reinforcement in such an arrangement that the perimeter of the contact area was totally sealed, leaving a gap inside in between the sensor and polystyrene foam. Furthermore, the FBG sensor was fixed on the steel reinforcement by using epoxy, while holes are created on the sides of the polystyrene foam cover. The holes are created in such a way that allows the water to go through without the cement paste, where the cement paste has higher viscosity compared to water. After the hydration reactions take place the cement gets hardened and water can travel through concrete porosity and through polystyrene foam to reach the steel reinforcement bars. Polystyrene

foam was chosen for this study because of its good energy absorption and deformability that are deemed to offer good protection to FBG strain sensor from damaging actions such as concrete pouring, compaction, hydration and other types of stresses under service exposure. Furthermore, polystyrene foam is lightweight, low-cost and can be easily shaped to suit different arrangements.

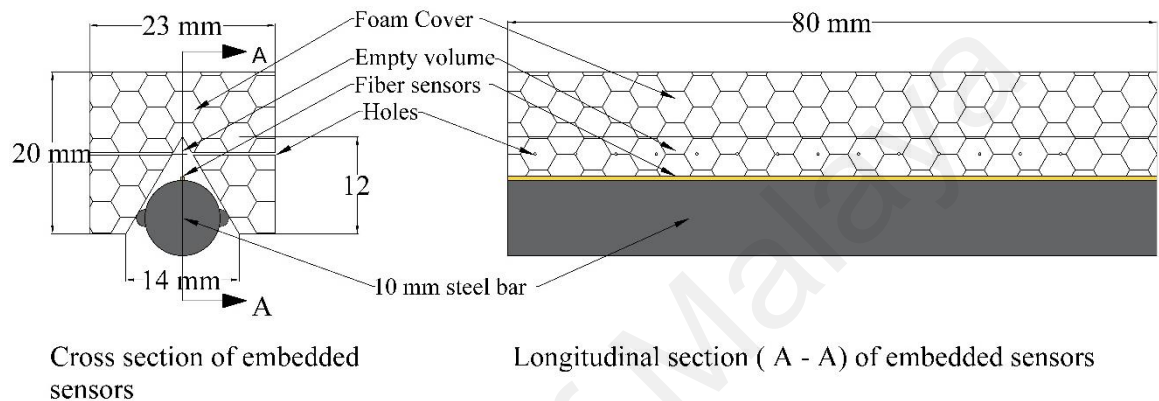
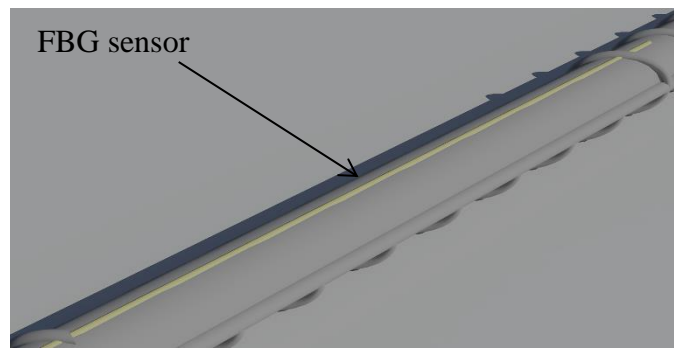
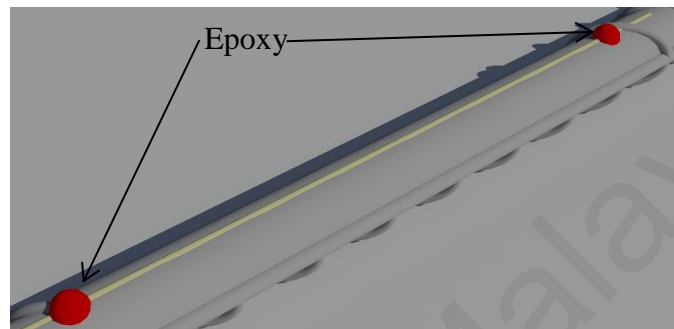


Figure 3.4: Layout of polystyrene foam cover for FBG strain sensor.

Due to the delicate and fragile nature of glass fiber, the mounting surface was carefully grinded and smoothed before the FBG sensor was bonded by epoxy resin. This approach also helped minimize the possibility of erroneous reading due to the uneven strain on the FBG during the corrosion process. The epoxy resin was left to cure for 6, which is specified by the epoxy manufacturer, hours before the polystyrene foam was placed to cover the sensor. Figure 3.5 shows the procedure for preparation and sensor mounting. As for the optical fiber extension which connects the FBG strain sensor with the interrogator (National Instrument PXIe-4844) was housed inside a plastic tube for protection from being exposed to concrete as shown in Figure 3.6.



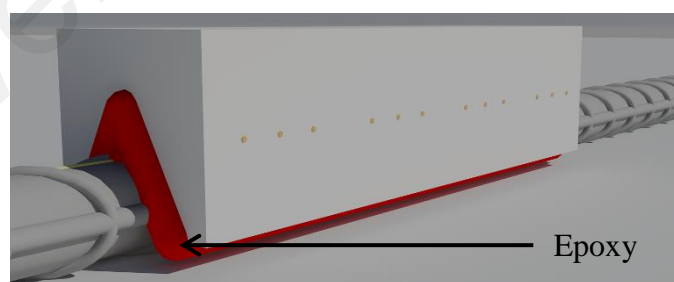
(a)



(b)



(c)



(d)

Figure 3.5: Procedure used for mounting FBG strain sensor on steel reinforcement bar for Phase1. (a) Fiber sensors were placed on the grinded surface of steel reinforcement. (b) The two ends of FBG strain sensor to steel reinforcement were bonded with epoxy resin. (c) Polystyrene foam was placed to cover FBG strain sensor. (d) Epoxy resin was applied to the perimeter of polystyrene foam to seal gap with steel reinforcement.

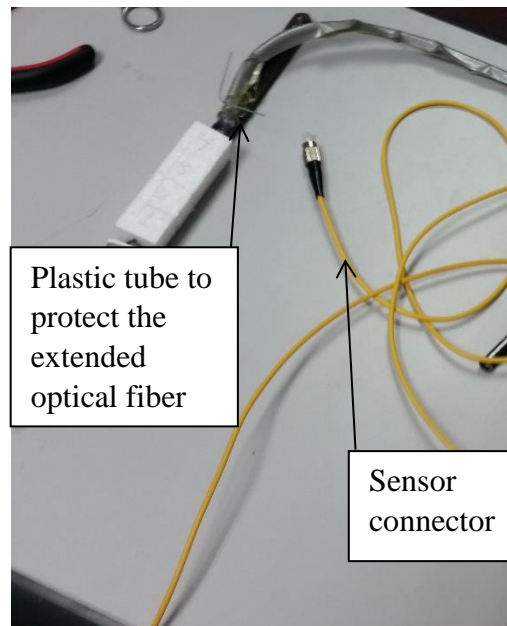


Figure 3.6: Photo of FBG strain sensor mounted on steel bar with polystyrene foam cover.

3.3.2. Phase 2 Experiment

The mounting method of Phase 2 is slightly modified compared to the Phase 1 experiment, where one of the FBG strain sensor end fixed by foam strip. The main reason for using foam strip was to allow the FBG strain sensor to detect the displacement of beam tested, where the foam allows the fiber to slide without damaging the FBG. The second reason was to increase the robustness of FBG sensor for detecting higher level of corrosion. Figure 3.7 illustrates the cross section and longitudinal section of mounting method used in the Phase 2 experiment.

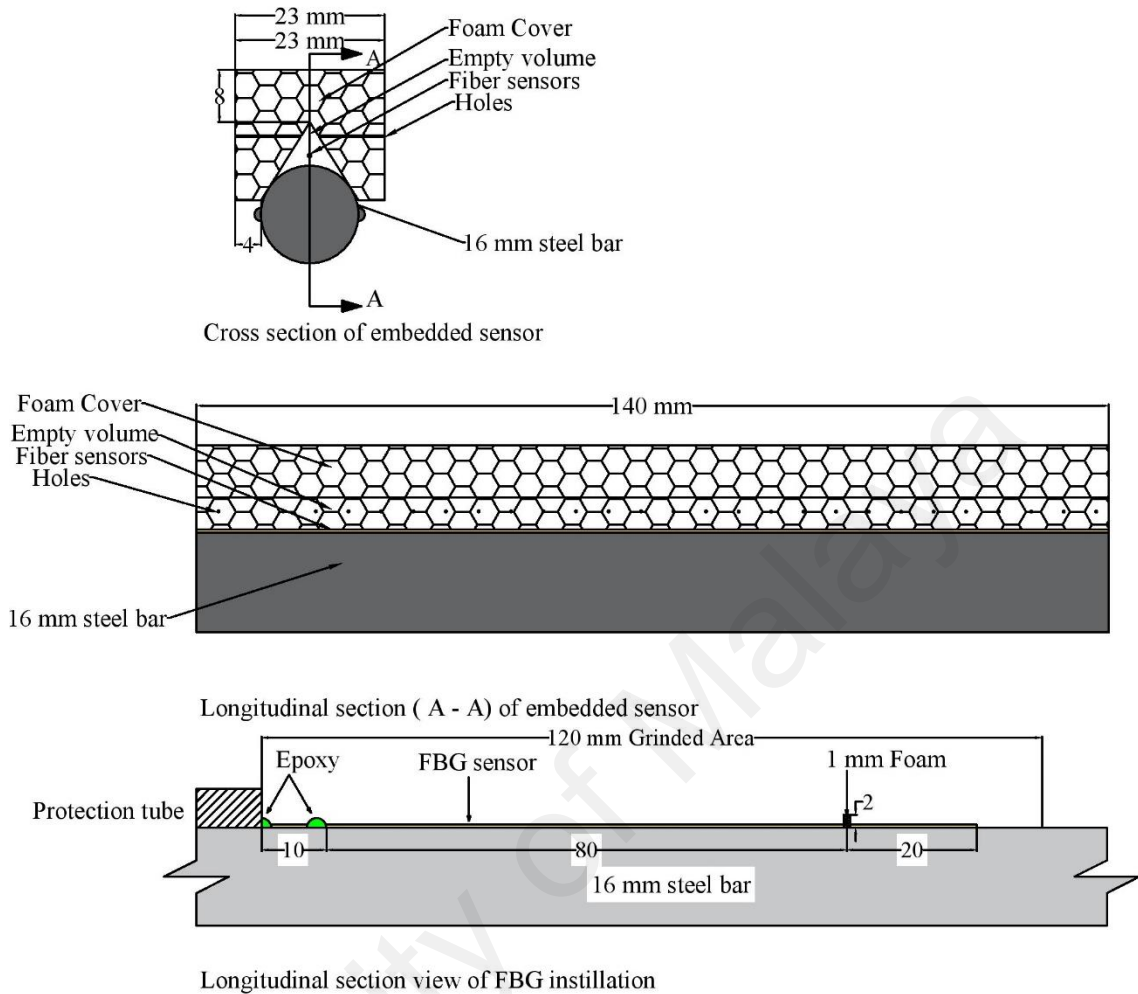


Figure 3.7: Foam cover dimension.

It is to be mentioned that for specimens used in this phase, the foam cover length and the room created by the foam was different from those of the Phase 1 experiment. This is due to the diameter of the steel reinforcement and extra area for the extended FBG from the foam strip end. Even though, the length of the foam cover is considered as un-bonded zone, which is 12 % of the total length of the embedded tensile steel reinforcements, it does not reduce the ultimate load carrying capacity significantly. Mousa (2015) found that 24% of the un-bond length of total length of tensile steel reinforcement can approximately reduce the ultimate load carrying capacity only by 4.2%, and increase the deflection only by 10% at the service load (~30 kN). The Phase 2

mounting procedure followed the same procedure of Phase 1 mounting method. Firstly, the surface of the steel reinforcement was grinded by an electric grinder and then smoothed by sandpaper. The FBG sensor was placed on the flattened area. The FBG was fixed on the steel reinforcement by epoxy. The free end of the fiber was placed at its position by using foam strip (1 mm X 2 mm) to allow the fiber to slides according to corrosion products formation and vertical displacement. The epoxy left for 6 hours to harden, then the foam was mounted over the sensor and attached to the steel bar by using epoxy. Finally, the epoxy hardened and ready to be embedded inside the concrete mould, the steps of Phase 2 are illustrated in . Figure 3.8 to 3.11 show how the glass fiber was mounted on the steel reinforcements, with Figure 3.8 indicating the fibers being laid over the grinded steel area and Figure 3.11 showing the full assembly of reinforcement cage with the FBG sensors protected under the foam covers. It is to be noted that the sensor connectors were inserted into a plastic tube to isolate them from concrete mix (see Figure 3.9 and Figure 3.12b).

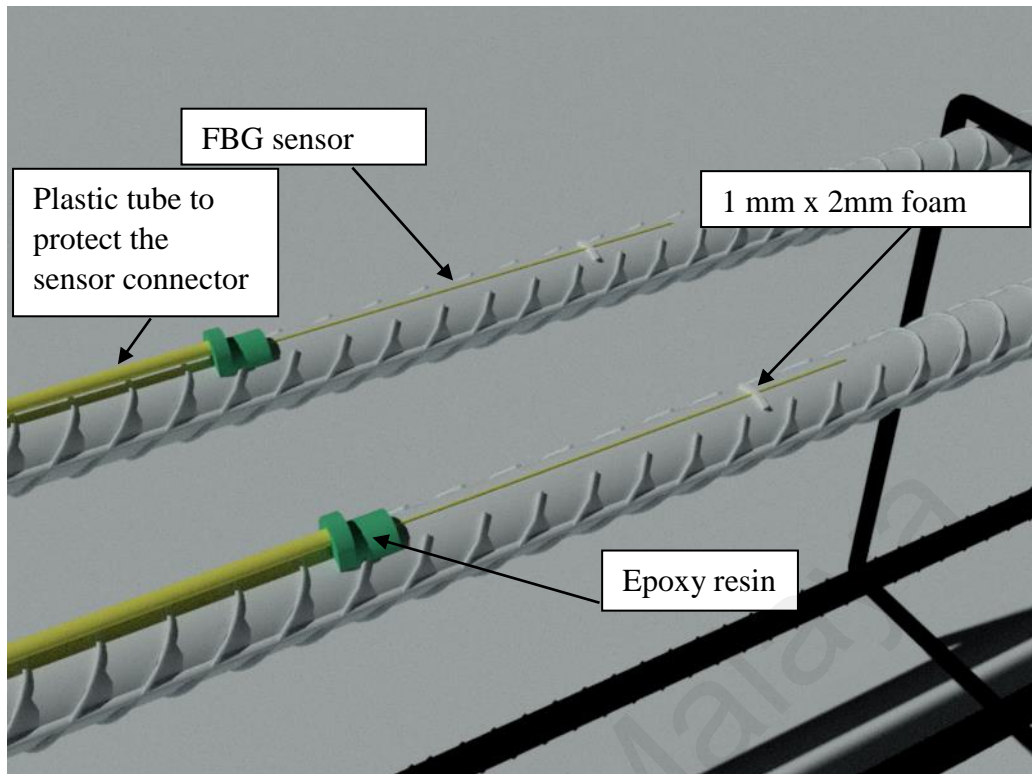


Figure 3.8: Procedure used for mounting FBG strain sensor on steel reinforcement bar for Phase 2. Fiber sensors were placed and fixed on the grinded surface of steel reinforcement.

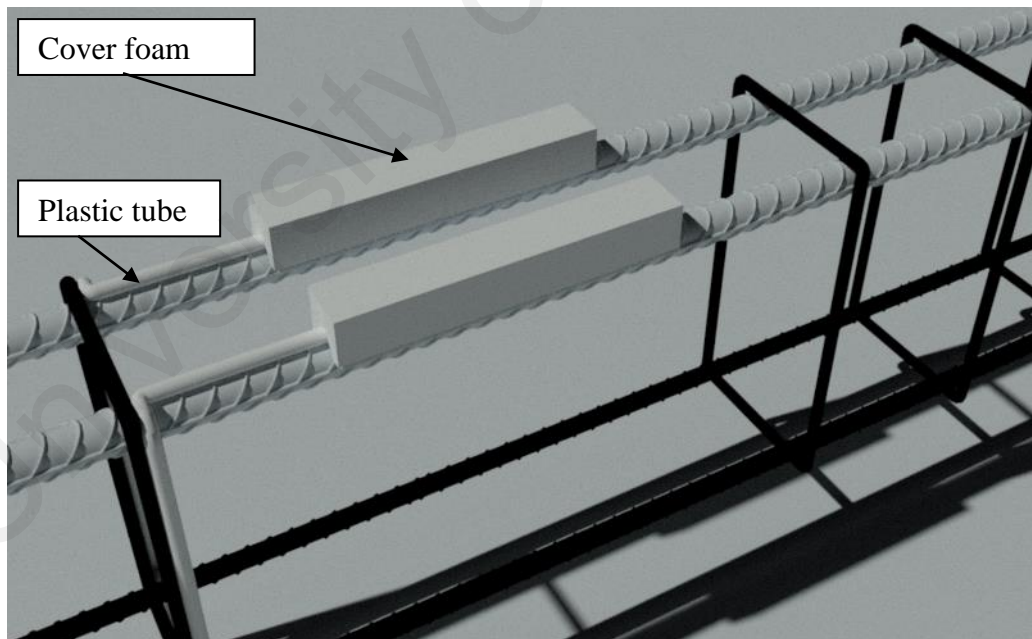


Figure 3.9: Procedure used for mounting FBG strain sensor on steel reinforcement bar for Phase 2. Polystyrene foam was placed to cover FBG strain sensor.

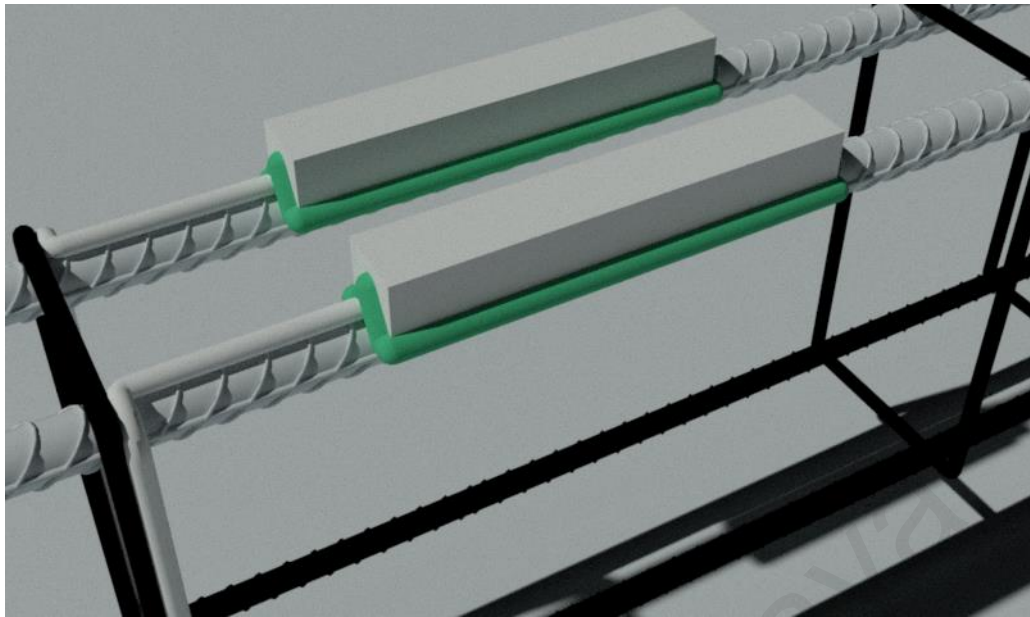


Figure 3.10: Procedure used for mounting FBG strain sensor on steel reinforcement bar for Phase 2. Epoxy resin was applied to perimeter of polystyrene foam to seal gap with steel reinforcement.

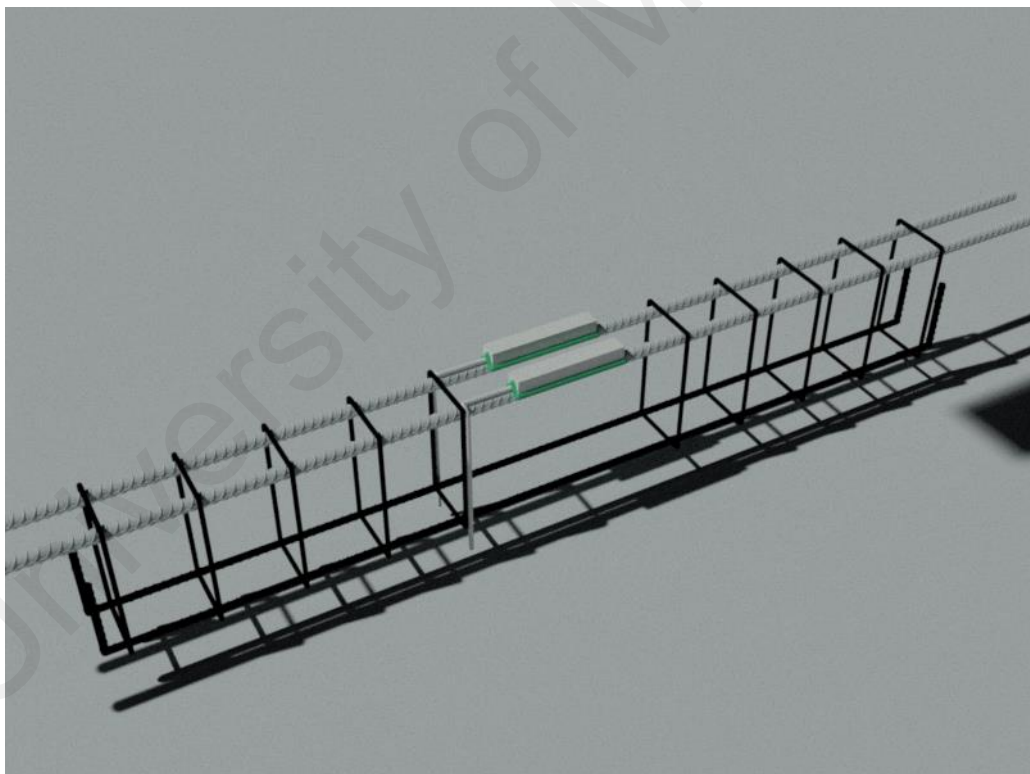
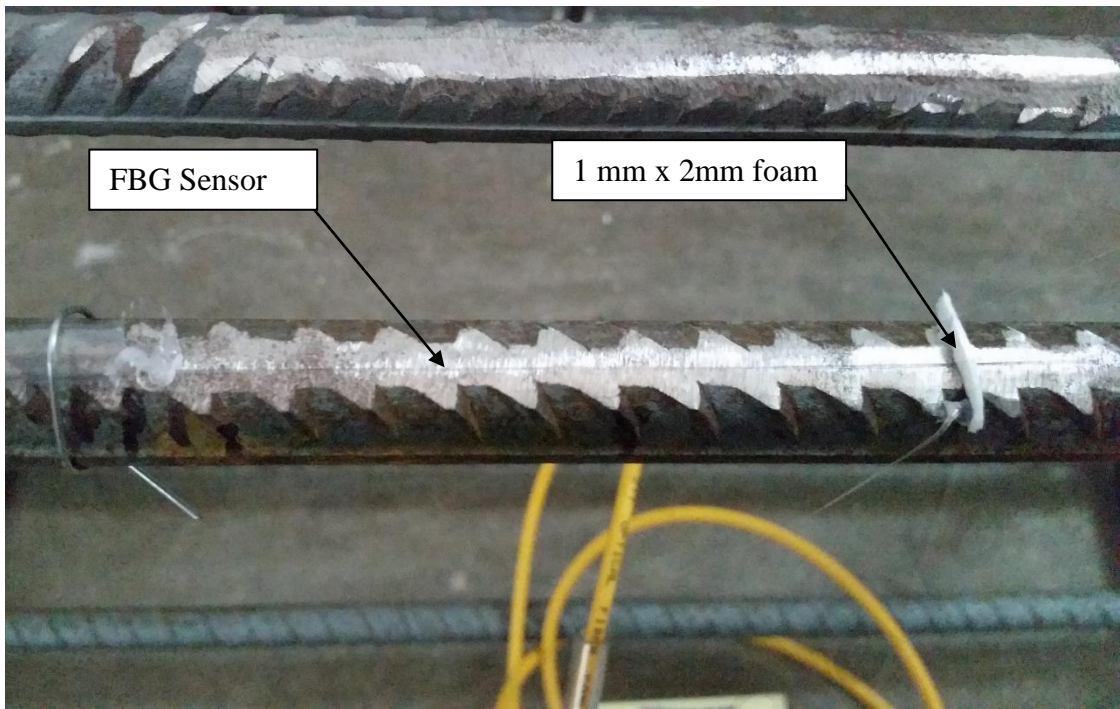
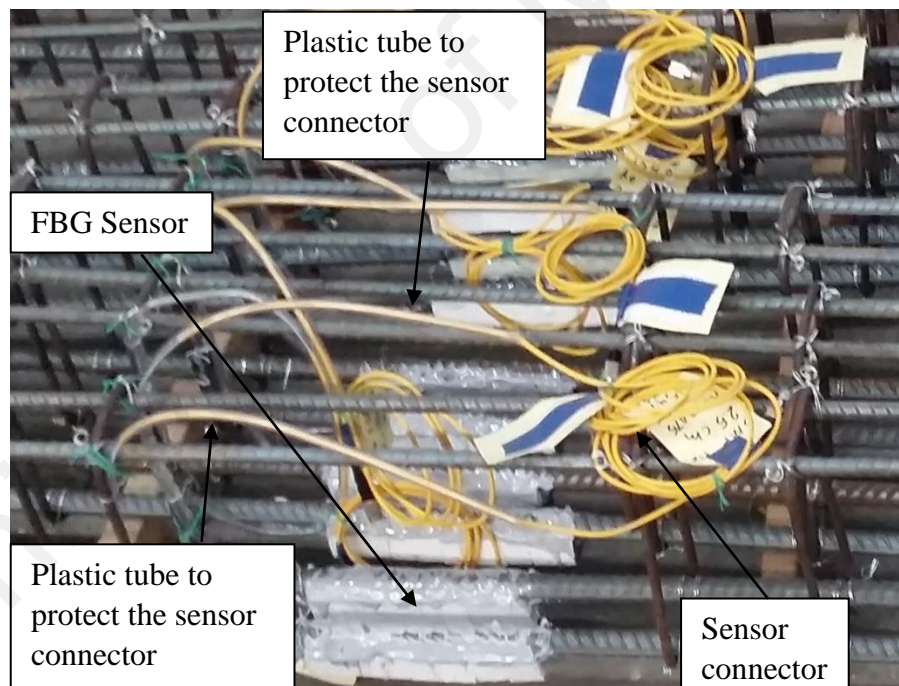


Figure 3.11: Procedure used for mounting FBG strain sensor on steel reinforcement bar for Phase 2. Steel reinforcement cage before concrete pouring.



(a)



(b)

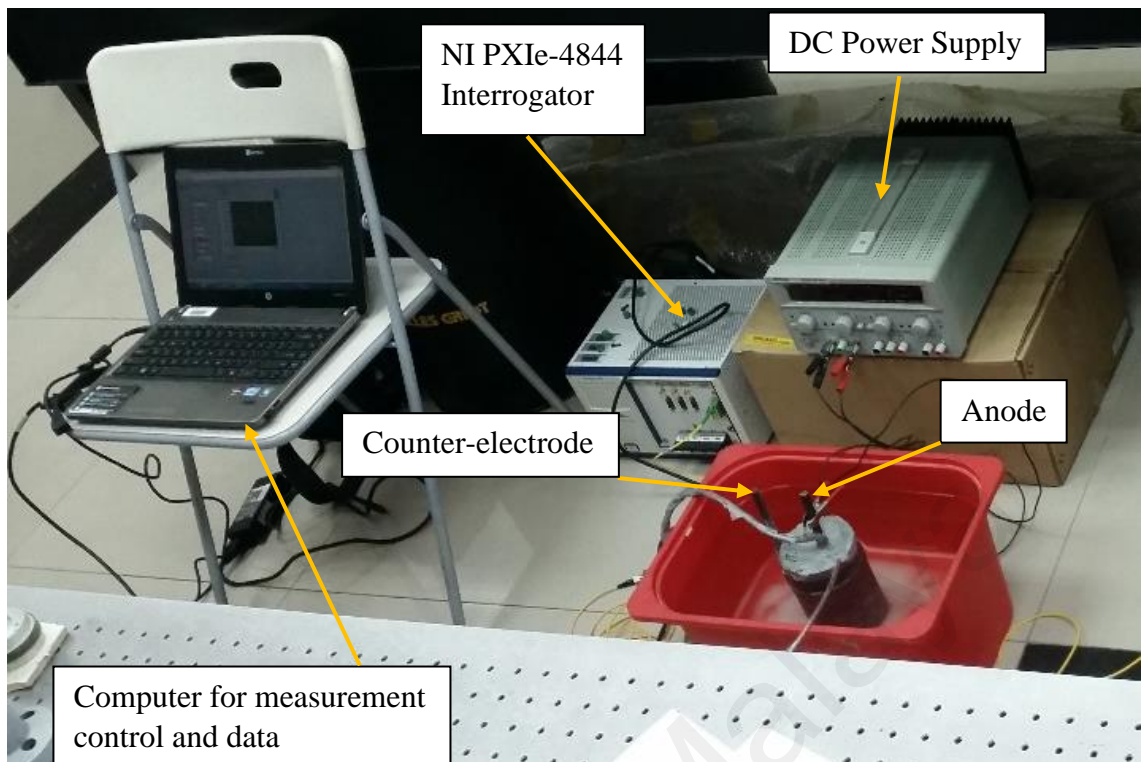
Figure 3.12: Photos of the sensors that were mounted over the steel bar (a) before placing the polystyrene foam (b) after sealing the perimeter of polystyrene foam with steel reinforcement.

3.4. Corrosion and Displacement Experiments Setup

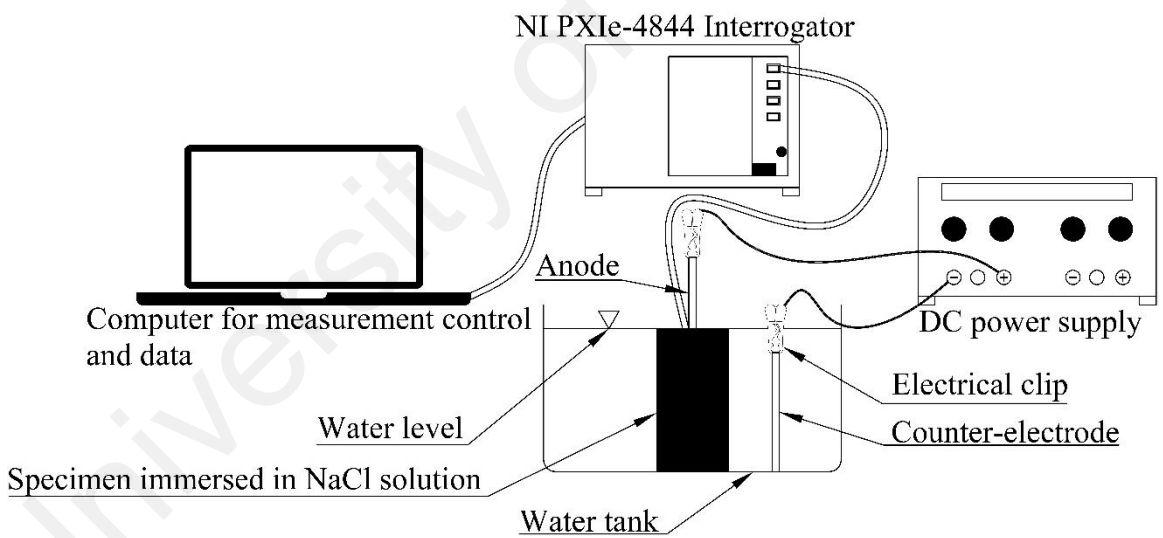
This section describes the setup of both Phases' experiments. Phase 1 includes corrosion experiment, while Phase 2 includes corrosion and flexure experiments.

3.4.1. Phase 1 Experiment

The experimental measurement setup for Phase 1 experiment is shown in Figure 3.13. In each of the two tests in this phase, one specimen was placed vertically into a plastic container filled with 5% NaCl solution by mass. The water level was adjusted to have a height of 20 cm from the specimen base. Also, the top and bottom faces of the second specimen were coated with epoxy resin to prevent steel reinforcement from directly be in contact with NaCl solution during accelerated corrosion process. This considered as an attempt to mimic the actual exposure condition of a typical RC element to corrosion, in which moisture and chloride ions are penetrating from concrete cover and in a direction perpendicular to steel reinforcement. A portable DC Power Supply (MEGURO MP 303-3) was used to perform accelerated corrosion by impressed current technique (Caré & Raharinaivo, 2007). The embedded FBG strain sensor in the concrete specimen was connected to an optical sensor interrogator (National Instrument PXIe-4844). Monitoring and data acquisition were controlled using LabVIEW software (National Instrument). The measurement was configured to have data recorded at one-hour intervals. The accelerated corrosion process was conducted for 36 and 144 hours for the first and second specimens, respectively.



(a)



(b)

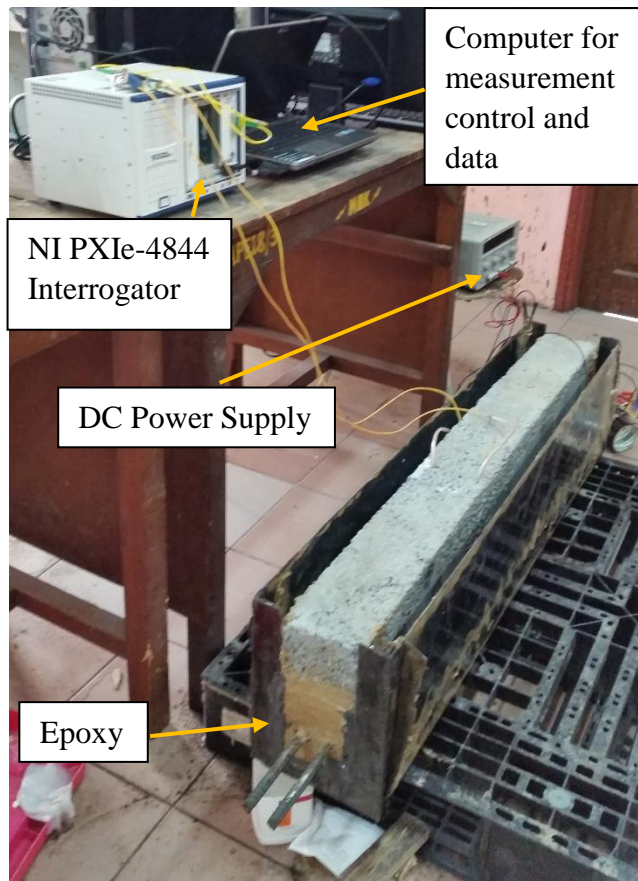
Figure 3.13: Phase 1 experiment: accelerated corrosion setup (a) photo (b) schematic set up.

3.4.2. Phase 2 Experiment

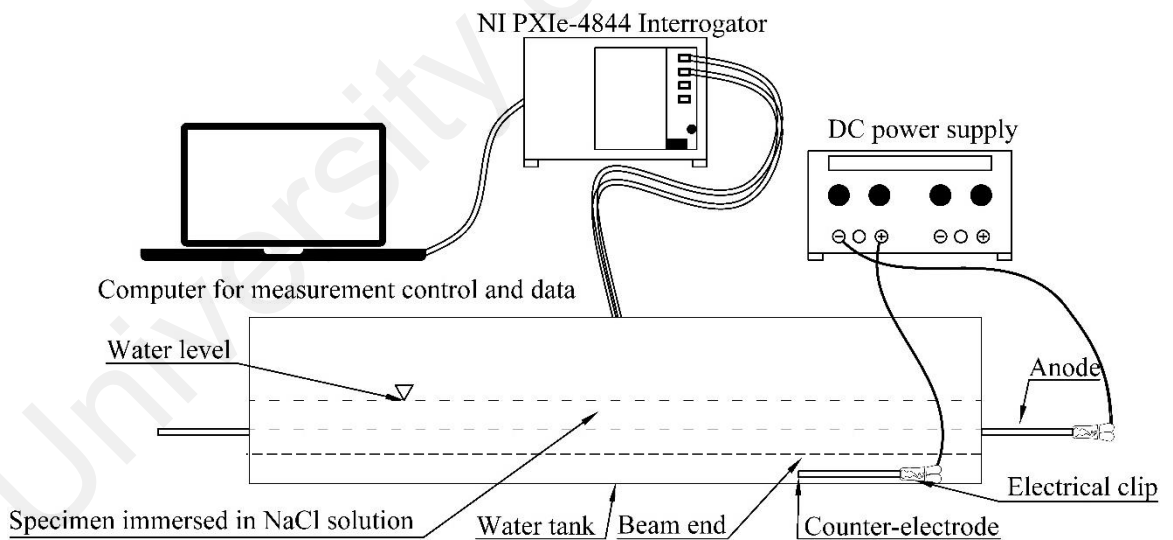
In the Phase 2 experiment, the accelerated corrosion process was performed using the same technique, i.e. impressed current technique. An attempt to mimic the actual exposure condition of a typical RC beam to corrosion, a tank was proposed as shown in Figure 3.14. The tank allows moisture and chloride ions to penetrate concrete cover in a direction perpendicular to steel reinforcement. The beam was laid flat inside the tank, with the extended steel reinforcement ends connected to the DC power supply via cables as shown in Figure 3.15. The exposed end beams were coated with epoxy to prevent any leakage from the concrete.



Figure 3.14: Steel container used for accelerated corrosion of beam specimens.



(a)



(b)

Figure 3.15: Phase 2 experiment: accelerated corrosion setup (a) photo (b) schematic set up.

Four beams corroded at different corrosion levels (2%, 4%, 6% and 10%) that was calculated based on Faraday's law. Notably, each beam has two FBG strain sensors bonded to the two tensile steel reinforcements, respectively. The electrical current was

constant at 2 Ampere throughout the test period. Based on Faraday's formula given by Equation 3.1, each day the steel reinforcement would lose 1% of its weight based on equation 3.2. That being said, accelerated corrosion periods of 48, 96, 144 and 240 hours were applied to BM2, BM3, BM4 and BM5, respectively. As mentioned earlier the tensile steel reinforcements were not anchored in order to be exposed for connecting to the DC power supply.

At the end of the accelerated corrosion experiment of the beams, flexure test was performed in three-point bending by using an Instron Universal Testing Machine in a heavy structural laboratory. Experiments were carried out using load control. The rate of the actuator was set to 5 kN/min. The test was undertaken to check the feasibility of the FBG instrumentation method in evaluating vertical displacement of beam specimens. An LVDT was installed to measure mid-span deflection of the specimens, the data of which would be used to correlate with the measured FBG data. The beam span was 1100 mm. With reference to Figure 3.16, monotonic load was applied to the specimen mid-span. The LVDT and FBG measurements were configured to have data recorded at one-minute intervals.

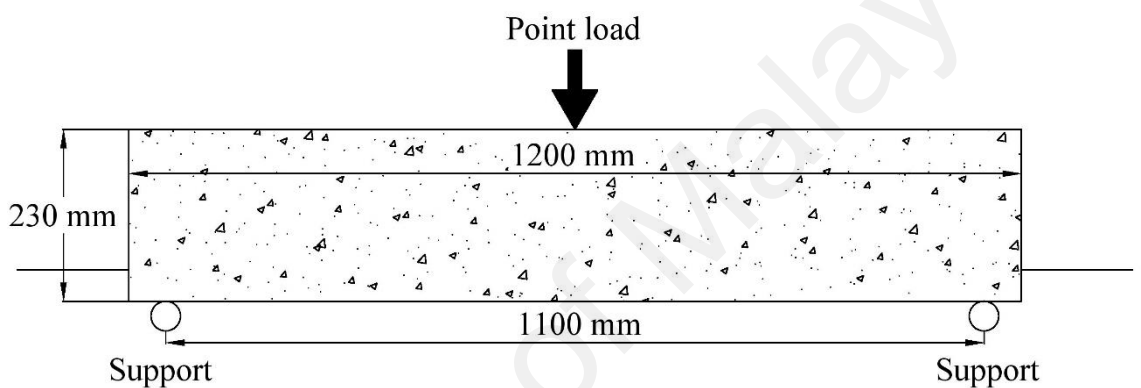
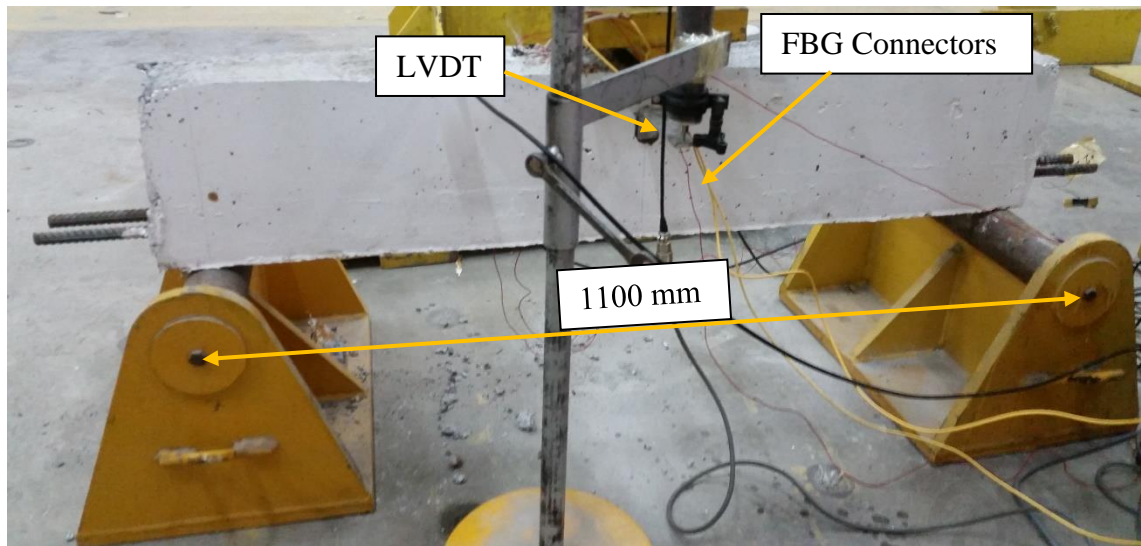


Figure 3.16: Phase 2 experiment: flexure test performed in three-point bending for beam specimens.

3.5. FBG Data Collection

The wavelength shifts of FBG strain sensors were monitored and measured by using an FBG interrogator (National Instrument PXIe-4844). The interrogator was connected by FBG strain sensors with optical fiber extensions. Then the interrogator was connected to a laptop that controlled data acquisition and storage. Measurement of FBG wavelength shift throughout the accelerated corrosion period and the mechanical load test were conducted by the computer using dedicated software programs, namely NI-OSI Explorer Figure 3.17 and LabVIEW Figure 3.18. By setting the wavelength boundaries (nm), the threshold (dBm) around the original peak and finally the minimum width (nm), the NI-OSI explorer can detect the original reflected peak as shown in Figure 3.17, however the explorer could not be used to save the changes of wavelength shift. Therefore, LabVIEW

was used to monitor and save wavelength shifts of the detected original reflected peak by NI-OSI explorer. It is to be noted, any changes in the FBG reflected spectrum shape (RSS) cannot be detected with LabVIEW; the program must be terminated before launching the NI-OSI explorer. LabView could save the wavelength shifts (Amplitude) over time (second). Each FBG sensor wavelength indicated in different colour as shown in LabVIEW front panel (see Figure 3.18).

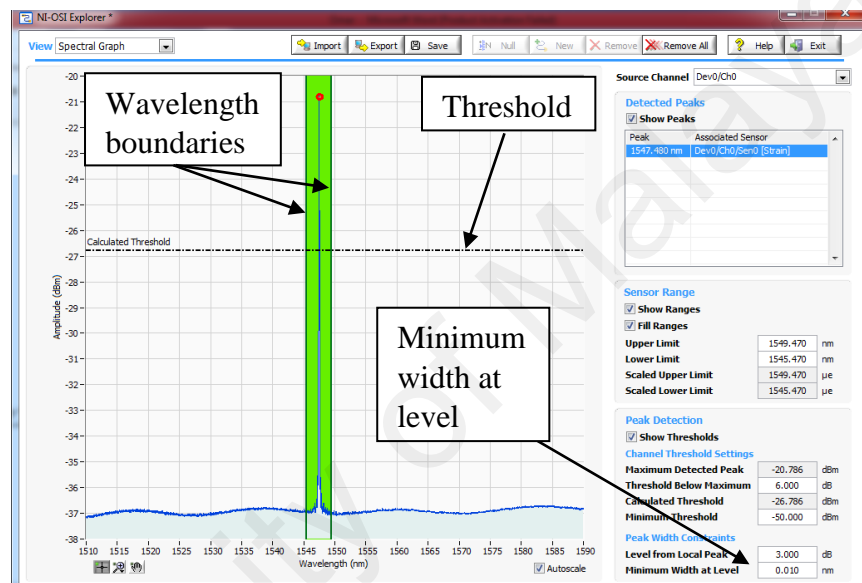


Figure 3.17: NI-OSI explorer main menu.

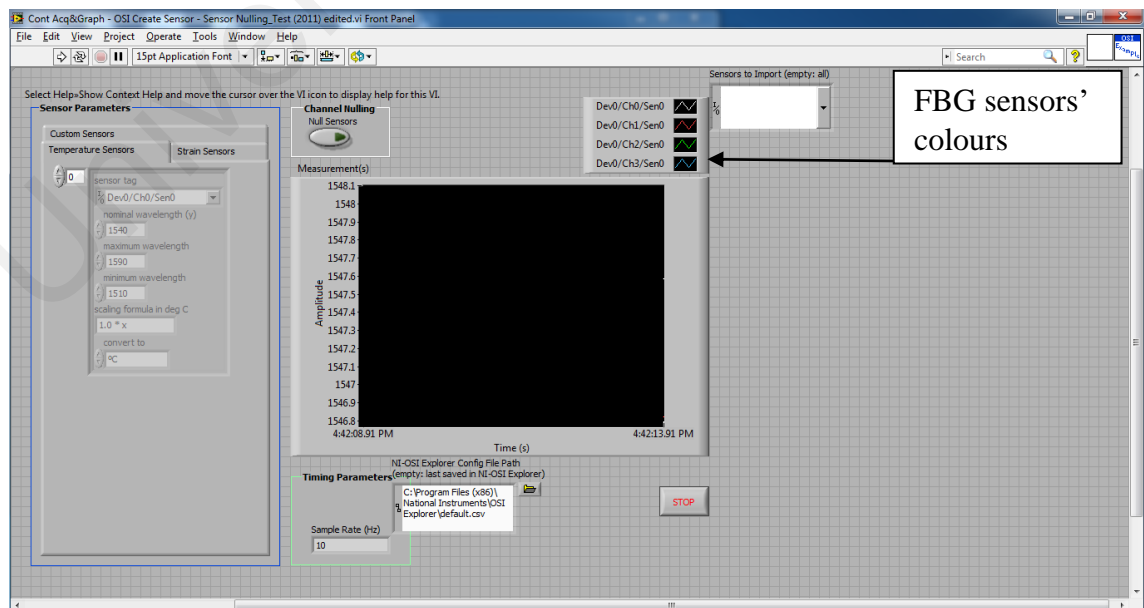


Figure 3.18: LabVIEW front panel.

CHAPTER 4: RESULTS AND DISCUSSIONS

This chapter presents and discusses the results of the Phase 1, Phase 2 experiments and the statistical analysis controlling model used in this study. The chapter includes six sections, corrosion experiments for Phase 1 and Phase 2, concrete mechanical properties, data collection, Phase 2 flexure test, identification of FBG parameters and Shewhart control chart for statistical analysis controlling model.

4.1. Accelerated Corrosion Test

4.1.1. Phase 1 Experiment

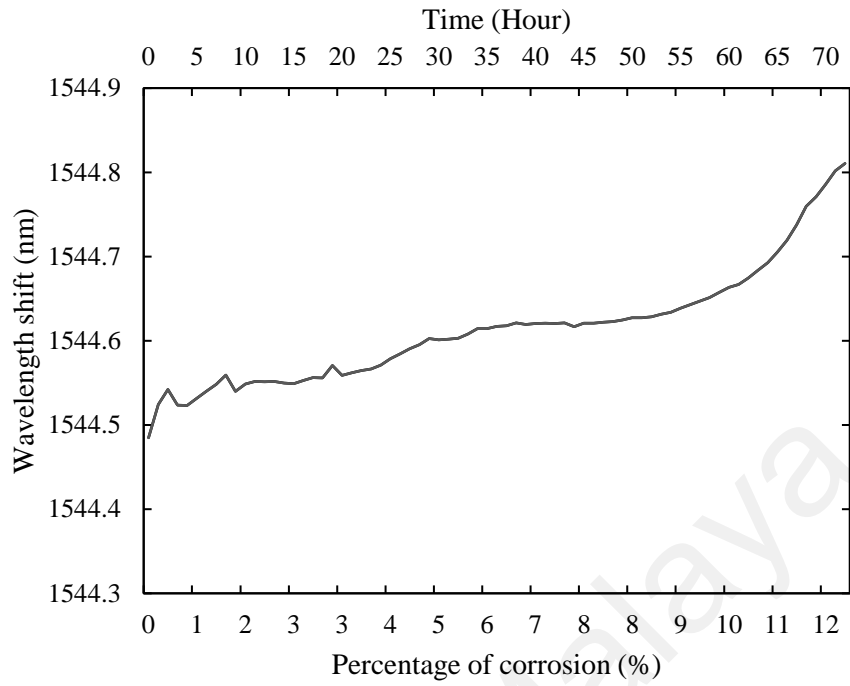
This section discusses feasibility of FBG sensing to monitor corrosion and evaluates effectiveness of sensor protection method adopted in the Phase 1 experiment. Due to safety reasons, the electric current voltage was stable and only fluctuated slightly throughout the corrosion test, giving a maximum variation of 30 V. To prevent current voltage from exceeding 30 V, current values were changed (see Table 4.1). Those changes can be observed especially for specimen 2 due to the duration of the test.

Table 4.1: Current values for each specimen.

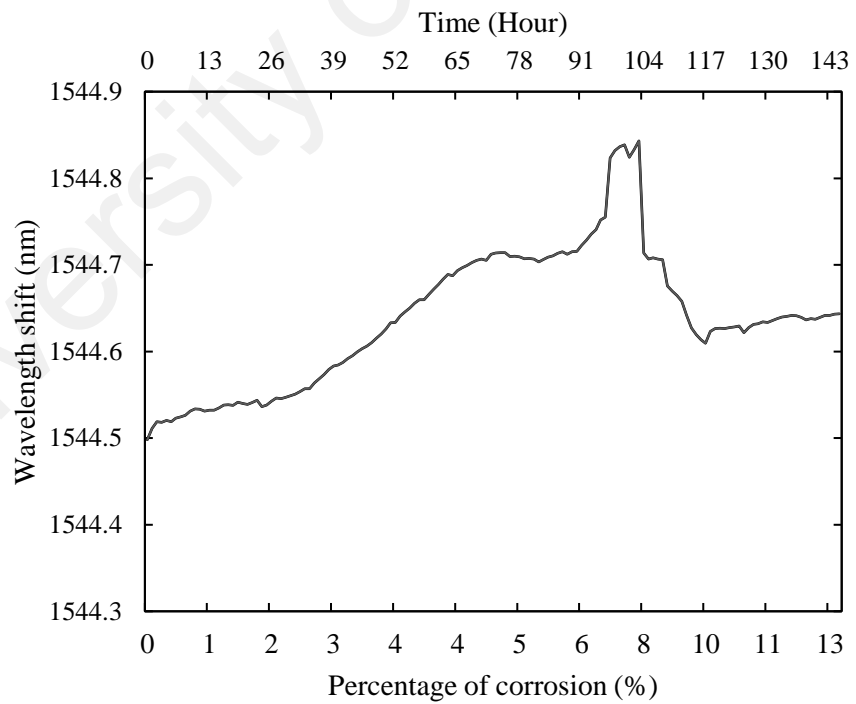
Duration (Hour)	Specimen number	Electric current (Ampere)
0 to 72	1	0.25
0 to 96	2	0.1
96 to 120	2	0.25
120 to 144	2	0.15

A shift in wavelength of FBG strain sensor showed an increment that was correlated with increase of corrosion time as shown in Figure 4.1. As provided by time history plots in Figure 4.1, corrosion introduced stresses that caused gradual changes in

FBG wavelength over time. Figure 4.1a and Figure 4.1b relate the changes in FBG wavelength with time and level of corrosion based on Faraday's law; these changes are expressed in terms of steel mass loss by percentage by using Equations 3.1 and 3.2 for specimen 1 and specimen 2, respectively. After corroding Specimen 2 for 96 hours, a 67-hour break was held before resumption of the impressed current procedure. It was later found out that during the break, progress in wavelength shift has drastically slowed down, and the difference between the first recorded wavelength at the start of the break (1544.762 nm) and the last one (1544.748 nm) at the end of the break was 0.014 nm, which is markedly smaller than other recorded wavelength shifts illustrated in Table 4.2. It is to be noted that the fifth column in Table 4.2 shows corrosion increment, which refers to the corrosion percentage of current hour minus corrosion percent of the previous hour ($6.291\% - 6.223\% = 0.068\%$). This shift was due to the natural rate of corrosion (normal corrosion) that took place during the break without impressed current being induced. In addition, laboratory temperature was kept constant throughout the testing period. Thereby, influence of temperature change on wavelength shift can be disregarded. The measured wavelength shift was solely caused by progression of steel corrosion.



(a)



(b)

Figure 4.1: Wavelength shift of cylindrical specimens 1 (a) and 2 (b) versus time and percentage of corrosion.

Table 4.2: FBG wavelength shift data for specimen 2 from 91 to 107 hours of corrosion time.

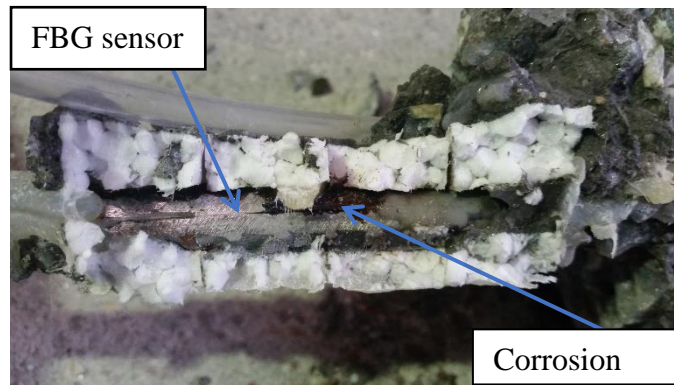
FBG Wavelength (End of the fourth day) (nm)	FBG Wavelength (Beginning of fifth day) (nm)	Corrosion time (Hour)	Corrosion percent (mass lost over original mass) (%)	Corrosion (Increment) (%)
1544.72		91	6.156	0.068
1544.72		92	6.223	0.068
1544.73		93	6.291	0.068
1544.74		94	6.359	0.068
1544.75		95	6.426	0.068
1544.76		96	6.494	0.068
67-hour break				
	1544.82	97	6.562	0.068
	1544.83	98	6.629	0.068
	1544.83	99	6.697	0.068
	1544.83	100	6.866	0.169
	1544.82	101	7.035	0.169
	1544.83	102	7.204	0.169
	1544.84	103	7.373	0.169
	1544.71	104	7.543	0.169
	1544.70	105	7.712	0.169
	1544.70	106	7.881	0.169
	1544.70	107	8.050	0.169

After completing Phase 1 accelerated corrosion the specimens were hacked open to examine the conditions of steel bars and FBG strain sensors. Figure 4.2 shows the conditions of corroded steel bar and FBG strain sensors observed at the interior of Specimens 1 and 2. Figure 4.2a shows that responses attained from the sensor were closely related to the increased volume of the corrosion product layer. According to García et al. (2006), this layer could be potentially formed from two types of corrosion

products, namely, adherent and non-adherent products. The adherent layer is deposited over bar surface while non-adherent layer is loosely bound to metal surface and probably dissolved in solution during corrosion. Therefore, at high corrosion levels, in the presence of a solution, non-adherent corrosion products act as fluids, as observed from Specimen 2 given in Figure 4.2b. This finding suggested that at high corrosion levels, no significant stresses were induced to the FBG strain sensor. This was supported by FBG wavelength shift measurement data, which was found to be almost constant for Specimen 2 at 97 hours to 103 hours after the start of corrosion experiment (see Figure 4.1b). Additionally, after 103 hours of corrosion of Specimen 2, FBG wavelength shift was found to have decreased, signifying movement of corrosion products; these movement were due to cracks propagated within the specimen, as shown in Figure 4.3. Notably, a marked jump in wavelength shift was noted between 96 hours to 97 hours after initiation of corrosion experiment. This jump corresponded to increase in electrical current; such increment kept current voltage constant throughout the experiments (Table 4.1 and Table 4.2).

Changes in current (A) affected the corrosion uniformity of steel bars of both specimens. Initial steel reinforcement corrosion of the second specimen was more uniform because of low ampere values. By contrast, the first specimen started with a high ampere value, leading to less uniform corrosion. This condition resulted in steel reinforcement of Specimen 1, which was mostly corroded on the base and not on the area of FBG; such phenomenon determines the difference between corrosion conditions of each specimen (see Figure 4.2). Remarkably, Specimen 2 was more severely corroded than Specimen 1 on the location of FBG sensor. Additionally, upon detailed examination, FBG sensors in both specimens were found intact, and their bonds with steel reinforcement remained sound. Thus, the sensors were in good working condition and can be recycled for other uses by detaching them from steel bars by heating the bonding

epoxy resin. This finding bears significance in validating the feasibility of mounting procedure for FBG strain sensor developed for monitoring and evaluating steel reinforcement corrosion embedded in concretes. In other words, the FBG sensing method adopted in this study for monitoring corrosion was considered successful in ensuring robustness and sensitivity of the FBG strain sensor to detect steel corrosion during extended period of accelerated corrosion.



(a)



(b)

Figure 4.2 : Condition of specimen 1 and 2 reinforcements and their FBG strain sensors after corrosion experiment. (a) Specimen 1 (b) Specimen 2.

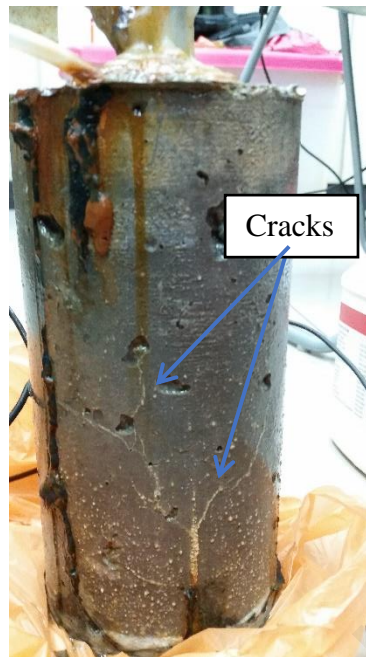


Figure 4.3: Specimen 2 shows the crack after the corrosion process.

4.1.2. Phase 2 Experiment

The Phase 2 experiment used beam specimens subject to accelerated corrosion test that followed the same procedure as with Phase 1. The theoretical and actual corrosion levels of the beam specimens, expressed in terms of percentage of mass difference of tensile steel reinforcements evaluated before and after corrosion, are given in Table 4.3. Discrepancies between the theoretical and actual corrosion levels could be attributed to two factors. The first factor involves the accuracy of Faraday's law; Fang et al. (2004) showed that the severity of corrosion evaluated based on the Faraday's law was generally higher than the actual one. The same conclusion was drawn from the results of this study, as shown in Table 4.3. The reason behind that is the valency of the corrosion reactions (equation 2.1 and 2.2) (Pantazopoulou & Papoulia, 2001). The valency usually is empirically assumed between 2 and 3 (2 for $\text{Fe}(\text{OH})_2$, and 3 for $\text{Fe}(\text{OH})_3$), which effect the accuracy of the Faraday' low (Chen & Mahadevan, 2008). The second factor refers to potential corrosion that occurred to the shear links in the beam specimens because they were in contact with the tensile reinforcements, resulting in lesser-than-expected

reactions directed to corrode the tensile reinforcements. This connection led the shear links to corrode simultaneously with tensile steel reinforcements.

Table 4.3: Comparison between theoretical and measured corrosion level for beams' specimens by weight.

Beam No.	Steel reinforcement no.	Mass of steel reinforcement		Corrosion level	
		before corrosion test (g)	after corrosion test (g)	Designed corrosion (%)	Measured corrosion (%)
1	1	2254	2250	0	0.1
	2	2270	2266	0	0.1
2	1	2272	2244	2	1.2
	2	2274	2244	2	1.3
3	1	2270	2206	4	2.8
	2	2244	2184	4	2.7
4	1	2252	2134	6	5.24
	2	2266	2148	6	5.21
5	1	2256	2084	10	7.62
	2	2262	2048	10	9.46

Each beams' tensile steel reinforcements (BM2, BM 3 and BM4) presented almost the same actual corrosion level, except for BM5. This was indicated by the actual corrosion level (Table 4.3) and theoretical wavelength shift based on the regression lines as shown in Figure 4.9, which is indicated with black colour lines for BM5. The discrepancy was attributed to the way the steel reinforcements were connected for accelerated corrosion test. As discussed in Section 3.2.3, steel reinforcements were

connected to a power supply to enforce electrolysis process that generated corrosion. Therefore, by connecting the negative terminal to a bare steel bar immersed in the solution and connecting the positive terminal to both embedded steel reinforcements, an electrical circuit was formed through the solution. Electrical current was transmitted through steel reinforcements, which featured a lower resistance. In this case, steel reinforcement No. 2 (Table 4.3) showed a lower resistance based on results and wavelength shift. Resistance was due to the concrete cover of steel reinforcement No. 2; at high concrete porosity, resistance is low and vice versa. Figure 4.4 presents the current flow of the electric circuit; the figure clearly shows that current flow strongly depended on the concrete cover around the steel reinforcements.

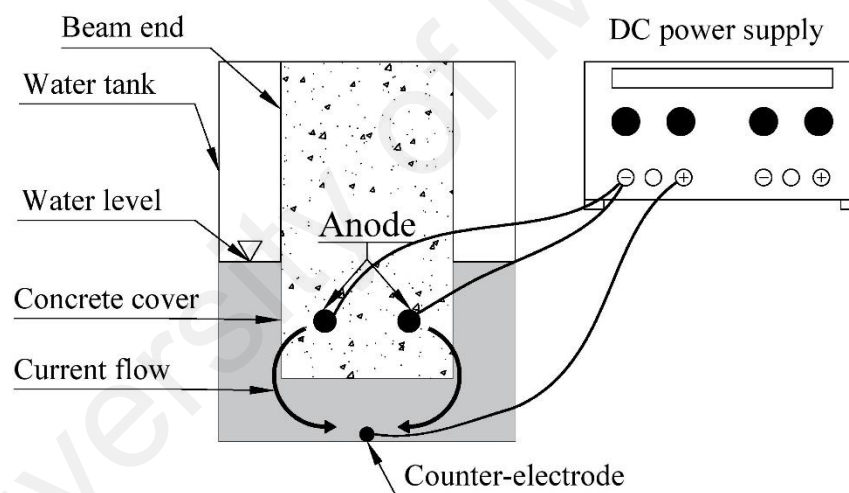
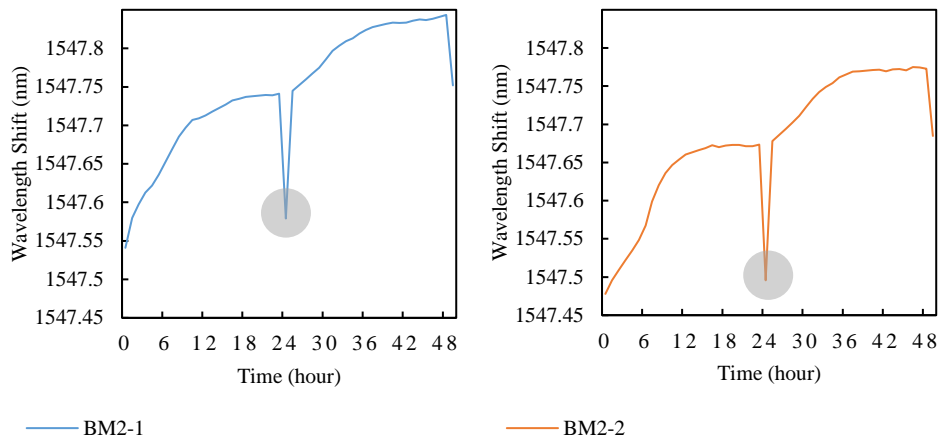


Figure 4.4: Beam cross section of corrosion experiment of Phase 2.

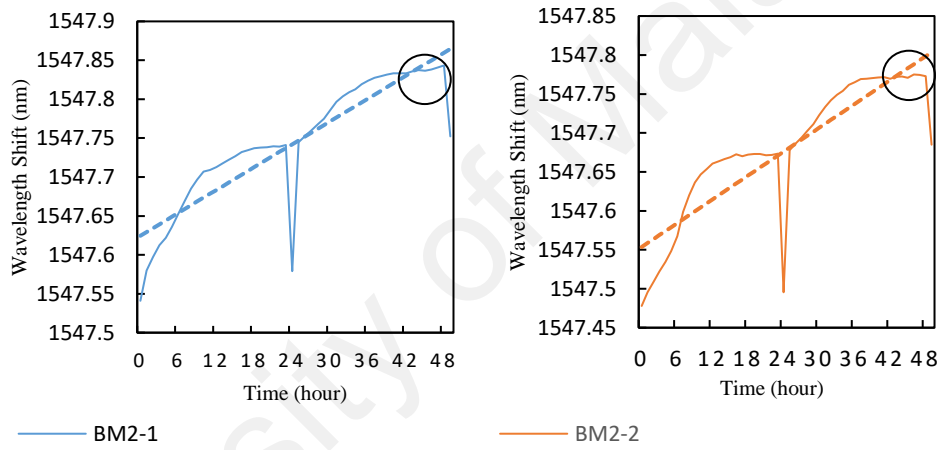
Similar to Phase 1 experiment, a correlation could also be found between the level of corrosion and wavelength shift in FBG strain sensor. Figure 4.5–4.8 show wavelength shift in steel reinforcements of each beam versus time. Figure 4.5a–4.8a show actual wavelength shifts of total time of corrosion, whereas Figure 4.5b–4.8b show wavelength shift from the start of the test until extreme changes in slope measurements were obtained. A regression line was drawn to investigate the relationship between FBG measurements

and corrosion time. For BM2, BM3, and BM4, FBG wavelength shift data curves of the two FBG sensors in each of the beams have very similar slopes, as shown in Figure 4.5 to 4.7, respectively. For BM5 (see Figure 4.8) however, the difference in the wavelength shift data between its two FBG sensors was caused by the discrepancy in corrosion level between its two steel reinforcements. From these observations, it can be confirmed that the FBG sensors responded consistently against corrosion of steel reinforcement. Table 4.4 shows that regression equations of initial measurements of wavelength shifted before they became unstable. Additionally, the regression lines of all beams were plotted to investigate the effects of each beam specimens' corrosion conditions to the relationship between the FBG measurements and corrosion time. The curve fit coefficient (R^2) of the regression lines indicated that the strong regression correlation between the wavelength shift and time of corrosion (corrosion level), where R^2 of the regression lines range from 0.74 to 0.96 of all beam specimens, which indicate a strong relationship between the wavelength shift and time of corrosion (corrosion level) (Lyu et al., 2017). Figure 4.9 displays wavelength shifts versus time; the figure was based on regression equation from FBG measurements of corroded beams (BM2-1 in the figure indicates Beam 2 Sensor 1). Measurements were obtained from the original wavelength shift at the beginning of the test until unreliable measurements were determined because of non-adherent corrosion products. Various factors affected similarities between beam measurements, for example, corrosion was nonuniform on steel surface. FBG strain sensor is considered as a point sensor (Kersey et al., 1997); it can monitor only one point of steel reinforcement. Therefore, the FBG sensing method is considered effective at detecting the generation of corrosion in a steel reinforcement at location where a sensor is placed, or its close surrounding. FBG sensor wavelength increment, which correlated to corrosion level, was inaccurate and unreliable at high levels of corrosion (approximately over 3%) due to the fluctuation of the measured data as shown in Figure 4.5 to Figure 4.8. The fluctuation of

FBG measured data increased dramatically at high levels of corrosion, which is indicated by black circles in Figure 4.5 to Figure 4.8. Therefore, after that level, the sensor was found to be inconsistent in giving readings that could be related to corrosion progress. As a result, the proposed FBG instrumentation method is more effective in wet-dry cycles conditions than under constant humidity, which form adherent corrosion products layer, so-called “patina” that can be detected by the instrumentation method proposed (Krivy, 2017). It is to be noted that there was minor fluctuation before the indicated points by the black circles, those fluctuations are due to detecting unwanted reflected peak as shown in grey circles in Figure 4.5. The discussion of detecting unwanted peak will be in section 4.3.

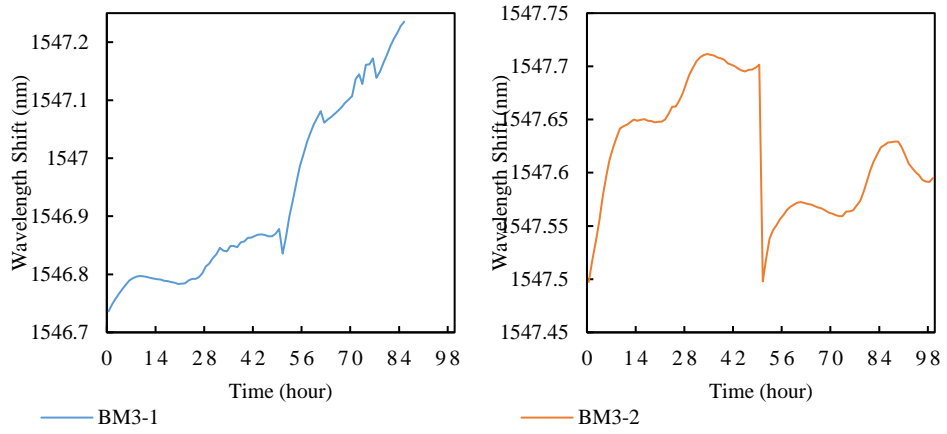


(a)

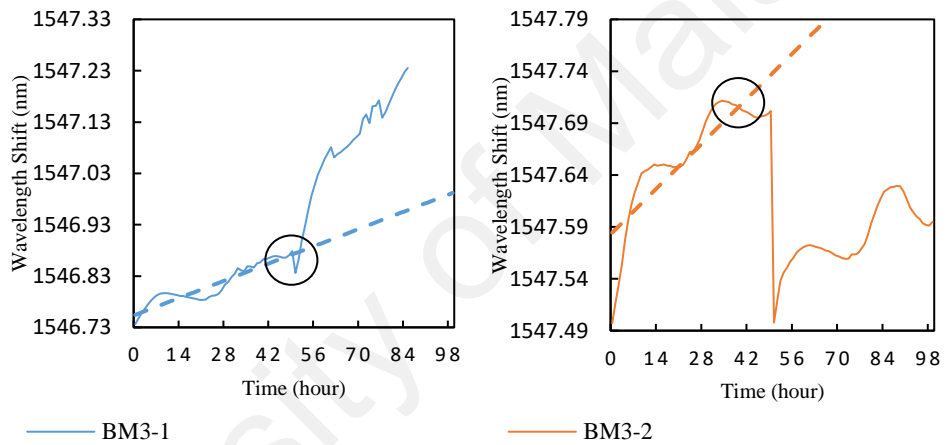


(b)

Figure 4.5: FBG vs corrosion time for BM2 wavelength shifts of FBG sensors (a) actual in total time of corrosion (b) linear regression.

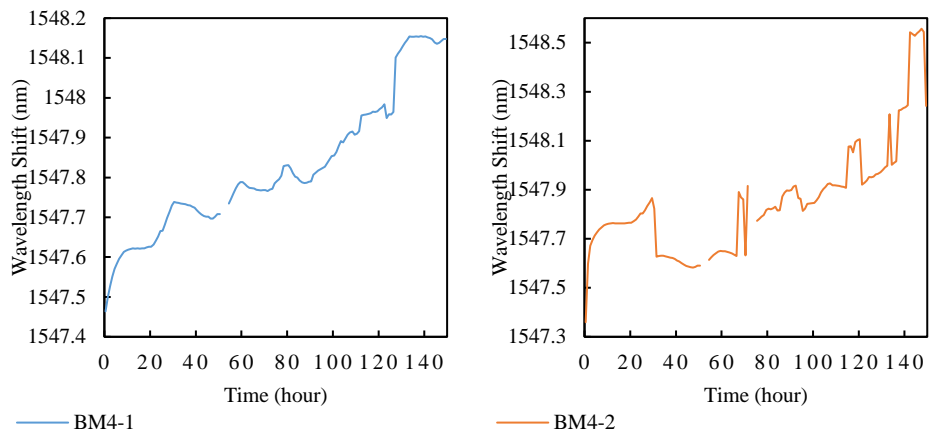


(a)

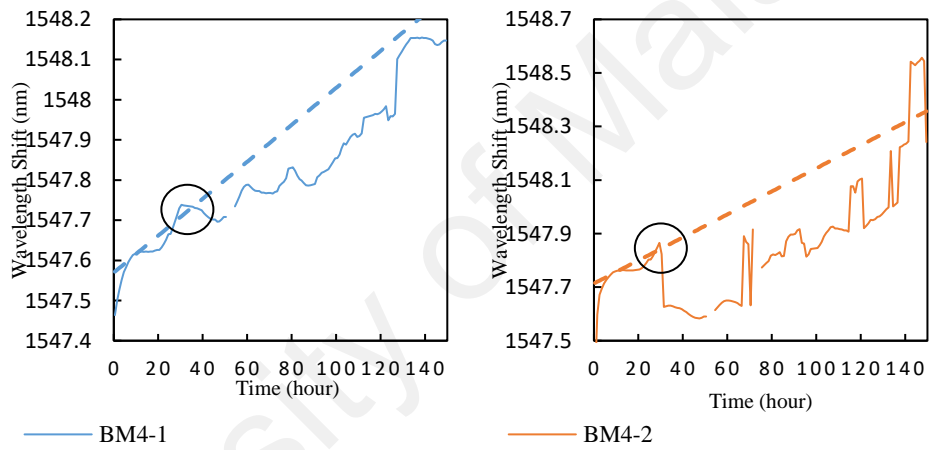


(b)

Figure 4.6: FBG vs corrosion time for BM3 wavelength shifts of FBG sensors (a) actual in total time of corrosion (b) linear regression.

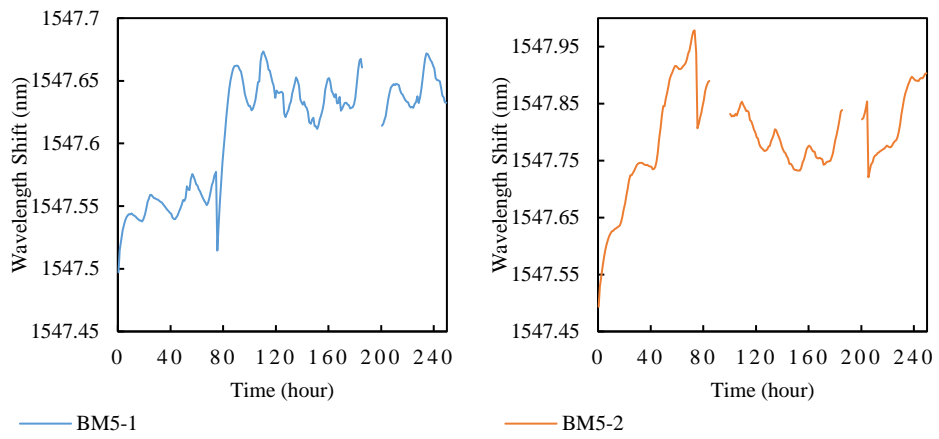


(a)

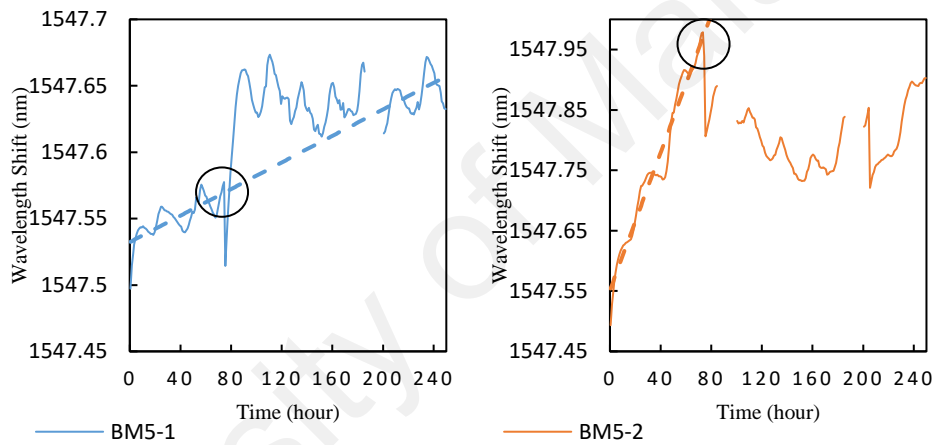


(b)

Figure 4.7: FBG vs corrosion time for BM4 wavelength shifts of FBG sensors (a) actual in total time of corrosion (b) linear regression.



(a)



(b)

Figure 4.8: FBG vs corrosion time for BM5 wavelength shifts of FBG sensors (a) actual in total time of corrosion (b) linear regression.

Table 4.4: Regression equations for wavelength shift of corrosion level measurements.

Beam	Channel	Linear Equation	Curve Fit Coefficient (R ²)
2	1	$y = 0.0052x + 1547.6$	0.8342
	2	$y = 0.0055x + 1547.5$	0.7994
3	1	$y = 0.0024x + 1546.8$	0.8776
	2	$y = 0.0031x + 1547.6$	0.7409
4	1	$y = 0.0046x + 1547.6$	0.836
	2	$y = 0.0043x + 1547.7$	0.8202
5	1	$y = 0.0005x + 1547.5$	0.5494
	2	$y = 0.0057x + 1547.5$	0.9631

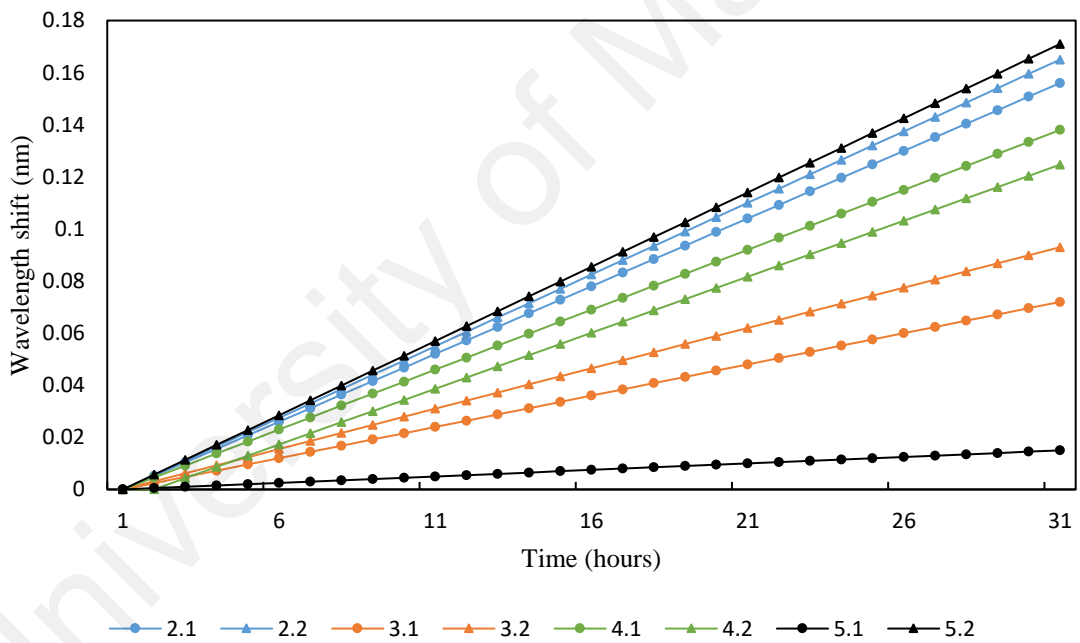


Figure 4.9: Theoretical wavelength shift based on the regression equations.

FBG sensing method can detect two out of the four stages of corrosion (Chen & Mahadevan, 2008). Corrosion stages are illustrated in Figure 4.10. The first stage is associated with chloride penetration and corrosion initiation. In actual corrosion, the first stage lasts for years. In the current study, the first stage was considered the initial two hours after initiation of corrosion. The second stage was defined as the period during

which free expansion of corrosion products, namely rust occurred, which in this current study was deemed to happen from the 101st hour after corrosion process started. In this stage, voids in concrete surrounding steel bars were occupied by rust. The third stage was considered stress initiation, when rust induced stresses on the concrete, thereby resulting in cracking events. In this study, the third stage of steel corrosion was unclearly identified by FBG strain sensing because of the isolation of sensors from concrete material with polystyrene foam cover, however a crack was observed after 101st hour of corrosion process. Additionally, the last stage was unremarkable.

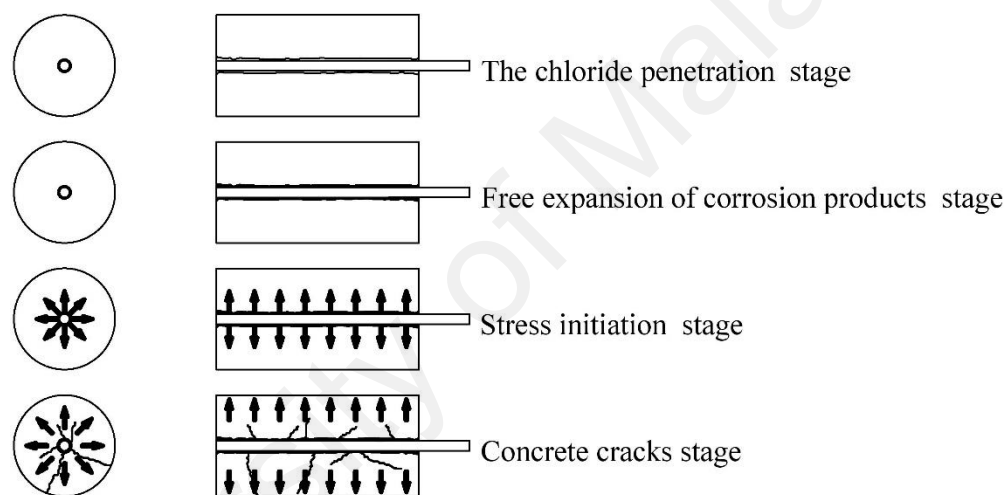


Figure 4.10: Chloride-induced reinforcement corrosion and cracking patterns (Chen & Mahadevan, 2008).

4.2. Concrete Mechanical Properties

The concrete used for beam casting was characterized by British Standards European Norm (BS EN) and American Society for Testing and Materials (ASTM) standard tests. The tests included compression test, splitting tension test and static modulus of elasticity test. The average 28th-day compressive strength was tested in according to BS EN 12390-3: 2009 at 40 MPa. Splitting tensile test in according to BS EN 12390-6: 2009 was performed to check indirect tensile strength of concrete, the test results indicated averages of 4 MPa for 200x100 mm cylindrical specimens and 2.8 MPa for 300x150 mm

cylindrical specimens. The modulus of elasticity of concrete tested at 28 days after casting in according to ASTM C469 / C469M – 14 reached an average of 33000 MPa. The same series of tests were conducted after completing the corrosion tests of all RC beams, which took almost 3 months (85 days). The tensile strength and modulus of elasticity of concrete tested using the same tests gave very similar results compared to that obtained at 28 days after casting. However, the concrete compression strength has increased to 49 MPa. Concrete density was measured at 2330 kg/m³, which is lower than the normal concrete density (2400-2500 kg/m³) because of the intended higher porosity to allow a higher rate of chloride ion penetration into concrete for generating corrosion to steel reinforcement.

4.3. Problems Faced in FBG Data Collection

For detailed discussion of the FBG measured data collection can refer to section 3.5. However, this section focuses on the two problems that affected the FBG data collection, which have been presented in two cases (first case: missing data, second case: detecting non-original peak). The two cases are illustrated in Figure 4.11 and 4.12. In normal data collection, settings of NI-OSI Explorer are fixed during data collection. In this study, however, FBG wavelength shift detection was affected due to certain changes in RSS, thereby creating many unwanted peaks. These changes influenced the efficiency and capability of the interrogator to detect the original reflected peak. FBG data collection was stopped when there are any unnatural patterns, such as missing data or detecting unwanted peak as shown in Figure 4.12. Then, specific adjustments applied to the configurations of NI-OSI to allow LabVIEW to continue detecting the original reflected peak without missing FBG data. Continued observation of the LabVIEW front panel was required to avoid loss or erroneous measurements. Therefore, a statistical analysis model is proposed in section 4.6 to indicate if there are any changes in reflected peak detected. Figure 4.13 to 17 display spectral graphs of sensors of all beams. Spectral graphs were

obtained before and after corrosion test for Phase 2 experiments are shown in top and bottom graphs of Figure 4.13 to 17, respectively. Each beam specimen featured two FBG strain sensors for each tensile steel reinforcement.

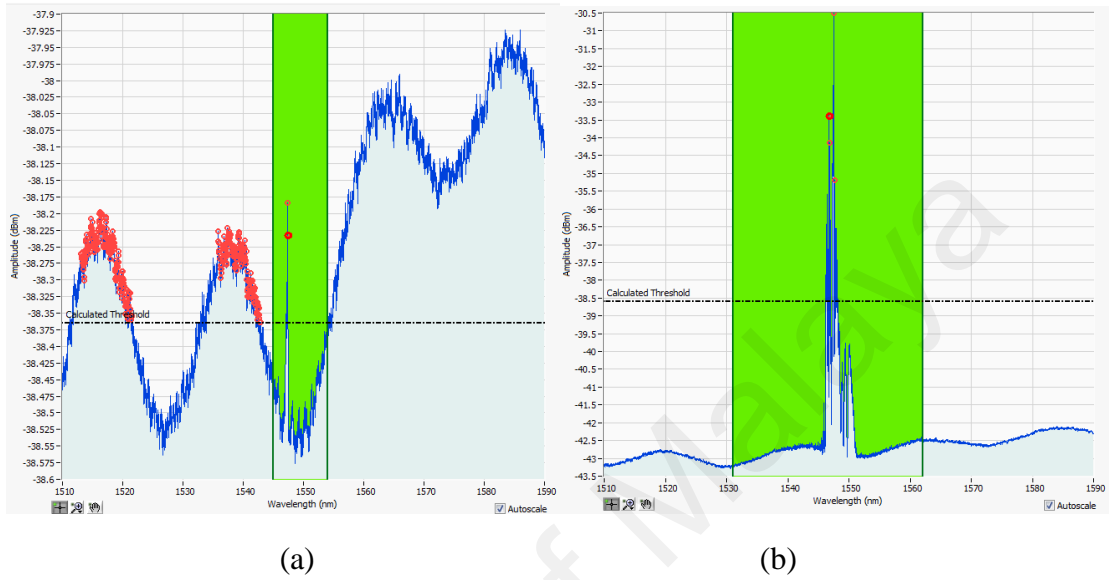
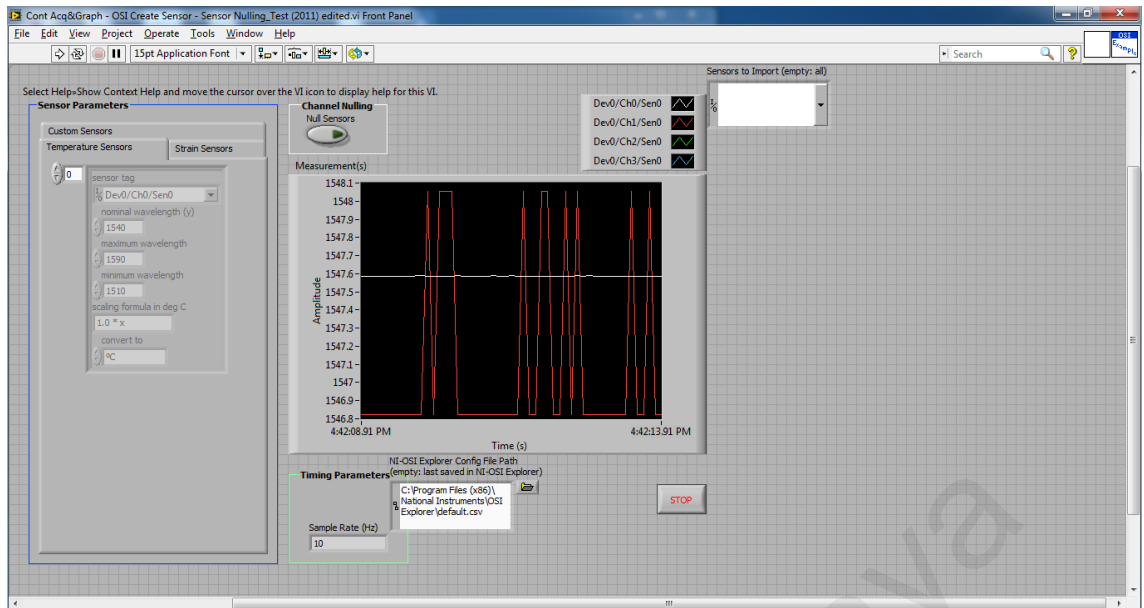
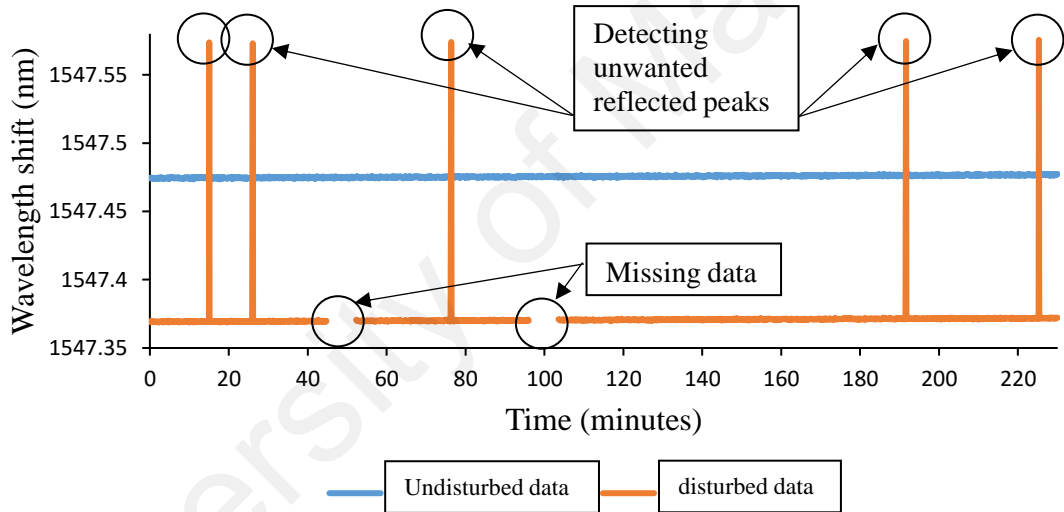


Figure 4.11: NI-OSI Explorer spectral graph view of the multippeak cases (a) missing data (b) detection of unwanted peaks.



(a)



(b)

Figure 4.12: Wavelength shift peaks obtained from (a) real-time monitoring display and (b) time history plot.

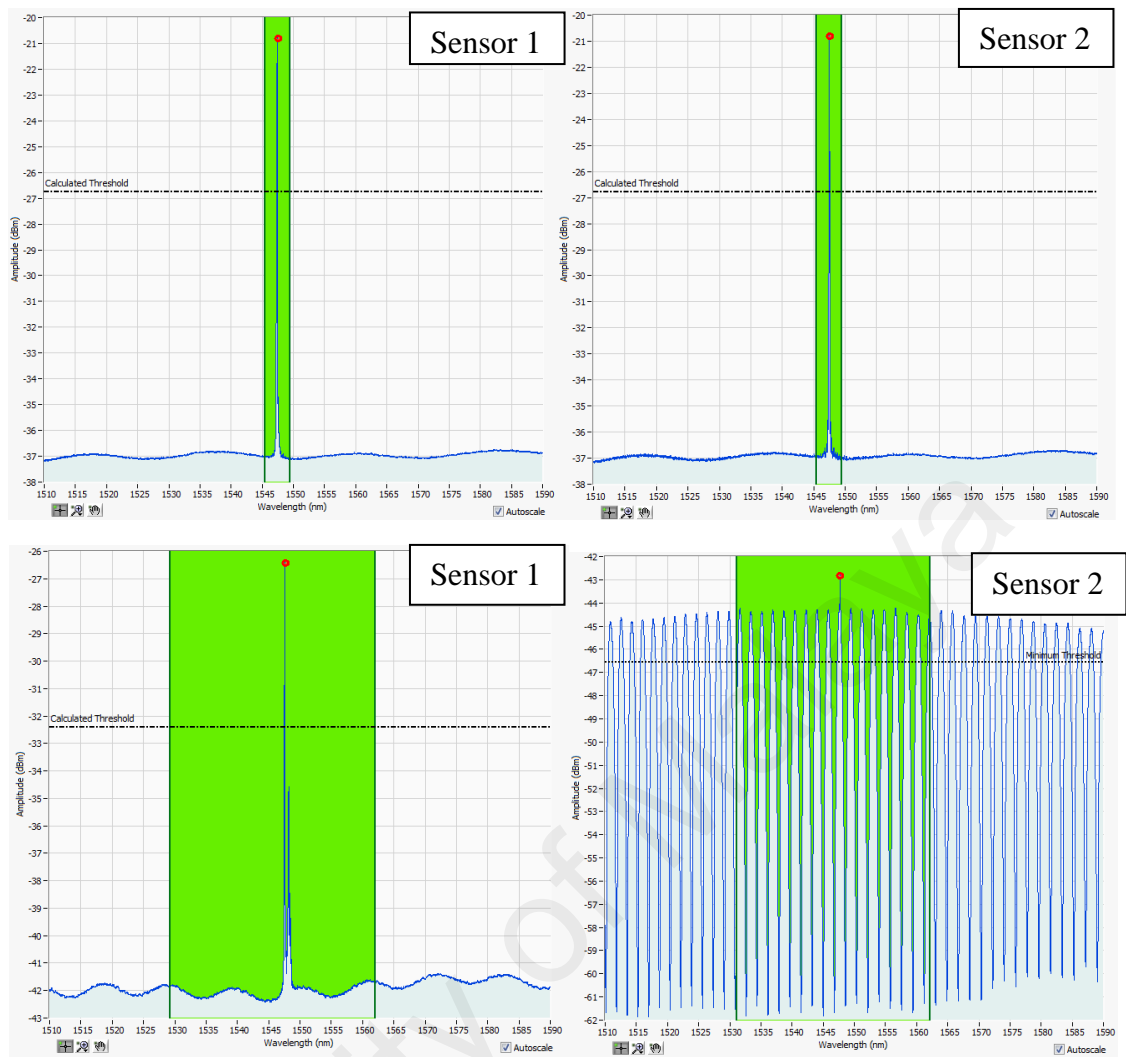


Figure 4.13: Reflected spectrums before and after corrosion experiment obtained from BM5-1 and BM5-2.

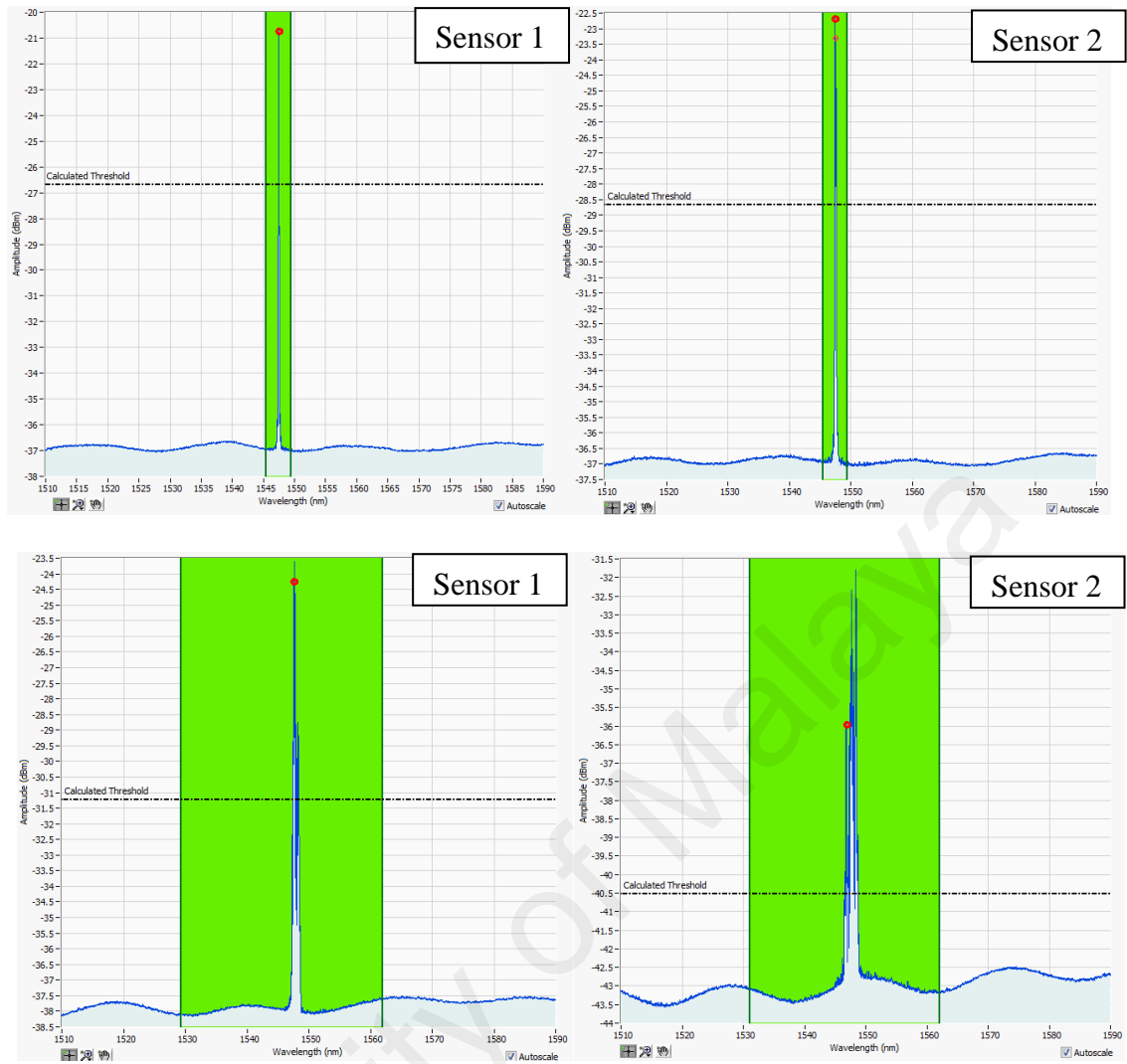


Figure 4.14: Reflected spectrums before and after corrosion experiment obtained from BM4-1 and BM4-2.

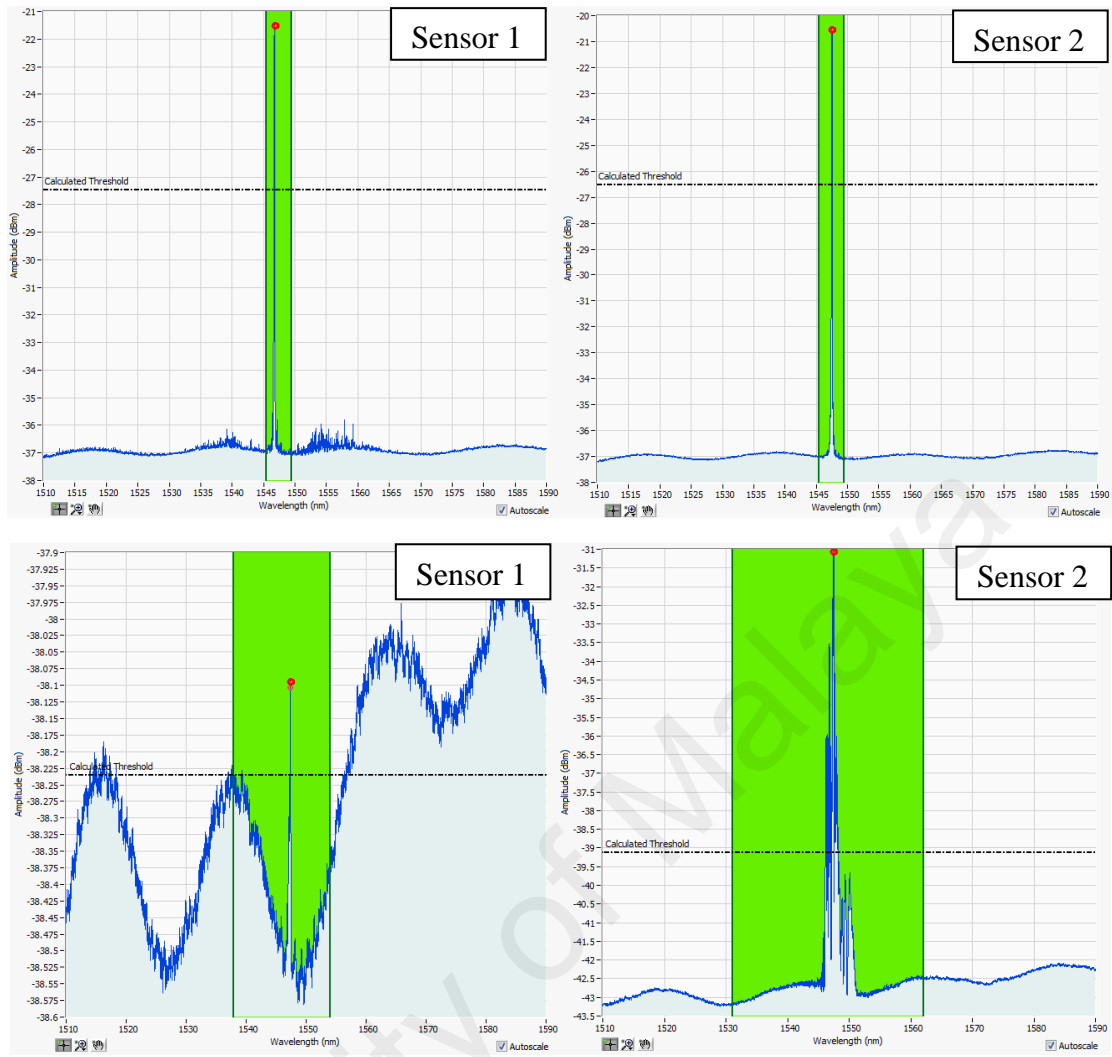


Figure 4.15: Reflected spectrums before and after corrosion experiment obtained from BM3-1 and BM3-2.

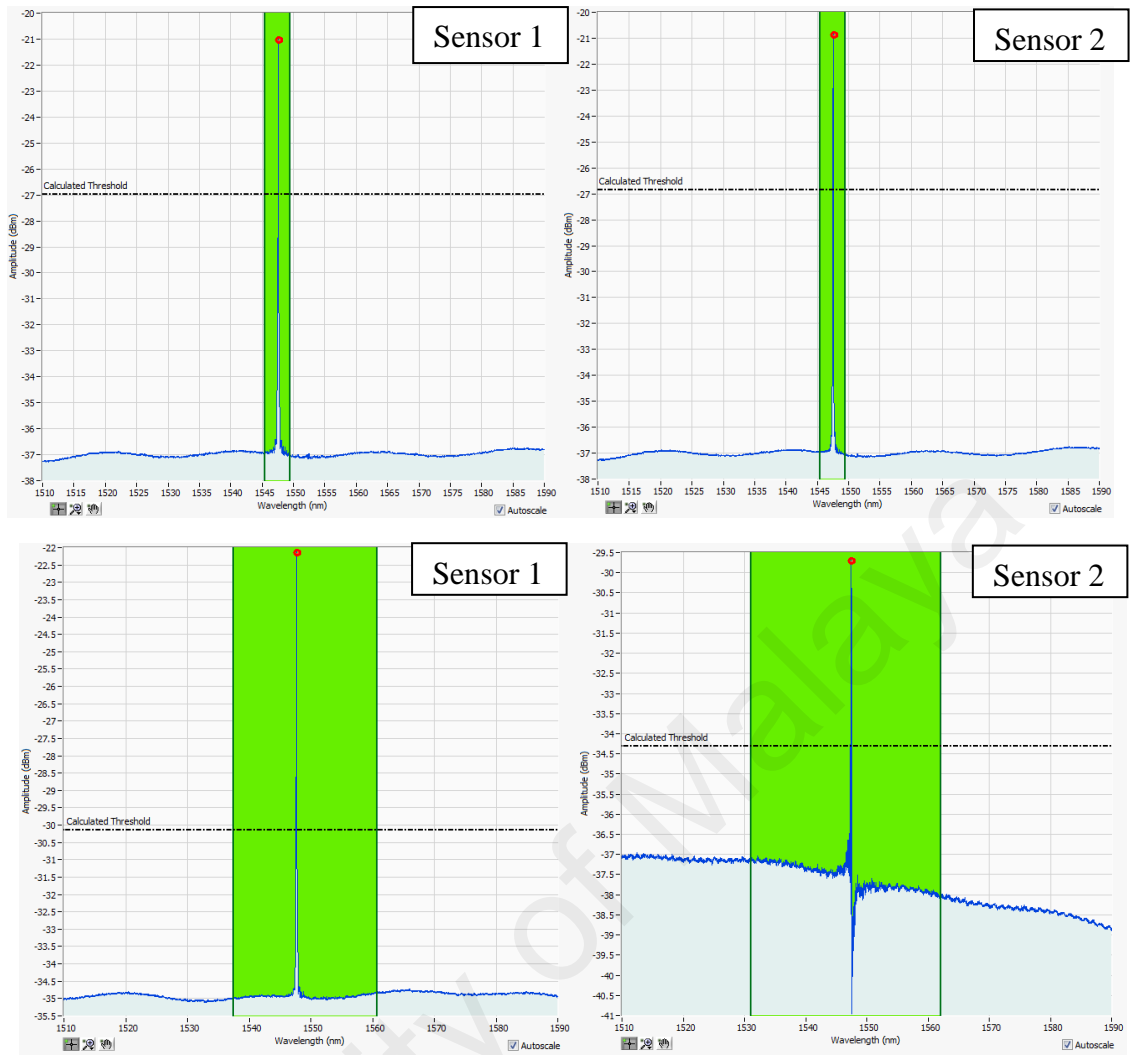


Figure 4.16: Reflected spectrums before and after corrosion experiment obtained from BM2-1 and BM2-2.

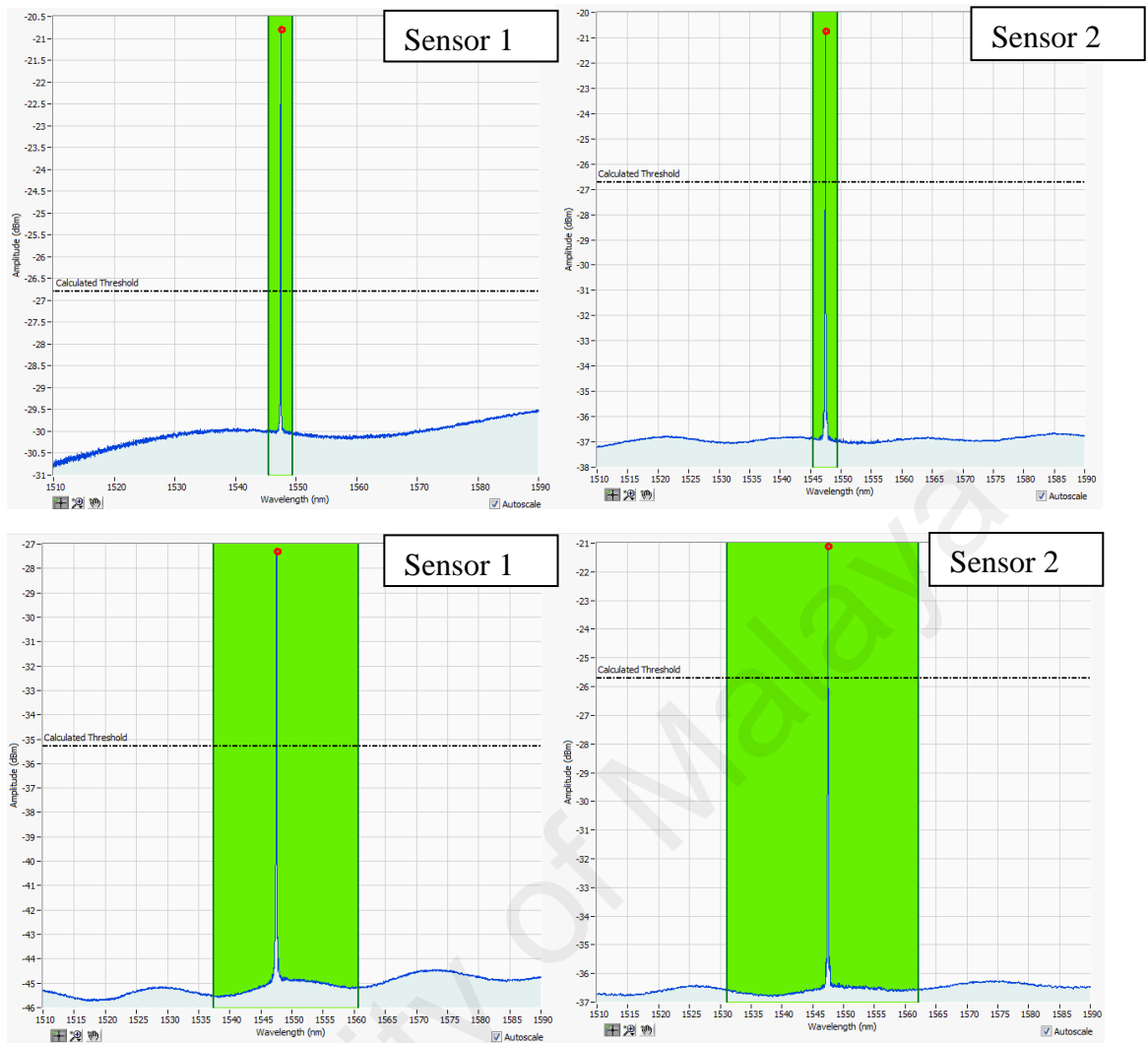
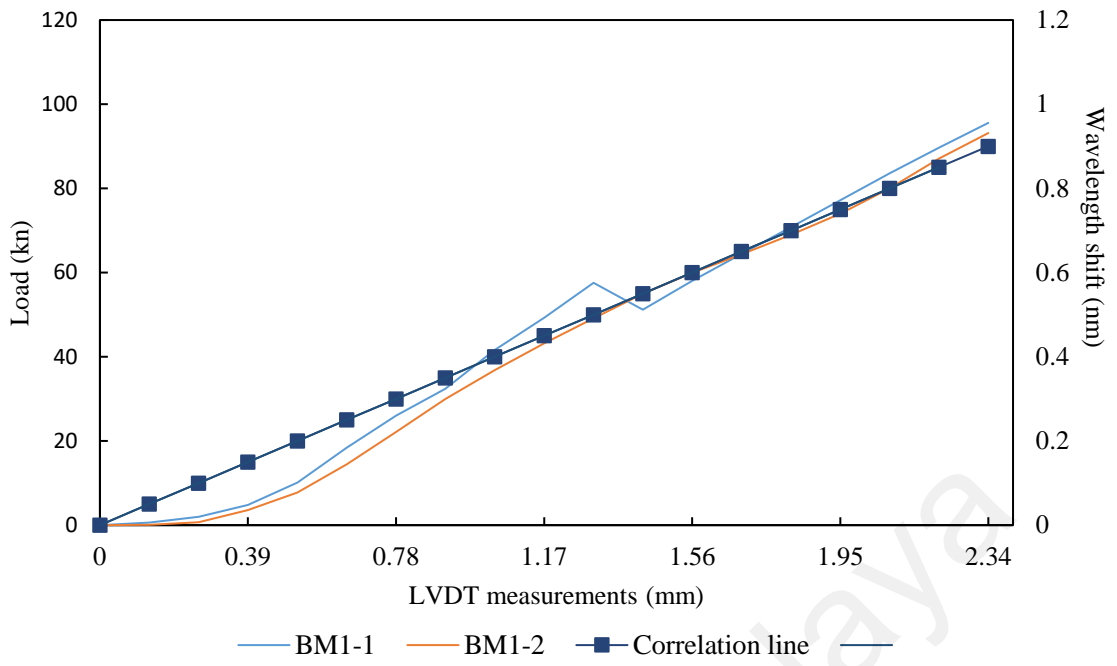


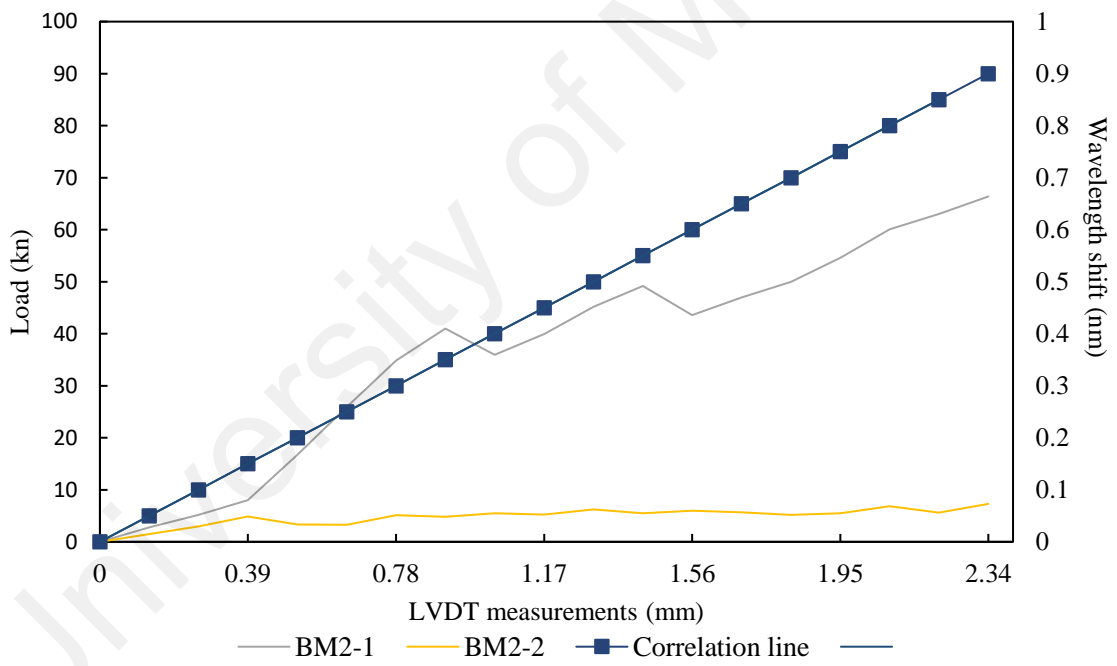
Figure 4.17: Reflected spectrums before and after corrosion experiment obtained from BM1-1 and BM1-2.

4.4. Phase 2 Flexure Test

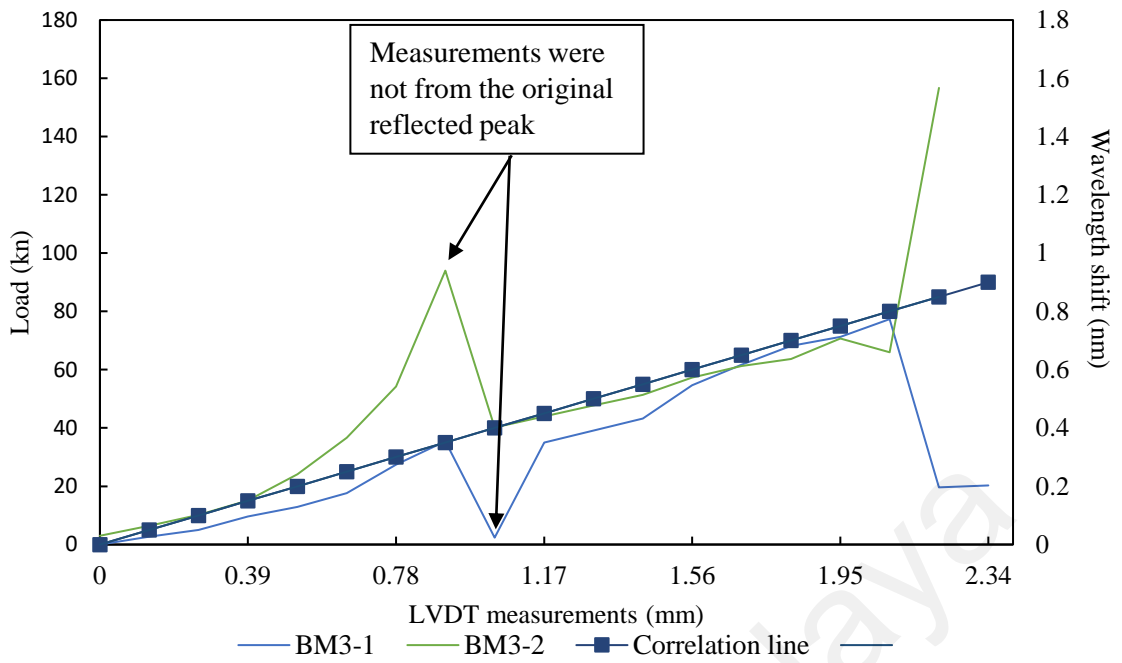
The flexural test performed on the beam specimens was intended at examining bend sensitivity of FBG strain sensors to evaluate the vertical displacement. The moment the beam specimens were bent under vertical progressive mechanical loading, deformation of the FBG sensors occurred accordingly and the resulting wavelength shifts could be correlated with beam displacement. A linear Variable Differential Transducer (LVDT) was used as a reference to measure vertical displacement of beam during the load test. Although some FBG measured data (wavelength shift) were lost or were not from the original reflected peak as shown in Figure 4.18. The dataset collected is sufficient to indicate a relative trend between the vertical displacement of the RC beam specimens and the FBG wavelength shift, giving a correlation coefficient 2.6 m/nm. The FBG measurements were calibrated with LVDT measurements to find the correlation coefficient. In fact, the correlation coefficient was found based mainly on measurements taken from BM1-1 and BM1-2 FBG sensors, in addition to BM2-1, BM3-1 and BM3-2 sensors (see Figure 4.18). Those five FBG sensors were chosen because they had the minimal effect from both cases (missing FBG or detecting non-original peak). In addition, by finding the wavelength shift difference between each 5 kN interval, the coefficient 2.6 m/nm was repeatedly found but not in continuous manner due to the effect from both cases (missing FBG or detecting non-original peak). Therefore, the instrumentation method can be used to monitor vertical displacement, however, an alarm needed to warn when there is a change in original reflected peak detection to insure accuracy of data. Figure 4.19 shows the detection problem where the reflected peak detected changed during flexural loading. This change led to unreliable FBG measurements. In other words, those FBG measured data are not from the original reflected peak, which are identified by observing jumps in the FBG measured obtained from the experiments.



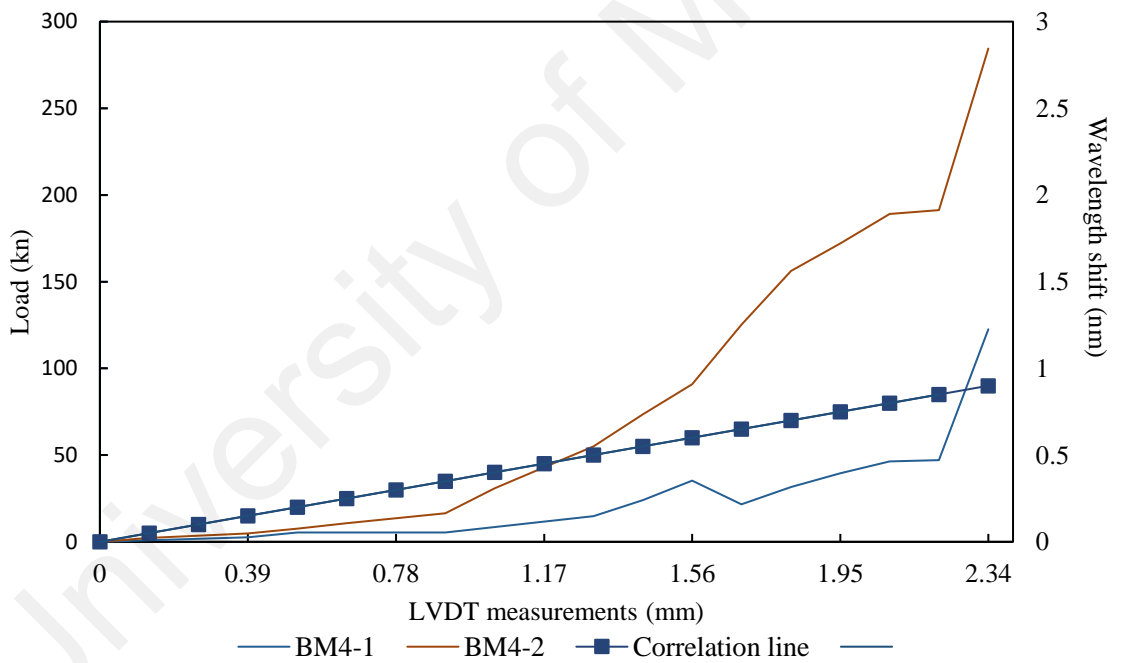
(a)



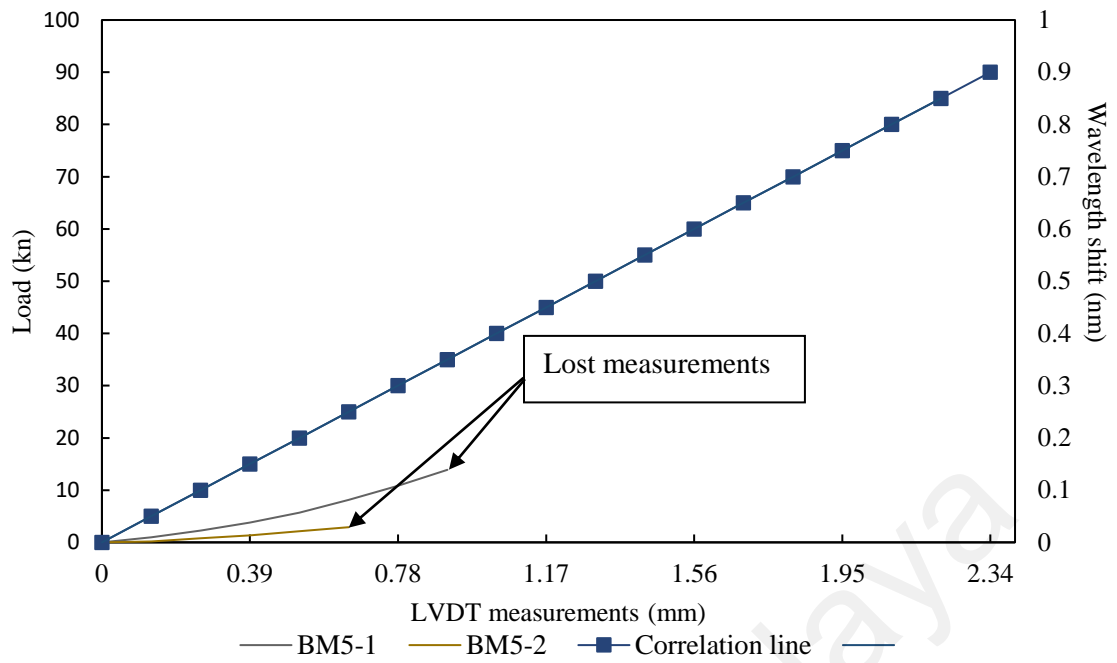
(b)



(c)



(d)



(e)

Figure 4.18: Load vs Wavelength shift vs LVDT measurements of all beams (a) BM1, (b) BM2, (c) BM3, (e) BM4, and (e) BM 5.

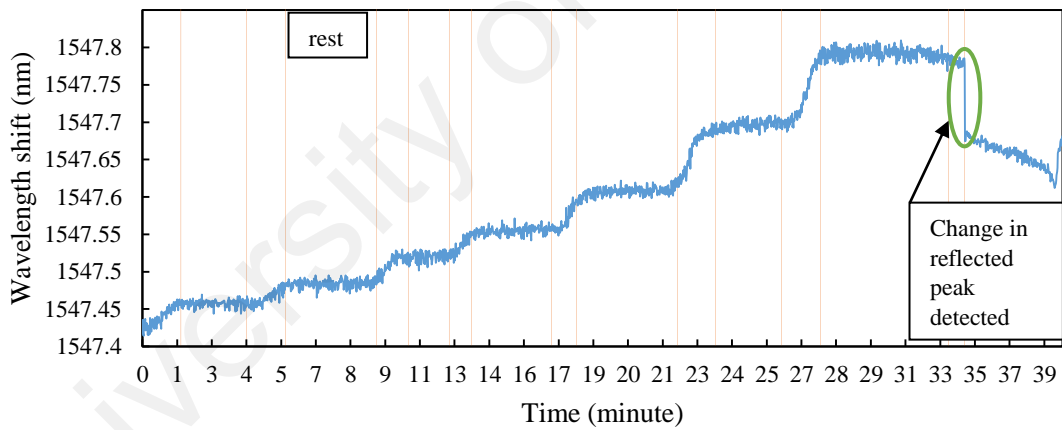


Figure 4.19: Wavelength shift vs time flexure test for BM3-1.

4.5. Identification of FBG Parameters (Reflected Spectrum Shape)

In addition to wavelength shift, the change of Reflected Spectrum Shape (RSS) of FBG was examined. Changes in RSS can be used to differentiate FBG wavelength shifts due to corrosion progression from those caused by vertical displacement. Previous studies showed that changes in RSS can be used effectively to detect damages that occur to material, especially in composites (Trilaksono et al., 2013; Shin et al., 2014; Trilaksono et al., 2014). Such studies used changes in the refracted spectrum as parameter to detect damage severity in composite material encapsulating FBG sensors. Formation and propagation of cracks changed FBG reflected spectrum by creating new peaks (disappearance of the main peak) or by changing power reflection.

Instrumentation of the proposed FBG strain sensing showed efficiency in correlating wavelength shift with corrosion levels and vertical displacement, where the wavelength shift increases with the increment of corrosion level or vertical displacement. However, under corrosion, FBG strain sensors not only showed wavelength shift as output but also RSS changes. The RSS of all corroded beams was found to change with corrosion, especially at high corrosion levels. Peak power reflection of corroded beams decreased, as shown in Table 4.5. Un-corroded beams showed slight reduction in power reflection of the peaks with unchanged RSS. This reduction was resulted from natural corrosion of steel reinforcement, which could have happened during curing of beam specimens. By examining the internal condition of the hacked-opened un-corroded beam after testing, a small volume of corrosion was spotted at the sensor location. It is considered that this corrosion was responsible for the small wavelength shift in sensors of un-corroded beams (sensor 1 wavelength shift = 0.025 nm; sensor 2 wavelength shift = 0.021 nm).

Table 4.5: Power reflection values before and after corrosion and of all beams.

Beam Name	Level of corrosion %	Before corrosion (dBm)		After corrosion (dBm)		Power reflection difference (dBm)	
						Sensor 1	Sensor 2
BM 1	0	-20.75	-20.75	-27.25	-21	6.50	0.25
BM 2	2	-21	-21	-22.25	-29.75	1.25	8.75
BM 3	4	-21.5	-20.5	-38.09	-31	16.59	10.50
BM 4	6	-20.75	-22.75	-24.25	-36	3.50	13.25
BM 5	10	-20.75	-20.75	-26.5	-42.75	5.75	22.00

Based on previous studies (Trilaksono et al., 2013; Shin et al., 2014; Trilaksono et al., 2014), a change in RSS is usually associated with formation of microcracks in FBG or stress-perturbed strain field posed by damage in composite material encapsulating the FBG strain sensors. Shin et al. (2014) indicated that the RSS change, in his study was an increase in background intensity, often arises from the formation of cracks in composite material encapsulating FBG strain sensors. Such cracks create stress-perturbed strain fields on FBG, thereby leading to changes in RSS, while power reflection of the original peak remained unchanged after loading tests (impact loading and fatigue loading tests). By contrast, the results of this study showed that the corrosion of steel reinforcement has changed RSS and power reflection of the original peaks. It is also to be noted that this current study did not use encapsulation as the mounting method for FBG strain sensors. Therefore, it is considered that any shape change in the reflected spectrum was not the result of stress-perturbed strain field on FBG. Based on the fore-mentioned reasons, the change of shape of reflected spectrum as obtained from this current study can be considered to be attributed to microcracks formation in FBG fibers.

Based on the results given in Figure 4.17 and Table 4.5 the trends of change in RSS and the power reflection of original peaks could not be concluded in a straight-forward manner. These parameters did not seem to exhibit a traceable pattern as corrosion progressed, perhaps because of two reasons. The first reason is non-uniformity of

corrosion at the restrained FGB end by epoxy (see a). The second reason is the limitation of interrogator used in the present study (National Instrument PXIe-4844) to monitor changes in the reflected spectrum; this interrogator can only monitor wavelength shift in real time. On the other hand, the spectrum analyzer (MS9710C, Anritsu Co.) used by Trilaksono et al. (2013) could detect changes in the reflected spectrum (occurrence of multiple peaks and variation in wavelength width). In this study, the change of wavelength shift was used to evaluate corrosion and vertical displacement of beam specimens, whereas change of RSS was used to differentiate wavelength shifts caused by corrosion from those by displacement. Reduction of the highest peak (original peak) can be used as degradation indicator, as demonstrated by Trilaksono et al. (2014) (See Figure 2.19). However, in this study, the reduction of the highest peak serves as an indicator of corrosion progression (Table 4.5).

4.6. Shewhart Control Chart for Statistical Analysis Controlling Model

The change of RSS was found to affect detection of wavelength shift of the original reflected peak. In this study, a statistical model concerns the implementation of an appropriate algorithm was developed to alarm if there is a change in the detection of the original reflected peak caused by change in RSS to prevent loss of FBG data.

In section 3.5, discussion was directed on detection of original peak. The detection was done by setting of wavelength boundaries (nm), threshold (dBm) around the desired peak (designed peak), and minimum width (nm) were critical in enabling NI-OSI Explorer to detect the original peak, as shown in Figure 3.17. However, the original peaks of FBGs of the corroded beam specimens spread widely and split heavily into distinct peaks, which occasionally led to failure of detection of the original peak. In other words, detection of non-original peaks took place. Therefore, a statistical analysis controlling

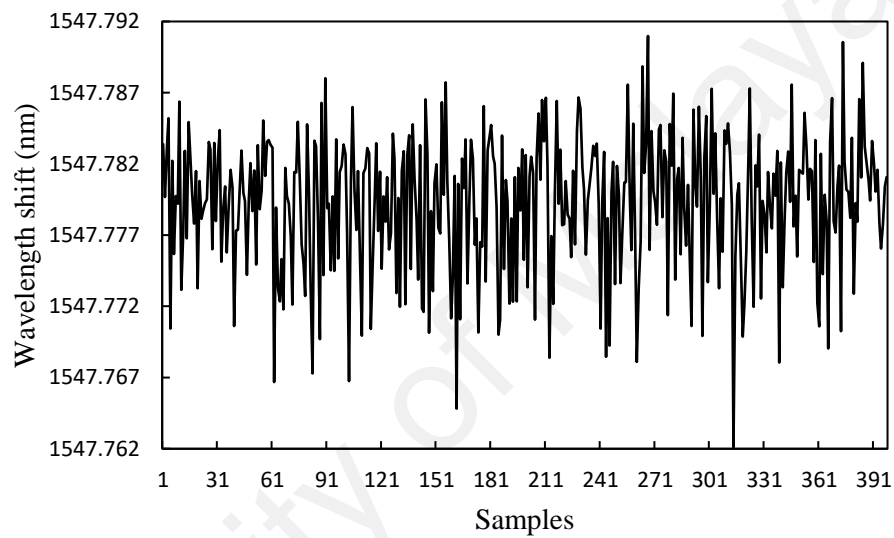
model is developed herein to serve the purpose of alerting users of any change of the detected peaks, so the correct changes can be reflected in the settings of NI-OSI explorer to prevent any data loss.

As seen from Figure 4.13 to 4.17, the original peaks of FBGs of corroded beam specimens could still be recognized. However, these peaks were not as distinct as they were before corrosion experiments because of the change of RSS. This study used bare FBG strain sensors with direct contact with the steel reinforcement surface except for one part that was covered with epoxy resin (see Figure 3.8). Epoxy resin was used to fix FBG to their position. Microcracks occurred on the FBG near the epoxy region because of increment in corrosion product volume, thereby inducing stresses on the FBG fibers. The flat smooth end of fractured fibers acted as a mirror that reflected light without discrimination on wavelength (Shin et al., 2014). Such effect caused change of RSS such as increases in background intensity causing disappearance of FBG reflection peak, original peak spread widely and split heavily into distinct peaks, and/or reduction of power reflection. In this study, control chart was developed to alarm of change of reflected peak detected.

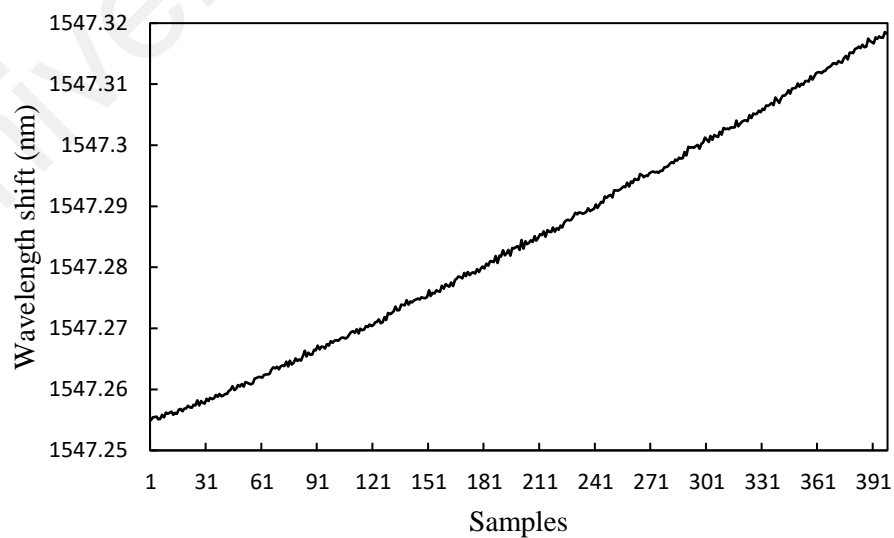
The construction of control chart was based on the study of Fugate et al. (2001). Figure 2.20 shows the flow chart of the steps followed, the first step concerns selecting a FBG parameter for evaluation, which is the wavelength shift in this study. Second, measured data was modeled after an appropriate time-series auto-regressive (AR) model. The AR model used to eliminate correlation between the data observed, thereby eliminating false alarms provided by control charts constructed from the correlated data (Montgomery, 2007). The AR(5) (Equation 2.6) was used in this analysis to obtain its residual errors formed from fitting it to the original wavelength shift measurements. The

residuals were used for the construction of control charts, which are uncorrelated with no systematic pattern. Thus, residual errors served as Damage Sensitive Feature (DSF). Residual errors were normalized and sub-divided into groups of size four so that measured data within each group are more similar than measured data between groups. Finally, a X-bar control chart was constructed (Shewhart chart) using the measurement results obtained from this study to resolve the detection problem faced during monitoring. The upper control limit (UCL), lower control limit (LCL) and center line (CL) of the control chart were obtained using equation 2.7. From the experimental data of this study, undamaged measured data were totalled at 397 and they were divided into 98 sub-groups. The same number of measured data were taken for each case. Figure 4.20 shows the wavelength shift measurements cases, which are wavelength shift measurements obtained from undamaged state of specimen (see Figure 4.20a), wavelength shift caused by displacement or by corrosion (see Figure 4.20b), and wavelength shift resulting from the detection of unwanted peaks cases (see Figure 4.20c and d). Following the control chart construction, the DSF of all cases were charted on the control chart. Figure 4.21 shows X-bar control charts of residual errors of all cases. Undamaged and displacement cases failed to show any changes in the number of outliers or abnormal charted values or observed obvious patterns such as consecutive five charted data above the mean followed by consecutive five charted below the mean line (Fugate et al., 2001). By contrast, the third case (unwanted peak detection), as shown in Figure 4.21 (c) and (d), did not give any difference in the number of outliers. However, abnormal charted values and specific patterns were observed. The abnormal charted values exceeded 1.5 which was not observed in the first two cases. While the charted values have showed a specific pattern, where they either continued over or below the mean line (CL). This abnormal pattern is regarded as “shift” and is recognized by a shift of the charted data below or above the mean line (CL) (El-Midany et al., 2010). Therefore, control charts can be used to alert

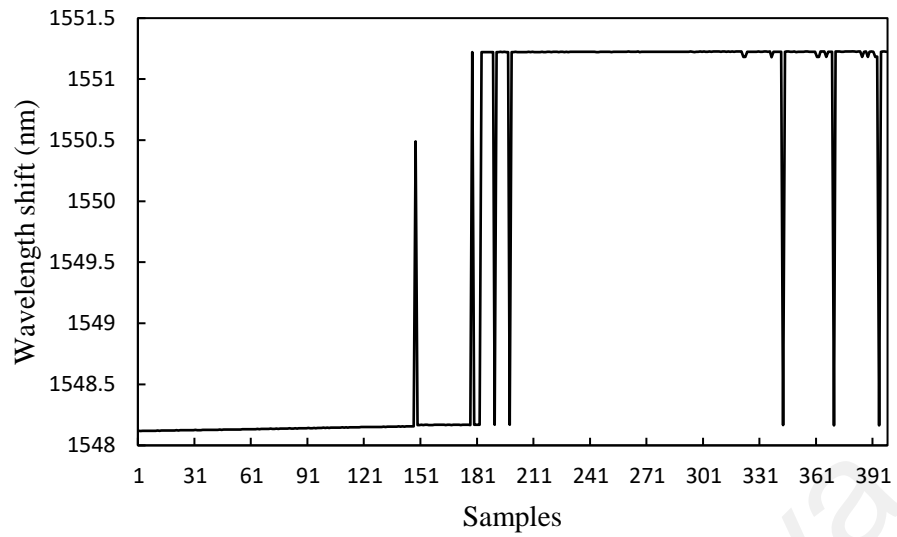
users regarding change in reflected peak detected. In summary, the presence of unnatural patterns and/or abnormal charted values indicate that the monitored wavelength shift is not from the original reflected peak (detection problem), and corrective actions should be taken by changing the settings of NI-OSI explorer (wavelength boundaries (nm), threshold (dBm), and minimum width (nm)). The corrective actions can eliminate the loss of FBG measurements due to detection problem, which improve data analysis and interpretation.



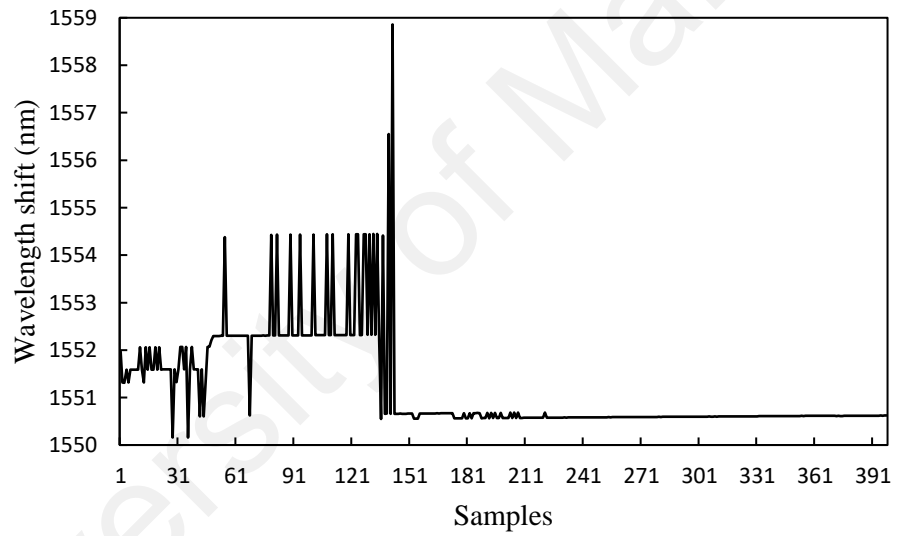
(a)



(b)

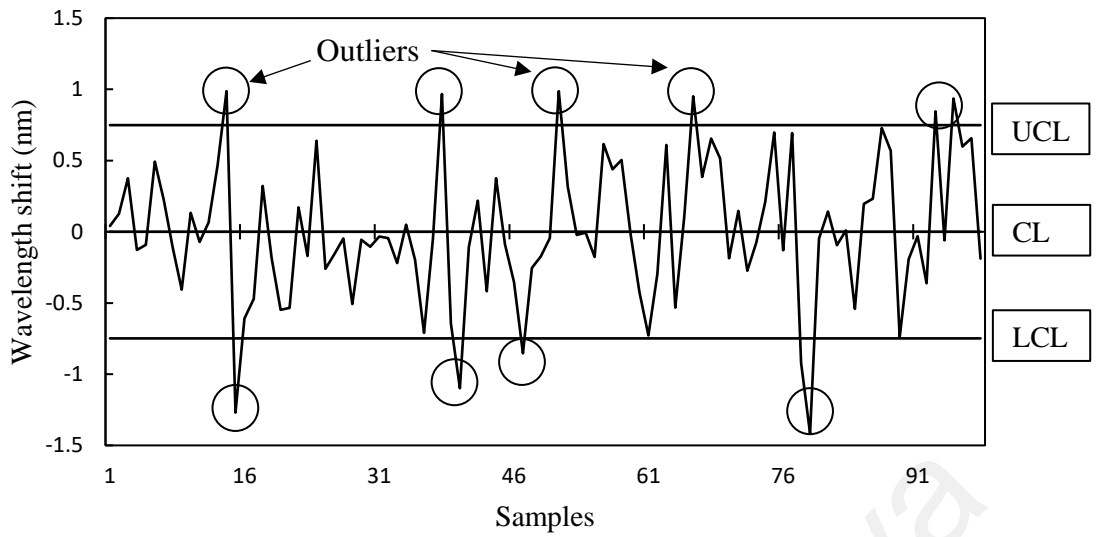


(c)

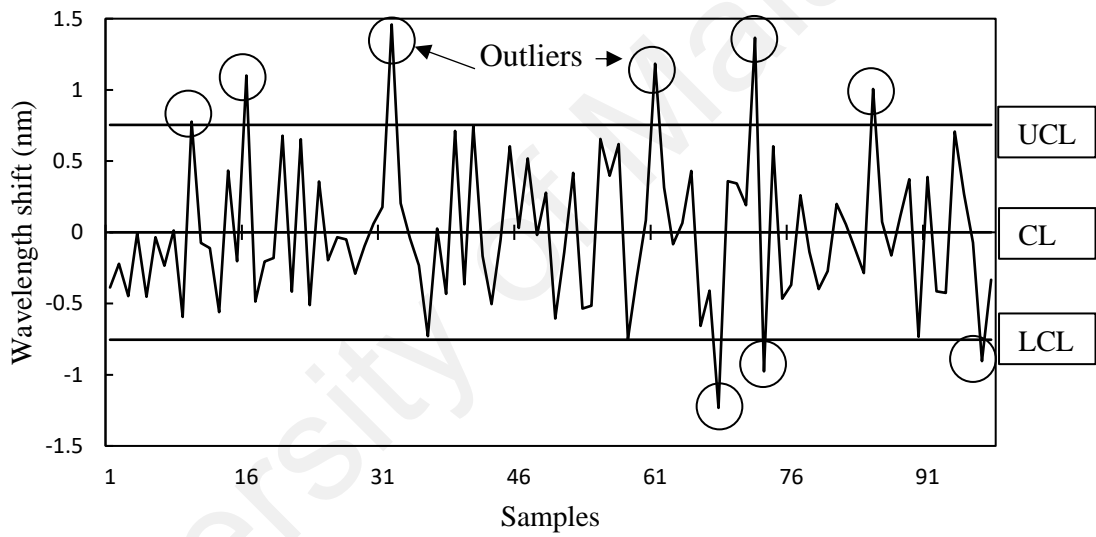


(d)

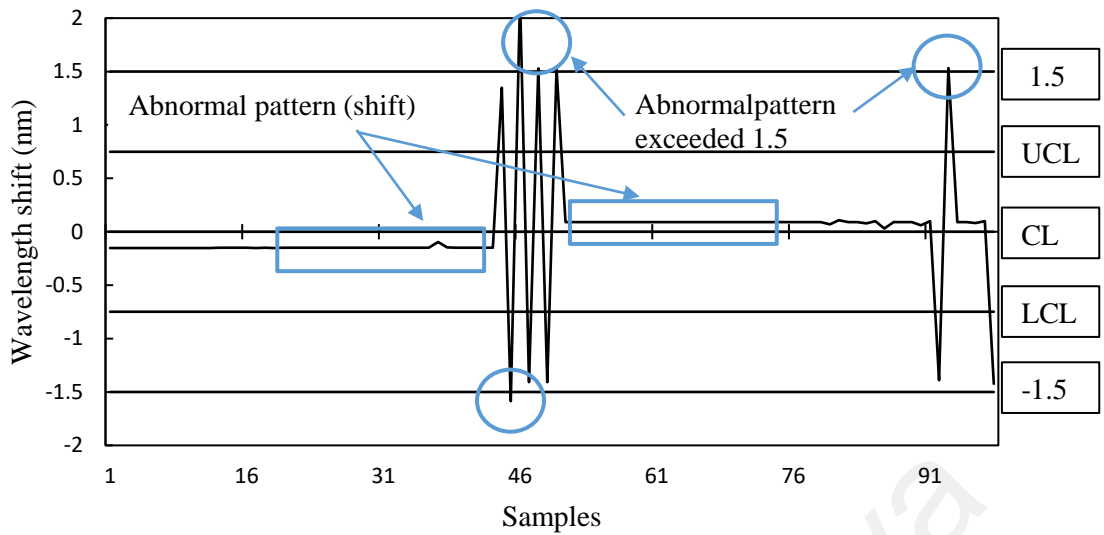
Figure 4.20: Original reflected peak wavelength shift of undamaged case (a)
 Wavelength shift due to vertical displacement or corrosion case (b) wavelength shift of
 unwanted peaks case example 1 (b) and example 2 (c).



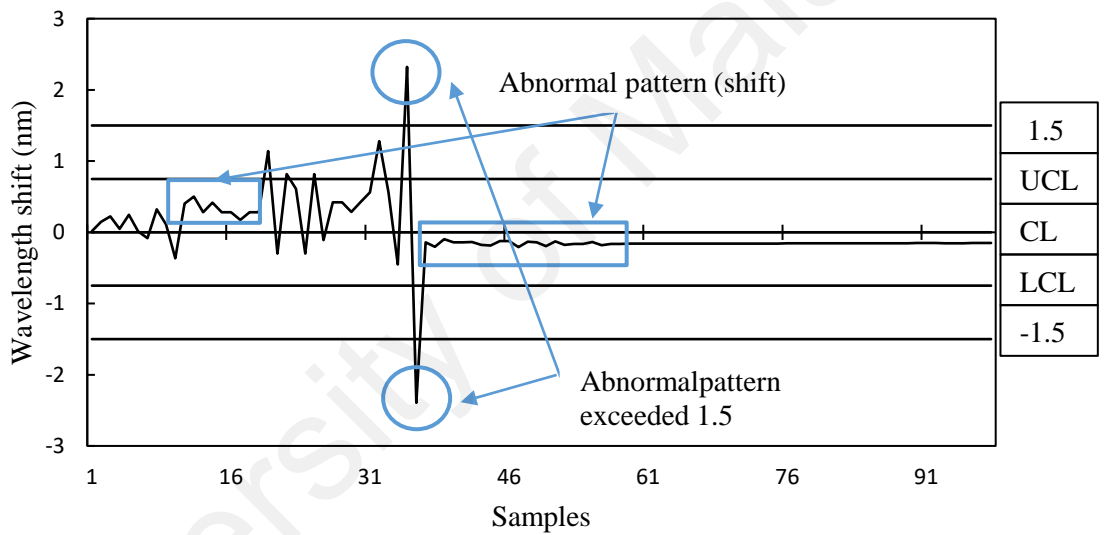
(a)



(b)



(c)



(d)

Figure 4.21: X-bar control charts of undamaged case (a) Wavelength shift due to vertical displacement or corrosion case (b) wavelength shift of unwanted peaks case example 1 (b) and example 2 (c).

CHAPTER 5: CONCLUSIONS AND RECOMMENDATIONS

Assessing the state of steel reinforcement corrosion and its resulting effect on vertical displacements of RC structural members are crucial for effective structural health monitoring practice. Thereby, the primary objective of this study is to provide a feasible instrumentation method for FBG strain sensing, which allows FBG strain sensors to monitor corrosion progression in steel reinforcements and the change of displacement resulting from load increment. The instrumentation method allows the FBG strain sensor to be in direct contact with steel reinforcements, while being protected by Polystyrene foam as buffer material. The instrumentation method was tested in laboratory experiments, where two types of specimens were tested (cylindrical and beam specimens). The major findings of this study are summarized as follows:

- 1- The proposed instrumentation method, in specific the FBG sensor mounting method, was effective in providing good protection to the sensors during casting and hardening of concrete, as well as throughout the accelerated corrosion tests. Also, it allowed the FBG sensor to detect corrosion without getting damage, even though the accelerated corrosion tests last up to 10 days to achieve a corrosion level of 10%.
- 2- Based on the laboratory work, the FBG sensing measurements were correlated with structural parameters as follows:
 - The increase in FBG wavelength shifts and the change trend of reflected spectrum shape (increase of background intensity and increase in wavelength width) were used as an indicator for corrosion progression of the embedded steel reinforcements.
 - Based on the number of specimens tested, FBG measurements were calibrated with vertical displacement of RC beams by using LVDT (the correlation coefficient is 2.6 m/nm). However, some beam specimens have not followed

the same correlation coefficient due to the FBG detection problem which leads to change of reflected peak detected.

- 3- A statistical analysis controlling model (Shewhart Control Chart) for FBG sensing was developed to assess the FBG measurements accuracy and interpretation, by alarming the users when there is a change in reflected peak detected. Moreover, corrective actions in NI-OSI explorer settings are required to prevent data loss.

Considering the instrumentation method's low cost, size, and manner of installation, instrumentation method should be used for monitoring bridges. It is suggested that the installation method should be made during the construction stage to ensure the earliest detection of corrosion. The sensor instrumentation adopted in this study is also considered a point sensor in which by using multiplex properties of FBG sensing. A chain of sensors could be placed along the bridge span, to obtain accurate and improved interpretation of measurements.

Further studies will still be required to improve the proposed FBG instrumentation and validate its robustness. To apply this method more efficiently, additional focus may be extended based on the achievements in this research. The following concerns can be considered as future studies which are highly required to improve the current method.

- The geometry and support conditions are mainly designed in a single span. Further study could be done in other structural forms, such as cantilever beam, to evaluate the feasibility of this method for different structural members that have different bending mechanism.
- Utilize a more sophisticated data acquisition system, namely an integrator that could detect the changes in the reflected spectrum shape of the FBG sensors

such as spectrum analyzer MS9710C, Anritsu Co. thus a better correlation with corrosion progression could be found.

- Apply the statistical analysis controlling model (Shewhart control chart) for real time monitoring by developing a dedicated algorithm compatible with NI-OSI explorer and LabVIEW.
- Use FBG strain sensors with higher bend sensitivity compare to normal FBG strain sensors such as multiple-core fiber with an asymmetric axially offset FBG. This kind of sensors will give higher sensitivity to changes in corrosion volume.

University of Malaya

REFERENCES

- ACI-408R-03. (2003). Bond and Development of Straight Reinforcing Bars in Tension. *American Concrete Institute, Detroit, Michigan, US.*
- Bentur, A., Berke, N., & Diamond, S. (1997). *Steel corrosion in concrete: fundamentals and civil engineering practice*: CRC Press.
- Bock, W. J., Chen, J., Mikulic, P., & Eftimov, T. (2007). A novel fiber-optic tapered long-period grating sensor for pressure monitoring. *IEEE transactions on instrumentation and measurement*, 56(4), 1176-1180.
- Boerstler, J. T., & Frankel, G. S. (2017). *Accelerated Corrosion Degradation of Coated Aluminum Alloy Systems through Galvanic Interactions*. Paper presented at the Meeting Abstracts.
- Brockwell, P., & DAVIS, R. (1991). *Time Series: Theory and Methods*: Springer-Verlag, New York.
- BS-EN. (2000). 12696: 2000, Cathodic Protection of Steel in Concrete. *British Standards Institution, London.*
- Bushman, J. B., & Engineer, P. P. C. (2000). Calculation of Corrosion Rate from Corrosion Current (Faraday's Law). *Bushman & Associates Inc.*
- Caré, S., & Raharinaivo, A. (2007). Influence of impressed current on the initiation of damage in reinforced mortar due to corrosion of embedded steel. *Cement and concrete research*, 37(12), 1598-1612.
- Chen, C., Caucheteur, C., Mégret, P., & Albert, J. (2007). The sensitivity characteristics of tilted fibre Bragg grating sensors with different cladding thicknesses. *Measurement Science and Technology*, 18(10), 3117.
- Chen, D., & Mahadevan, S. (2008). Chloride-induced reinforcement corrosion and concrete cracking simulation. *Cement and Concrete Composites*, 30(3), 227-238.

- Chen, W., & Dong, X. (2012). Modification of the wavelength-strain coefficient of FBG for the prediction of steel bar corrosion embedded in concrete. *Optical Fiber Technology*, 18(1), 47-50.
- Chen, X., Zhang, C., Webb, D. J., Peng, G.-D., & Kalli, K. (2010). Bragg grating in a polymer optical fibre for strain, bend and temperature sensing. *Measurement Science and Technology*, 21(9), 094005.
- Chess, P. M., & Broomfield, J. P. (2003). *Cathodic protection of steel in concrete*: CRC Press.
- Chindaprasirt, P., Hatanaka, S., Chareerat, T., Mishima, N., & Yuasa, Y. (2008). Cement paste characteristics and porous concrete properties. *Construction and Building Materials*, 22(5), 894-901.
- Choi, S. W., Lee, J., Oh, B. K., & Park, H. S. (2016). Analytical models for estimation of the maximum strain of beam structures based on optical fiber Bragg grating sensors. *Journal of Civil Engineering and Management*, 22(1), 86-91.
- Christodoulou, C., Glass, G., Webb, J., Austin, S., & Goodier, C. (2010). Assessing the long term benefits of Impressed Current Cathodic Protection. *Corrosion Science*, 52(8), 2671-2679.
- De Larrard, F. (1999). *Concrete mixture proportioning: a scientific approach*: CRC Press.
- Doebbling, S. W., Farrar, C. R., Prime, M. B., & Shevitz, D. W. (1996). Damage identification and health monitoring of structural and mechanical systems from changes in their vibration characteristics: a literature review: Los Alamos National Lab., NM (United States).
- Dong, X., Liu, Y., Liu, Z., & Dong, X. (2001). Simultaneous displacement and temperature measurement with cantilever-based fiber Bragg grating sensor. *Optics Communications*, 192(3), 213-217.
- Du Béton, F. I. (2000). Bond of reinforcement in concrete: state-of-art report. *Bulletin*, 10, 160-167.
- El-Midany, T. T., El-Baz, M., & Abd-Elwahed, M. (2010). A proposed framework for control chart pattern recognition in multivariate process using artificial neural networks. *Expert Systems with Applications*, 37(2), 1035-1042.

- El Maaddawy, T. A., & Soudki, K. A. (2003). Effectiveness of impressed current technique to simulate corrosion of steel reinforcement in concrete. *Journal of materials in civil engineering*, 15(1), 41-47.
- Erdogan, T., & Sipe, J. (1996). Tilted fiber phase gratings. *JOSA A*, 13(2), 296-313.
- Fang, C., Lundgren, K., Chen, L., & Zhu, C. (2004). Corrosion influence on bond in reinforced concrete. *Cement and concrete research*, 34(11), 2159-2167.
- Farrar, C. R., & Worden, K. (2007). An introduction to structural health monitoring. *Philosophical Transactions of the Royal Society of London A: Mathematical, Physical and Engineering Sciences*, 365(1851), 303-315.
- Flockhart, G., MacPherson, W., Barton, J., Jones, J., Zhang, L., & Bennion, I. (2003). Two-axis bend measurement with Bragg gratings in multicore optical fiber. *Optics letters*, 28(6), 387-389.
- Fugate, M. L., Sohn, H., & Farrar, C. R. (2001). Vibration-based damage detection using statistical process control. *Mechanical Systems and Signal Processing*, 15(4), 707-721.
- Gao, J., Wu, J., Li, J., & Zhao, X. (2011). Monitoring of corrosion in reinforced concrete structure using Bragg grating sensing. *NDT & E International*, 44(2), 202-205.
- García, K., Morales, A., Barrero, C., & Greneche, J. (2006). New contributions to the understanding of rust layer formation in steels exposed to a total immersion test. *Corrosion Science*, 48(9), 2813-2830.
- Gouveia, C. A., Baptista, J. M., & Jorge, P. A. (2013). Refractometric Optical Fiber Platforms for Label Free Sensing. *Current Developments in Optical Fiber Technology*, Dr. Sulaiman Wadi Harun (Ed.), ISBN, 978-953.
- Grattan, S., Basheer, P., Taylor, S., Zhao, W., Sun, T., & Grattan, K. (2007). *Fibre Bragg grating sensors for reinforcement corrosion monitoring in civil engineering structures*. Paper presented at the Journal of Physics: Conference Series.
- Guan, B. O., Tam, H. Y., & Liu, S. Y. (2004). Temperature-independent fiber Bragg grating tilt sensor. *IEEE Photonics Technology Letters*.

- Guh, R. S. (2002). Robustness of the neural network based control chart pattern recognition system to non-normality. *International Journal of Quality & Reliability Management*, 19(1), 97-112.
- Guo, T., Ivanov, A., Chen, C., & Albert, J. (2008). Temperature-independent tilted fiber grating vibration sensor based on cladding-core recoupling. *Optics letters*, 33(9), 1004-1006.
- Hao, K. C., Hassan, A., & Ismail, A. S. (2005). A Preliminary Framework for a Web-based Control Chart Pattern Recognition System.
- Hassan, M. R. A., Bakar, M. H. A., Dambul, K., & Adikan, F. R. M. (2012). Optical-based sensors for monitoring corrosion of reinforcement rebar via an etched cladding Bragg grating. *Sensors*, 12(11), 15820-15826.
- Hong, C. Y., Zhang, Y. F., Zhang, M. X., Leung, L. M. G., & Liu, L. Q. (2016). Application of FBG sensors for geotechnical health monitoring, a review of sensor design, implementation methods and packaging techniques. *Sensors and Actuators A: Physical*, 244, 184-197.
- Hu, W., Cai, H., Yang, M., Tong, X., Zhou, C., & Chen, W. (2011). Fe-C-coated fibre Bragg grating sensor for steel corrosion monitoring. *Corrosion Science*, 53(5), 1933-1938.
- Islam, M. R., Bagherifaez, M., Ali, M. M., Chai, H. K., Lim, K.-S., & Ahmad, H. (2015). Tilted fiber bragg grating sensors for reinforcement corrosion measurement in marine concrete structure. *IEEE transactions on instrumentation and measurement*, 64(12), 3510-3516.
- Islam, M. R., Gunawardena, D. S., Lee, Y.-S., Lim, K.-S., Yang, H. Z., & Ahmad, H. (2016). Fabrication and characterization of laser-ablated cladding resonances of two different-diameter photosensitive optical fibers. *Sensors and Actuators A: Physical*, 243, 111-116.
- Jensen, W. A., Jones-Farmer, L. A., Champ, C. W., & Woodall, W. H. (2006). Effects of parameter estimation on control chart properties: a literature review. *Journal of Quality Technology*, 38(4), 349.
- Kersey, A. D., Davis, M. A., Patrick, H. J., LeBlanc, M., Koo, K., Askins, C., . . . Friebele, E. J. (1997). Fiber grating sensors. *Journal of Lightwave Technology*, 15(8), 1442-1463.

- Khatri, R., & Sirivivatnanon, V. (2004). Characteristic service life for concrete exposed to marine environments. *Cement and concrete research*, 34(5), 745-752.
- Khudhair, A. M., & Farid, M. M. (2004). A review on energy conservation in building applications with thermal storage by latent heat using phase change materials. *Energy conversion and management*, 45(2), 263-275.
- Koleva, D., Guo, Z., Van Breugel, K., & De Wit, J. (2009). Conventional and pulse cathodic protection of reinforced concrete: electrochemical behavior of the steel reinforcement after corrosion and protection. *Materials and corrosion*, 60(5), 344-354.
- Kouroussis, G., Kinet, D., Moeyaert, V., Caucheteur, C., & Dupuy, J. (2016). *Development of structural railway monitoring solutions using FBG sensors*. Paper presented at the Proceedings of the 23rd International Congress on Sound and Vibration—ICSV23. Athens (Greece).
- Li, C. Q., & Melchers, R. E. (2005). Time-dependent risk assessment of structural deterioration caused by reinforcement corrosion. *ACI structural journal*, 102(5), 754.
- Lim, J., Yang, Q., Jones, B. E., & Jackson, P. R. (2002). Strain and temperature sensors using multimode optical fiber Bragg gratings and correlation signal processing. *IEEE transactions on instrumentation and measurement*, 51(4), 622-627.
- Lin, C. Y., Wang, L. A., & Chern, G. W. (2001). Corrugated long-period fiber gratings as strain, torsion, and bending sensors. *Journal of Lightwave Technology*, 19(8), 1159.
- Lyu, M., Zhu, X., & Yang, Q. (2017). Connection stiffness identification of historic timber buildings using Temperature-based sensitivity analysis. *Engineering Structures*, 131, 180-191.
- Ma, G. M., Li, C. R., Jiang, J., Liang, J. Y., Luo, Y. T., & Cheng, Y. C. (2012). A passive optical fiber anemometer for wind speed measurement on high-voltage overhead transmission lines. *IEEE transactions on instrumentation and measurement*, 61(2), 539-544.
- Majumder, M., Gangopadhyay, T. K., Chakraborty, A. K., Dasgupta, K., & Bhattacharya, D. K. (2008). Fibre Bragg gratings in structural health monitoring—Present status and applications. *Sensors and Actuators A: Physical*, 147(1), 150-164.

- Mao, J., Chen, J., Cui, L., Jin, W., Xu, C., & He, Y. (2015). Monitoring the Corrosion Process of Reinforced Concrete Using BOTDA and FBG Sensors. *Sensors*, 15(4), 8866-8883.
- Martinez, A., Lai, Y., Dubov, M., Khrushchev, I., & Bennion, I. (2005). *Vector bending sensors based on fiber Bragg gratings inscribed by an infrared femtosecond laser*. Paper presented at the Lasers and Electro-Optics, 2005.(CLEO). Conference on.
- Melo, L., Rodrigues, J., Farinha, A., Marques, C., Bilro, L., Alberto, N., . . . Nogueira, R. (2014). Concentration sensor based on a tilted fiber Bragg grating for anions monitoring. *Optical Fiber Technology*, 20(4), 422-427.
- Montgomery, D. C. (2007). *Introduction to statistical quality control*: John Wiley & Sons.
- Moses, F., Lebet, J. P., & Bez, R. (1994). Applications of field testing to bridge evaluation. *Journal of Structural Engineering*, 120(6), 1745-1762.
- Mousa, M. I. (2015). Effect of bond loss of tension reinforcement on the flexural behaviour of reinforced concrete beams. *HBRC Journal*.
- Pantazopoulou, S., & Papoulia, K. (2001). Modeling cover-cracking due to reinforcement corrosion in RC structures. *Journal of Engineering Mechanics*, 127(4), 342-351.
- Patrick, H. J. (2000). Self-aligning bipolar bend transducer based on long period grating written in eccentric core fibre. *Electronics Letters*, 36(21), 1763-1764.
- Pereira, G., McGugan, M., & Mikkelsen, L. P. (2016). Method for independent strain and temperature measurement in polymeric tensile test specimen using embedded FBG sensors. *Polymer Testing*, 50, 125-134.
- Perry, M. B., Spoerre, J. K., & Velasco, T. (2001). Control chart pattern recognition using back propagation artificial neural networks. *International Journal of production research*, 39(15), 3399-3418.
- Pham, D., & Wani, M. (1997). Feature-based control chart pattern recognition. *International Journal of production research*, 35(7), 1875-1890.

- Qiao, G., Guo, B., Li, Z., Ou, J., & He, Z. (2017). Corrosion behavior of a steel bar embedded in a cement-based conductive composite. *Construction and Building Materials*, 134, 388-396.
- Rao, Y. J. (1999). Recent progress in applications of in-fibre Bragg grating sensors. *Optics and lasers in Engineering*, 31(4), 297-324.
- Rytter, A. (1993). Vibrational based inspection of civil engineering structures.
- Saraf, V., & Nowak, A. S. (1998). Proof load testing of deteriorated steel girder bridges. *Journal of Bridge Engineering*, 3(2), 82-89.
- Shen, C., Zhang, Y., Zhou, W., & Albert, J. (2014). Au-coated tilted fiber Bragg grating twist sensor based on surface plasmon resonance. *Applied Physics Letters*, 104(7), 071106.
- Shin, C.-S., Liaw, S.-K., & Yang, S.-W. (2014). Post-impact fatigue damage monitoring using fiber Bragg grating sensors. *Sensors*, 14(3), 4144-4153.
- Siad, A., Bencheikh, M., & Hussein, L. (2017). Effect of combined pre-cracking and corrosion on the method of repair of concrete beams. *Construction and Building Materials*, 132, 462-469.
- Sohn, H., Farrar, C. R., Hemez, F. M., Shunk, D. D., Stinemates, D. W., Nadler, B. R., & Czarnecki, J. J. (2003). A review of structural health monitoring literature: 1996–2001. *Los Alamos National Laboratory, USA*.
- Song, H. W., & Saraswathy, V. (2007). Corrosion monitoring of reinforced concrete structures-a. *Int. J. Electrochem. Sci*, 2, 1-28.
- Tan, C., Shee, Y., Yap, B., & Adikan, F. M. (2016). Fiber Bragg grating based sensing system: early corrosion detection for structural health monitoring. *Sensors and Actuators A: Physical*, 246, 123-128.
- Torres-Acosta, A. A., Navarro-Gutierrez, S., & Terán-Guillén, J. (2007). Residual flexure capacity of corroded reinforced concrete beams. *Engineering Structures*, 29(6), 1145-1152.
- Trilaksono, A., Watanabe, N., Hoshi, H., Kondo, A., Iwahori, Y., & Takeda, S.-I. (2013). Continuous Damage Monitoring of a Thin Composite Structural with

Mismatched Stiffener in a Combined Joint Using Fiber Bragg Grating under Tension and Three-Point Loading.

Trilaksono, A., Watanabe, N., Kondo, A., Hoshi, H., & Iwahori, Y. (2014). Automatic Damage Detection and Monitoring of a Stitch Laminate System Using a Fiber Bragg Grating Strain Sensor. *Open Journal of Composite Materials*, 2014.

Yang, D., Du, L., Xu, Z., Jiang, Y., Xu, J., Wang, M., . . . Wang, H. (2014). Magnetic field sensing based on tilted fiber Bragg grating coated with nanoparticle magnetic fluid. *Applied Physics Letters*, 104(6), 061903.

Yau, M., Chan, T., Thambiratnam, D., & Tam, H. (2011). *Using fiber Bragg grating (FBG) sensors for vertical displacement measurement of bridges*. Paper presented at the Proceedings of The 14th Asia Pacific Vibration Conference.

Yau, M., Chan, T., Thambiratnam, D., & Tam, H. (2013). Methodology for measuring the vertical displacements of bridges using fibre Bragg grating sensors. *Australian Journal of Structural Engineering*, 14(1), 71-84.

Ye, X., Su, Y., & Han, J. (2014). Structural health monitoring of civil infrastructure using optical fiber sensing technology: A comprehensive review. *The Scientific World Journal*, 2014.

Yong, Z., Zhan, C., Lee, J., Yin, S., & Ruffin, P. (2006). Multiple parameter vector bending and high-temperature sensors based on asymmetric multimode fiber Bragg gratings inscribed by an infrared femtosecond laser. *Optics letters*, 31(12), 1794-1796.

Zhou, Z., Graver, T. W., Hsu, L., & Ou, J.-p. (2003). Techniques of advanced FBG sensors: Fabrication, demodulation, encapsulation, and their application in the structural health monitoring of bridges. *Pacific Science Review*, 5(1), 116-121.

SUPPLEMENTARY

Paper Presented

Almubaied, O., Chai, H. K., Islam, M. R., Lim, K. S., Tan, C. G. (2017). Monitoring corrosion process of reinforced concrete structure using FBG strain sensor. *IEEE Transactions on Instrumentation and Measurement*, PP(99), 1-8.

University of Malaya